Fall 2011

Alendronate treatment elicits a reduction in fatigue-life of canine cortical bone

Joseph Ryan Geissler
New Jersey Institute of Technology

ABSTRACT

ALENDRONATE TREATMENT ELICITS A REDUCTION IN FATIGUE-LIFE OF CANINE CORTICAL BONE

by
Joseph Ryan Geissler

Bone serves contradictory needs; bone must be strong yet light, and stiff yet flexible. At the tissue level bone material withstands cyclic loading without failing by dissipating energy via the formation and accumulation of microdamage. Proper removal of this damage in exchange for fresh tissue is vital to bone maintenance, and is achieved through a remodeling process. Imbalanced remodeling leads to osteoporotic fractures. Bisphosphonate drugs are proven to reduce fracture risk. However, the long-term effects of bisphosphonates on tissue-level properties are unknown. This study characterized the fatigue-life of cortical bone tissue after bisphosphonate treatment with alendronate (Aln). 11^{th} ribs from 36 skeletally mature female beagles (1-2 years of age) treated daily with either a vehicle control (Cont, 1mL/kg saline) or Aln (0.2 or 1.0 mg/kg) for 3 years were evaluated. From both medial and lateral cortices, 1-6 cortical bone beams of uniform rectangular cross-section (0.5 x 1.5 mm) and length (10 - 12 mm) were prepared. A total of 90 bone beams were mechanically loaded in 4-point bending at specific stress amplitudes, 45-85 MPa, applied sinusoidally at 2 Hz until fracture or 250,000 cycles. Compared to control, Aln 1.0 beams exhibited significantly lower initial stiffness (15%) and cycles to failure (>3-fold, $p<0.05$). While control exhibited increased loss of stiffness as a function of increasing stress amplitude, this was not observed with Aln treatment. This first fatigue study of bisphosphonate-treated bone suggests mechanisms behind the atypical cortical bone fracture patterns that have been observed clinically in a subset of patients on long-term bisphosphonate treatment.

ALENDRONATE TREATMENT ELICITS A REDUCTION IN FATIGUE-LIFE OF CANINE CORTICAL BONE

by
Joseph Ryan Geissler

A Thesis
Submitted to the Faculty of
New Jersey Institute of Technology
in Partial Fulfillment of the Requirements for the Degree of
Master of Science in Biomedical Engineering

Department of Biomedical Engineering

January 2012

APPROVAL PAGE

ALENDRONATE TREATMENT ELICITS A REDUCTION IN FATIGUE-LIFE OF CANINE CORTICAL BONE

Joseph Ryan Geissler

Dr. William C. Van Buskirk, Thesis Co-Advisor Distinguished Professor and Chair of Biomedical Engineering, NJIT	Date
Dr. James Christopher Fritton, Thesis Co-Advisor Assistant Professor of Orthopaedics, UMDNJ Adjunct Professor of Biomedical Engineering, NJIT	Date
Dr. Treena L. Arinzeh, Thesis Committee Member Professor of Biomedical Engineering, NJIT	Date

BIOGRAPHICAL SKETCH

Author: Joseph Ryan Geissler

Degree: Master of Science

Date: January 2012

Undergraduate and Graduate Education:

- Master of Science in Biomedical Engineering,
  New Jersey Institute of Technology, Newark, NJ, 2012

- Bachelor of Science in Chemical Biology with
  Minor in Interdisciplinary Healthcare Ethics,
  Saint Joseph's University, Philadelphia, PA, 2009

Major: Biomedical Engineering

Spotlight Presentations:

Bajaj D., Geissler J.R., Allen M.R., Burr D.B., Fritton J.C. (2011) Fatigue life characterization of long-term alendronate-treated canine cortical bone tissue. Abstract presented at the Orthopaedic Research Society Annual Meeting. Long Beach, CA, USA — January 12-16, 2011. http://www.ors.org/web/Transactions/57/0090.PDF

Geissler J.R., Bajaj D., Allen M.R., Burr D.B., Fritton J.C. (2012) Alendronate treatment elicits a reduction in fatigue-life of Canine Cortical Bone. Abstract to be presented at the Orthopaedic Research Society Annual Meeting. San Francisco, CA, USA — February 4, 2012.

"You can get so confused
that you'll start in to race
down long wiggled roads at a break-necking pace
and grind on for miles across weirdish wild space,
headed, I fear, toward a most useless place.

The Waiting Place… …for people just waiting.

Waiting for the fish to bite
or waiting for wind to fly a kite
or waiting around for Friday night
or waiting, perhaps, for their Uncle Jake
or a pot to boil, or a pair of pants or a wig
with curls, or Another Chance.
Everyone is just waiting.

NO!
That's not for you!
Somehow you'll escape
All that waiting and staying.

You'll find the bright places where Boom Band are playing
With banner flip-flapping
Once more you'll ride high!
Ready for anything under the sky.
Ready because you're that kind of guy!" **-Dr. Seuss**

Life if full of ups and down, peaks and valleys; success and failure meant not to destroy us, but to challenge our status quo. Life throws you a curve ball not to strike you out, but to see how you can adapt to an ever changing environment. This was most elegantly personified through the life a close friend who has recently passed away.

As I begin my transition from masters to Ph.D., I am being presented with new, challenging responsibilities. One of which that I have enjoyed most is acclimating new students to the lab. To me, this was a chance to test my teaching abilities. However, with one individual, I was the student.

Rohit was a young scholar full of life. He was never without a smile and can do attitude. Regardless of the situation, he was ready to embark on life's next journey no matter how daunting the task, never content with his current situation.

The most important lesson which I have learned from my friendship with Rohit was that win or lose, never find yourself in a steady state; whether good news or bad, avoid *The Waiting Place*. Rohit will always remain in my thoughts and serve as the driving force which has not only lead me to complete the work outlined in this thesis, but the motivation to continue down a path of academic success.

Lost but not forgotten.

Rohit Belman
12/18/1988 - 08/23/2011

ACKNOWLEDGEMENT

I would like to first thank my academic mentors for providing me with the intellect and resources to complete this comprehensive investigation. Drs. J. Christopher Fritton and Devendra Bajaj welcomed me into the lab about two years ago and have been training me to excel in both my academic and professional pursuits ever since. There is no doubt that these two individuals are directly responsible for the recent honors and recognition which I have received from the research community. They continue to push me to exceed well beyond my own expectations as I continue my journey in academia, presenting me with academic opportunities most graduate students are unaware of.

Although I have only known Dr. Bajaj for a short time, he has had a profound impact on my academic and professional career. He has, and continues, to steer me in the right direction providing just enough insight for me to make my own conclusions. Dr. Bajaj and I have been able to balance a unique relationship. Dr. Bajaj is a friend when I am confused and frustrated as well as an antagonist when I am unfocused and veer off task. There is no doubt that without the help and motivation from Dr. Bajaj, the caliber of work presented in this thesis would simply not exist.

Next, I would like to thank faculty members of the New Jersey Institute of Technology Department of Biomedical Engineering, specifically Drs. William Van Buskirk, Treena Arinzeh, Richard Foulds, Bryan Pfister and Max Roman. Each one has help to facilitate my successful completion of a Master's degree and have challenged me to continue my academic career with a Ph.D. I thank them for seeing my potential and look forward to future collaborations.

A very special thanks goes to my family. Without their unconditional love and support, there is no doubt that I would not be who I am today. They have always stood by me in times of joy and despair. The individual achievements and success of my family members has taught me to not only take chances and fail, but more importantly to get back up and achieve something even greater. And for that, I am forever grateful.

TABLE OF CONTENTS

TABLE OF CONTENTS
(Continued)

Chapter **Page**

TABLE OF CONTENTS
(Continued)

Chapter **Page**

LIST OF TABLES

LIST OF FIGURES

LIST OF FIGURES
(Continued)

Figure **Page**

LIST OF FIGURES
(Continued)

Figure **Page**

LIST OF FIGURES
(Continued)

Figure **Page**

LIST OF FIGURES
(Continued)

Figure **Page**

LIST OF FIGURES
(Continued)

Figure **Page**

CHAPTER 1

INTRODUCTION

Bone functions to provide mechanical stability and mineral homeostasis, as well as forms the hard portion of the musculoskeletal system that facilitates the cyclic loading of locomotion, maintains body shape, and protects vital organs. Throughout growth and into adulthood bone tissue is constantly renewed and repaired in a process known as remodeling, thus maintaining structural and mechanical integrity. However, bone's metabolism and remodeling slows down with ageing and/or disease resulting in bone tissue loss, osteoporosis and fragile bones.

Pharmaceutical countermeasures are often sought to reverse bone loss. Bisphosphonate drugs, such as alendronate, are currently the most effective treatment for osteoporosis and are proven to reduce fracture risk in both men and women. However, bisphosphonates also reduce the tissue remodeling capability of bone cells. This reduction may lead to local, or tissue-level, changes with serious implications for fragility fracture risk. In this investigation, tissue-level mechanical properties of alendronate-treated cortical bone will be evaluated with cyclic loading.

1.1 Bone

At the largest scale of organization, bone is divided into two compartments, cortical and trabecular (Figure 1.1). Cortical bone, or the outer shell cortex, accounts for approximately 80% of the skeletal mass [1]. Sometimes described as compact, cortical bone is composed largely of osteons that are formed by concentric layers of mineralized

collagen fibers. Each osteon provides mechanical strength to bone, and support for nerves and blood vessels within a main pore known as the Haversian canal (Figure 1.1) [1]. Blood vessels also branch off in perpendicular directions from the vessels of the Haversian canal into smaller perforating, or Volkmann's canals that run within the osteon (Figure 1.1). This system of canals is vital to the maintenance and survival of bone tissue since they provide the conduit for nutrient supply. Around the Haversian canals concentric layers of collagen fibers form nearly perpendicular to each other. This level of organization adds to the strength of cortical bone and provides anisotropy that in turn promotes resistance against damage that may occur in the form of microcracks. *Principally, an anisotropic material exhibits toughness due to the ability to resist crack extension*. The engineering definition of toughness is the energy absorption capacity of a material. The space between the osteons also contributes to bone's anisotropic mechanical properties and is comprised of interstitial lamellae that are not part of a complete osteon (Figure 1.1).

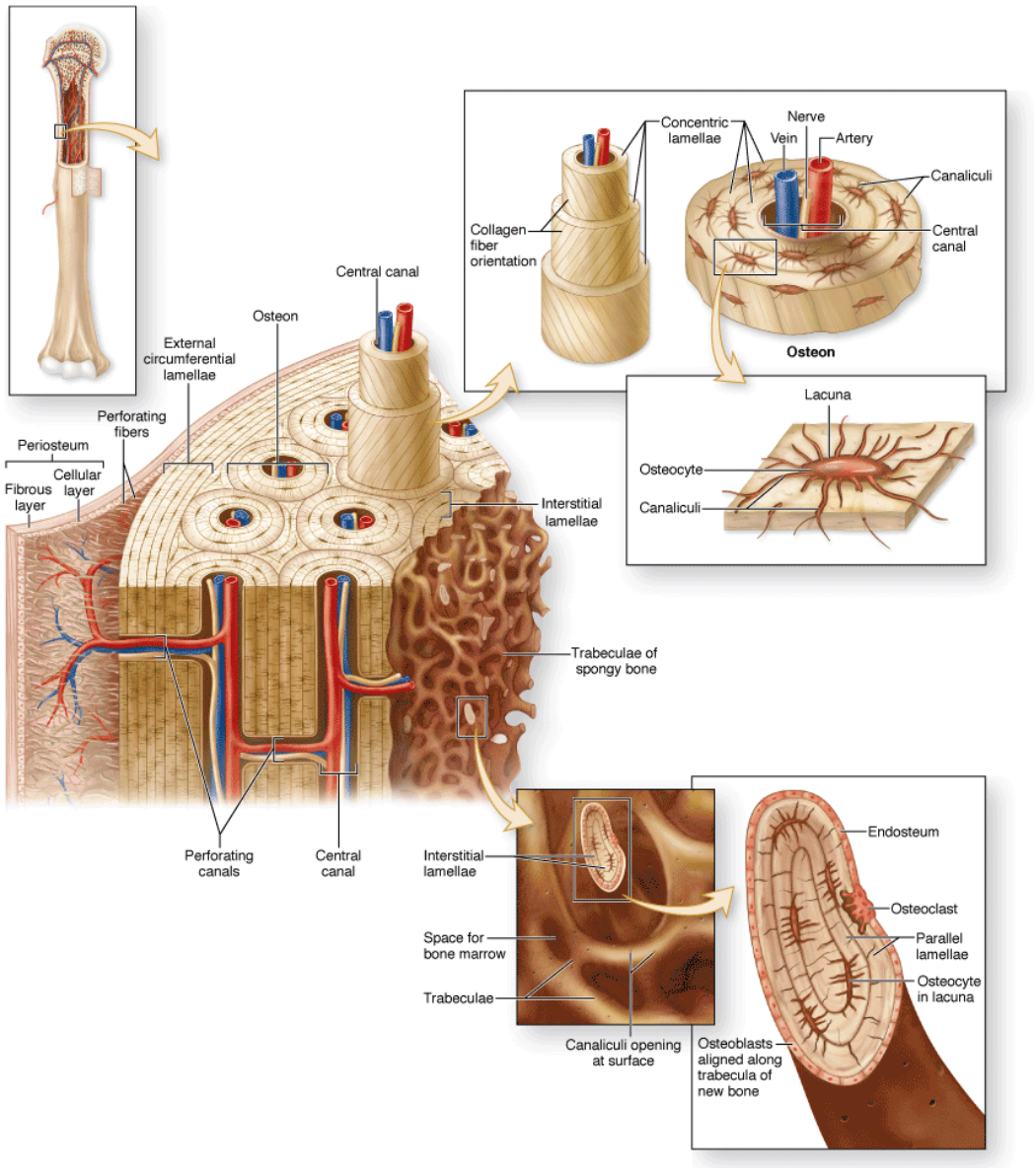

Figure 1.1 Schematic of the cortical, trabecular, lamellar and cellular organizations within bone [2].

Trabecular bone, also referred to as cancellous bone, accounts for the remainder (20%) of skeletal mass [1]. Trabeculae are described as forming a microarchitecture of interconnected plates and rods. They are generally found at the ends of long bones, in the vertebrae of the spinal column and sandwiched in-between the cortical shells of flat

bones, such as those of the hip and pelvis. Trabecular bone has a large surface area exposed to the internal environment that allows for easy exchange of ions and proteins. In addition, the micro-architecture of trabecular bone plays a central role in absorbing and dissipating the energy that is applied to bones, especially near articulating joints.

The excellent mechanical and structural properties of bone are due to the regulation and organization of organic and inorganic materials by bone cells. These cells are osteoclasts that resorb bone, osteoblasts that form bone, and specialized osteoblasts known as osteocytes that play a role in maintenance of bone (Figure 1.1). Osteoblasts form bone by first producing an organic matrix, mainly cross linked type-I collagen fibers. These fibers bind hydroxyapatite $Ca_5(PO_4)_3(OH)$, an inorganic mineral that constitutes two-thirds of bone by weight [1,3]. The inorganic phase provides compressive strength and rigidity whereas, the organic phase accounts for flexibility, toughness and resistance to tensile forces [1,3,4]. The mechanical properties of bone are therefore largely dependent on the structural organization of these two phases by the bone cells.

Cellular processes leave in their wake not only the hard tissue of bone but also many levels of porosity. The largest of these pores are the medullary canal and the trabecular space, both of which are filled with bone marrow, described as a nutrient containing tissue responsible for the formation of blood's cellular components, hematopoiesis [3]. The next smallest pores are those of the Haversian canals that contain the nutrient-supplying blood vessels for the deep cortical tissues. At a smaller, cellular level are the osteocyte lacunae, which are small pockets that house the osteocytes (Figure 1.1). These lacunae form as osteoblasts differentiate into osteocytes and become embedded in their own freshly secreted matrix material. Osteocytes in these lacunae can

modify their local microenvironment and have recently been found capable of moving their cell body and long dendritic processes [5]. There are 50-100 of these dendritic processes per osteocyte, each residing in a canaliculus and forming the next level of porosity [3,6,7]. The features and abilities of the osteocyte contribute to the cell's ability to translate mechanical signals into biochemical signals and convey information through the dendritic processes. These processes form a communications network of connections with neighboring cells via gap junctions. Signals sent through this network can affect tissue repair [5].

Direct communication between cells is not limited to the osteocytes as these cells form junctions with cells within the marrow and those on the outside surface of bone. Almost this entire surface, except at articulations between bones and points of attachment for tendons and ligaments, is coated in a soft-tissue layer known as the periosteum [6]. The periosteum is connected by a bundle of collagenous perforations, known as Sharpey's fibers, and is composed of two layers (Figure 1.1). The outermost periosteal layer is a fibrous layer, and acts as a sheath. The inner layer is the cambium or cellular layer and is populated by osteoblast progenitors and chondrocytes [6]. Because this region is so rich in the precursors to bone forming cells, the periosteum plays a central role in bone growth.

1.2 Bone Growth and Modeling

Investigation of embryonic bone growth provides insight into the complexity of bone development, as well as bone repair. Two main processes are responsible for bone growth, intramembranous and endochondral ossification. Intramembranous ossification is

mostly responsible for formation of flat bones (e.g., hip and pelvis). On the other hand, most longitudinal growth of vertebrates occurs during formation of long bones (e.g., femur and humerus) by endochondral ossification in which the matrix of the initial cartilage anlage is systematically replaced by mineralized tissue. Initial formation of this anlage occurs by differentiation of mesenchymal stem cells (MSC) into chondrocytes that produce a cartilage matrix as they further divide. The same MSC later differentiate into bone-forming osteoblasts that quickly lay down a flexible and disorganized 'woven' bone architecture (Figure 1.2) [6]. At the ends of long bones, growth occurs as chondrocytes divide, and secrete new collagen matrix that drives elongation [3].

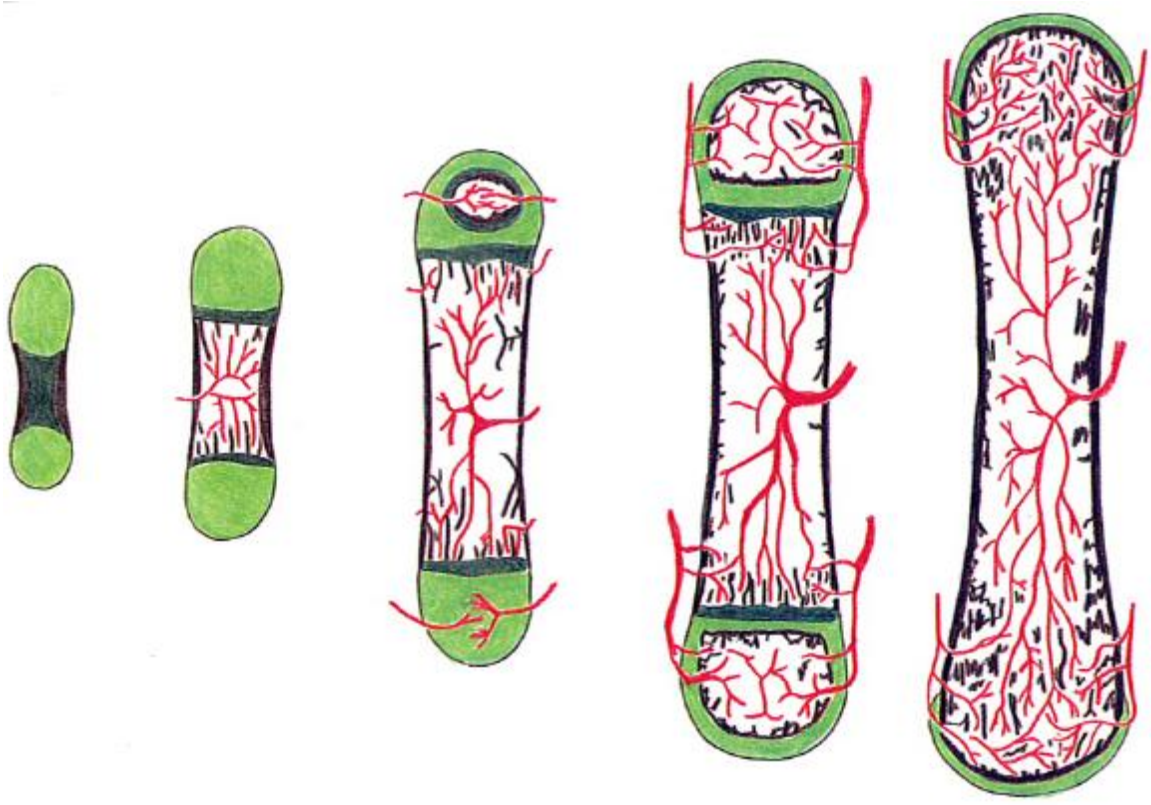

Figure 1.2 Bone growth and elongation begins in the embryo and occurs until after puberty. Depicted in this figure, uncalcified cartilage is in light green, calcified cartilage in dark green, bone is black, and blood vessels are in red. The conversion of cartilage to bone is a gradual process facilitated by osteoclasts and osteoblasts [3,8].

As bones get longer they also increase their girth by a process of 'lamellar' osteoblast apposition known as modeling. Modeling produces the correct bone shape and gives strength to bone in two important ways (Figure 1.3). First, as a result of modeling, bones become larger. Second, the less mineralized, flexible, woven bone template is replaced by a more highly organized, rigid mineral lamellar bone structure. Therefore, the transition from woven to lamellar tissue during growth is an important process that establishes the mechanical properties of bone in a young adult.

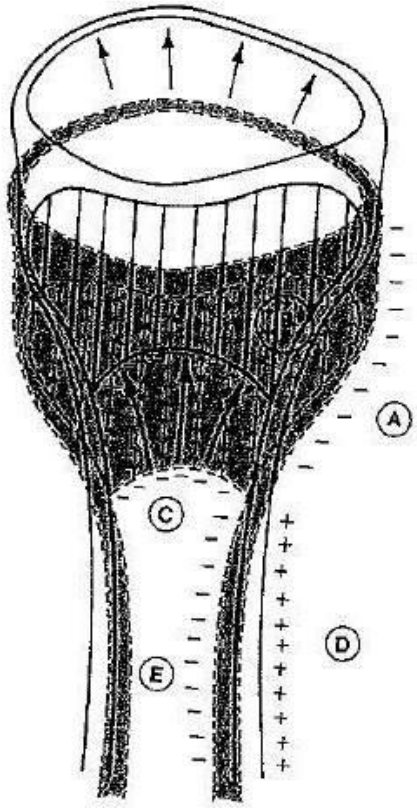

Figure 1.3 Diagram of the modeling occurrence during growth of proximal end of the tibia. Frontal section of original proximal tibia is indicated as stippled area. The situation after growth period of 21 days is superimposed. (A) Reduction of metaphyseal funnel into a narrower shaft by osteoclastic bone resorption (resorption drift) along periosteal surface of metaphysis (-). (B) Thickening of cortex by osteoblastic bone formation (formation drift) along cortical endosteal surface of metaphysis (+). (C) Enlargement of marrow cavity by osteoclastic resorption of metaphyseal trabecular and subendocortical bone (-). (D) Increase of the diameter of the shaft by periosteal bone formation first (+). (E) Enlargement of the marrow cavity by cortical endosteal bone resorption (-) [9].

1.3 Bone Remodeling

The most important process for maintaining the mechanical properties of bone during adulthood is remodeling, or the turnover of old bone tissue with new (Figure 1.4). This dynamic process allows for the tissue to continually renew itself with complete turnover occurring every 4 to 20 years in the adult human [10]. Remodeling also allows for alterations in bone structure in response to changes in the functional demands of the mechanical environment so that bone can be added where needed and removed where not required. Another type of targeted remodeling occurs in response to micro-damage which is a consequence of normal loading activity.

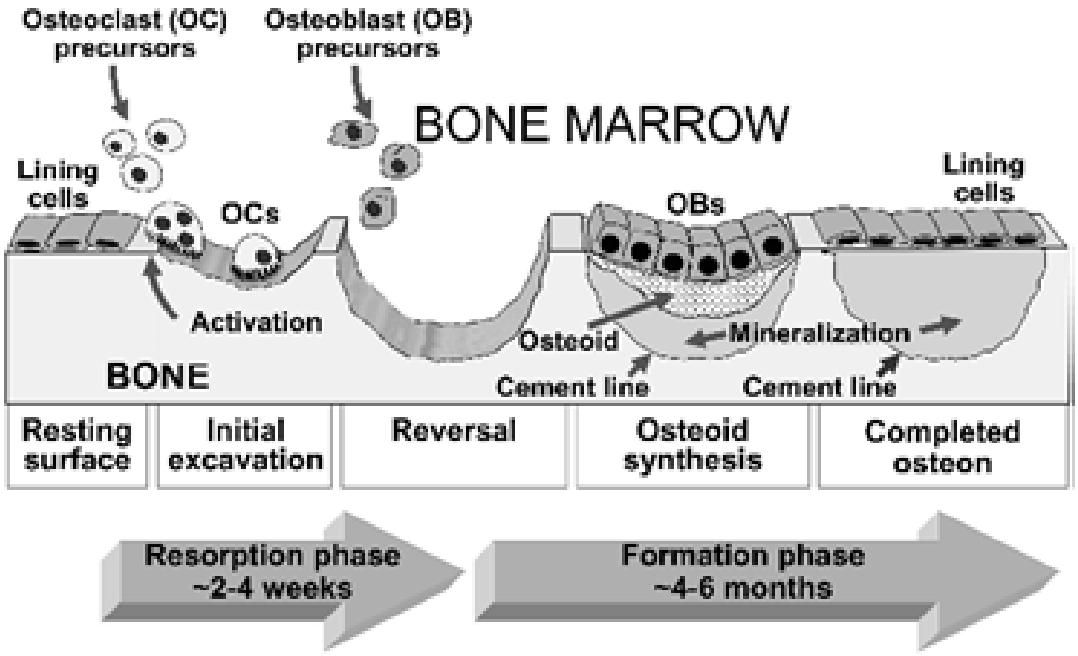

Figure 1.4 Schematic of trabecular bone remodeling. Bone turnover describes the complete process of bone remodeling. This consists of an initiating event, followed by bone resorption, and then bone formation [11].

Targeted bone remodeling may be initiated by the death of osteocytes after an injury (Figure 1.5). In the case of physical damage to the cell a process of apoptosis, or

regulated cell death, may be initiated. During the process of dying the osteocyte and neighboring cells release biochemical signals that initiate the sequential and coordinated activity of multinucleated osteoclasts to break down bone. These osteoclasts are joined, in what is known as a basic multicellular unit (BMU), by mononucleated osteoblasts to rebuild bone (Figure 1.1) [1,3,10,12,13]. Therefore, the regulation of the BMU and the activity of osteoclasts and osteoblasts are vital for the survival of bone and the bone's owner.

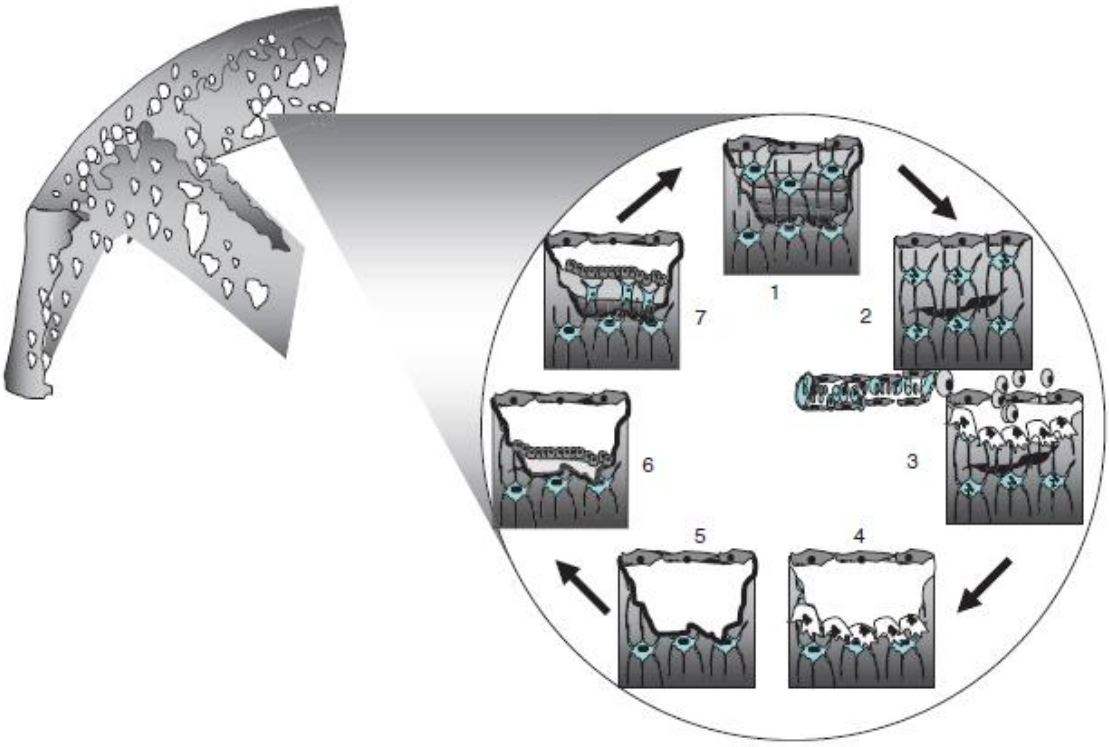

Figure 1.5 (1) Osteocytes are connected by processes to each other and to lining cells on the endosteal surface. (2) Damage to osteocytic processes by a microcrack produces osteocyte apoptosis. The distribution of apoptotic osteocytes provides information needed to target osteoclasts to the damage. (3) Osteoclast precursors may be delivered from the marrow via circulation. (4) Osteoclasts resorb damage and bone. (5) The reversal phase and formation of a cement line. (6) Osteoblasts deposit osteoid. (7) Some osteoblasts are entombed in osteoid and differentiate into osteocytes reconstructing the osteocytic canalicular network [14].

While the remodeling process occurs similarly in all bones, differences in trabecular and cortical bone architecture lead to slightly different modes of action. As previously discussed trabecular bone has greater surface area than cortical bone and therefore BMU activity is surface based. In the first stage of trabecular bone remodeling, bone lining cells retract to expose the surface of bone (Figure 1.4) so that osteoclasts can gain access. The exact signaling mechanism which initiates this process is still unknown. However, once this signal is received and the bone lining cells retract, osteoclasts attach to the bone and form a ruffled border that isolates the extracellular environment from the hydrochloric acid that they release to disintegrate the components of bone (Figure 1.6). Once resorption is complete, the osteoclast detaches leaving an empty pit, known as the resorption pit.

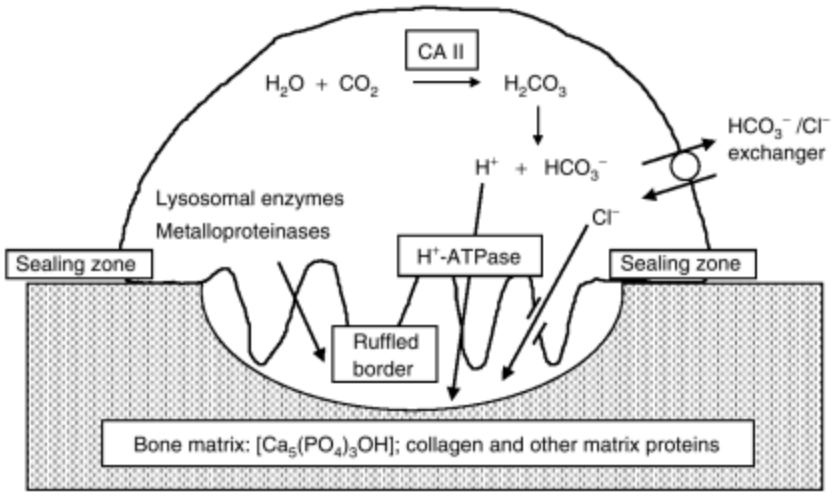

Figure 1.6 The mechanism of resorption activity of osteoclasts. Within the sealed site, acids and hydrolases are secreted to dissolve bone minerals and digest organic matrix, respectively [3]. Treatment with anti-resorptive agents, namely bisphosphonates, inhibits proper sealing between osteoclasts and bone matrix, restricting bone resorption [15].

The second stage is formation by deposition of lamellar layers of new bone matrix material, the osteoid, by osteoblasts of the BMU [7]. While the pit is being filled with

osteoid, some osteoblasts will become embedded in the freshly deposited material forming a communication network within the freshly mineralized tissue (Figure 1.7), transitioning into osteocytes, while others will undergo apoptosis after completing their deposition. Upon completion of osteoblastic activity, the bone lining cells cover over the newly formed bone. The complete bone packet is described as a hemi-osteon (Figure 1.4).

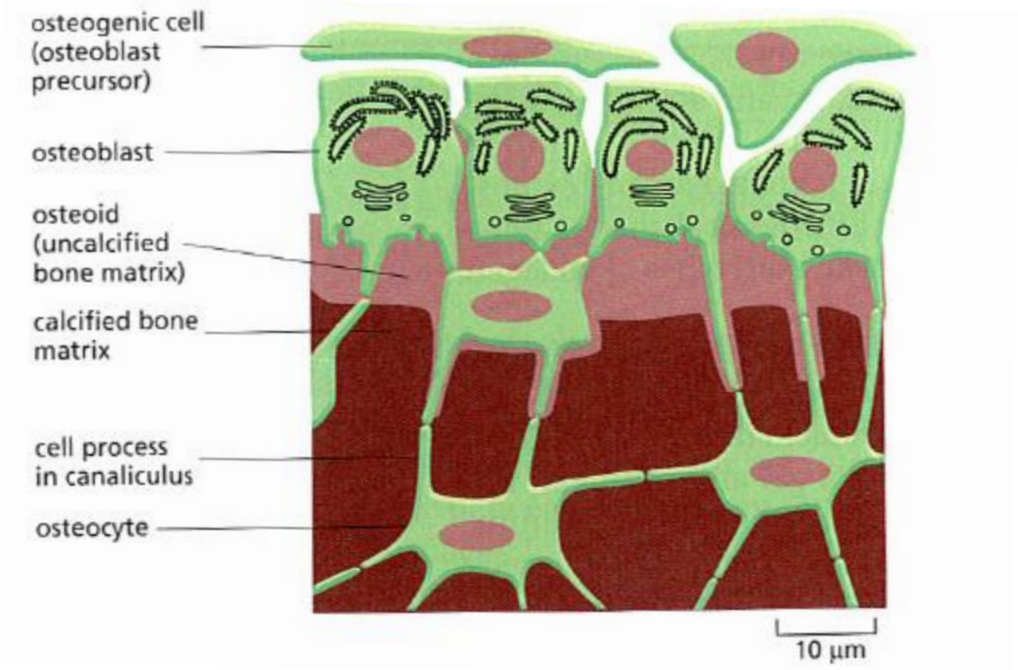

Figure 1.7 Osteoblasts that line the bone's surface secrete an uncalcified bone matrix, osteoid. Some osteoblasts will be embedded within the osteoid as this layer transitions into a calcified bone matrix. As this matrix begins to harden, immobilized osteoblasts become osteocytes and extend canals, known as canaliculi, between osteocytes [3].

As opposed to the hemi-osteon, a complete osteon results from remodeling activity in cortical bone. In cortical bone, osteoclasts must penetrate longitudinally through the layers of bone to generate a resorption cavity (Figure 1.8). The process by which these cells tunnel through bone is characterized as a cutting cone because of the shape, a cavity forms as osteoclasts break down bone. While the osteoclasts traverse

through bone, a capillary loop follows to supply both blood and cells to the advancing cone [6]. It is unclear whether the osteoclasts pull the capillary loop along or the capillary loop pushes the osteoclasts. Regardless, a constant blood supply is necessary for cell survival. Osteoblasts are recruited to the resorption cavity, and beginning from the outer surface of the cavity, lay down layers of osteoid forming concentric circles around the capillary loop. When new bone has completely surrounded the nerves and blood supply, the Haversian system is complete and a new osteon has been formed (Figure 1.8) [1,6].

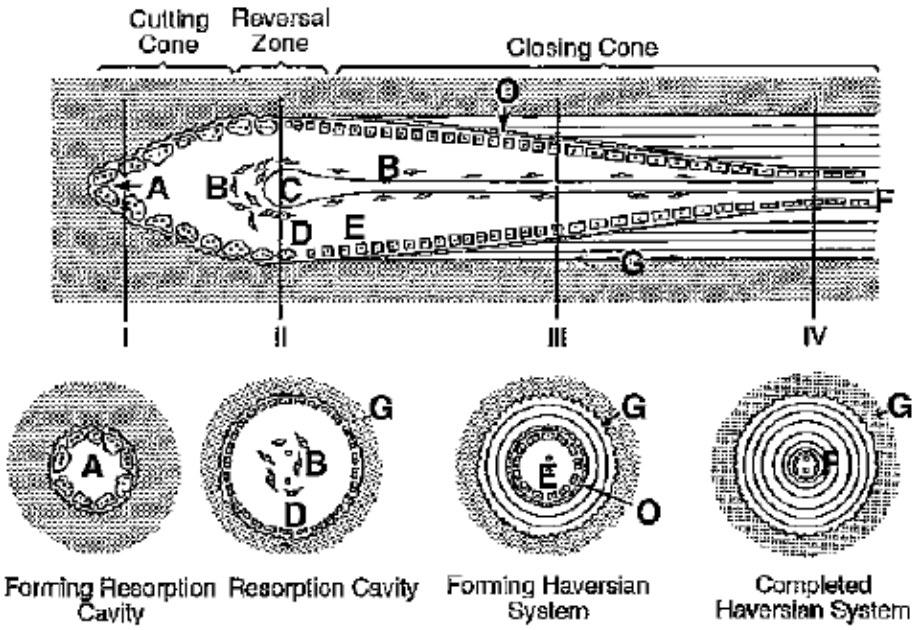

Figure 1.8 Diagram showing a longitudinal section through a cortical remodeling unit with corresponding transverse sections below. (A) Multinucleated osteoclasts in Howship's lacunae advancing longitudinally from right to left and radially to enlarge a resorption cavity. (B) Perivascular spindle-shaped precursor cells. (C) Capillary loop delivering osteoclast precursors. (D) Mononuclear cells (osteoblast progenitors) lining reversal zone. (E) Osteoblasts apposing bone centripetally in radial closure and its perivascular precursor cells. (F) Flattened cells lining Haversian canal of completed Haversian system or osteon. Transverse section at different stages of development: (I) resorption cavities lined with osteoclasts; (II) completed resorption cavities lined by mononuclear cells, the reversal zone; (III) forming Haversian system or osteons lined with osteoblasts that had recently apposed three lamellae; and (IV) completed Haversian system or osteon with flattened bone cells lining canal. Cement line (G); osteoid (stippled) between osteoblast (O), and mineralized bone [1].

1.4 Microdamage and Fatigue Crack Growth

The construction of healthy bone, described in the previous section, provides a mechanism for energy dissipation (measured as toughness) which is vital for bones ability to resist fracture. To accommodate for very small changes in the stress acting across the surface area of bone during daily cyclic loading, minute cracks form and function to dissipate the load and are referred to as microcracks. Microdamage can occur in the form of linear microcracks or diffuse damage. Linear microcracks which arise under compressive loading are described as individual, well-defined cracks that propagate through interstitial bone. Linear microcracks are also restricted from propagating across osteons and are diverted around osteonal boundaries i.e. cement line and layers of concentric mineralized collagen fibers [17]. Diffuse damage occurs under tensile loading and is characterized as an array of small cracks highly concentrated in a single location within interstitial bone [17]. In general, microdamage is restricted to more densely mineralized, older bone tissue found between osteons [18].

During daily cyclic loading of bone, cracks that initiate and propagate throughout bone are confined to specific regions and prevent catastrophic failure i.e. fracture. The complex structure of an individual osteon described in the previous section, as well as the amount of osteons per unit of bone volumes, play a key role in distributing energy and resisting fracture [18]. A result of fatigue loading is the accumulation of microdamage at sites of increased mineralization. In healthy bone, damage is repaired at a rate which prevents coalescence. However, if damage accumulation is not repaired expeditiously, fracture will require less energy to initiate and propagate leading to catastrophic failure.

When investigating the principles of crack initiation within an engineering material e.g. metals, one must first recognize there are a variety of approaches, or mechanisms, which attempt to explain this unique event. Proposed by W.A. Wood in 1958, crack initiation can be attributed to varying amounts of net slip across different planes within a metal as a result of cyclic loading [19]. As a material is fatigued, irreversible displacements occur along slip bands which cause the material surface to become rough. This surface roughening can be attributed to the formation of 'hills' and 'valleys' (or extrusions and intrusions) at locations where slip bands interface with a free surface [19]. These slip bands, also referred to as persistent slip bands, can exist throughout a material and generate a preferential site for crack initiation to occur [20]. It has been suggested that the fatigue life a material will reduce as the materials surface becomes rougher. In fact, a study by Thompson, Wadsworth and Louat put forth the notion that fatigue life of copper can be increased by removing these 'hills' and 'valleys' by means of electrospinning the specimen's surface [21]. Although maintaining a smooth and defect free surface may increase fatigue life, it is not practical and cannot be achieved within bone. Therefore, crack nucleation will undoubtedly take place, resulting in crack propagation.

Upon cyclic loading of bone, stress at the tips or boundaries of the cracks increases which facilitates crack growth and extension. Based on work conducted by Paris *et al.*, fracture mechanics can be applied to fatigue crack growth in order to characterize its behavior. Located at a crack's tip is a cyclic plastic zone through which the crack propagates. As the crack grows, it leaves behind a plastic wake which surrounds the extending crack (Figure 1.9). Illustrated in Figure 1.9, if the plastic zone is contained

within the elastic singularity zone, then the crack growth can be characterized by K_{min} and K_{max} [22]. This relationship can also be expressed as:

$$\frac{da}{dN} = f1(\Delta K, R)$$

where da/dN is rate of crack growth, i.e. crack growth per cycle, ΔK is the stress intensity range (K_{max}-K_{min}) and R is the stress ratio (K_{min}/K_{max}) [22]. The integration of this equation provides an equation which can be used to estimate fatigue life:

$$N = \int_{ao}^{af} \frac{da}{f1(\Delta K, R)}$$

where N is the number of cycle required to propagate a crack, a_o is the initial crack length, a_f is the final crack length [22].

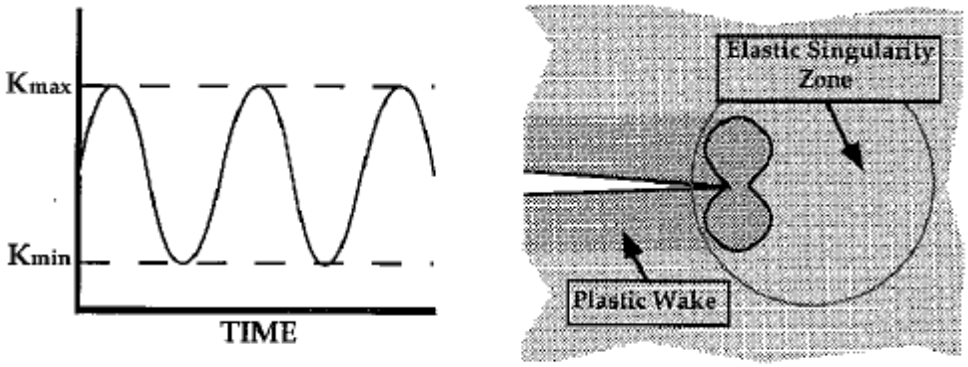

Figure 1.9 Illustration of fatigue crack propagation through a material under constant amplitude [22].

A log-log plot of da/dN versus ΔK of typical fatigue crack growth in metals helps illustrate the relationship between crack growth per cycle and the change in applied stress (Figure 1.10). This sigmoidal curve demonstrates the affects of fatigue on crack growth. Crack propagation is illustrated in the linear region (Region II), where crack growth rate is insensitive to microstructure and da/dN follows Paris Law of power:

$$\frac{da}{dN} = C(\Delta K^m)$$

where C is the fatigue crack growth coefficient and m is the fatigue crack growth exponent, an index of the material brittleness [22].

At high (Region III) and low (Region I) ΔK values, the crack growth rate tends to deviate from the linear region and represents crack initiation and fracture, respectively. Fracture toughness can be inferred from region III, as the crack growth rate increases as K_{max} approaches $K_{critical}$. Under high cyclic stress, the cross sectional area of the material will become reduced to the point where the load can no longer be sustained, resulting in fracture. Bone demonstrates a similar response. However, the difference in healthy living bone tissue versus metals is that a balance in damage accumulation and repair preserves strength.

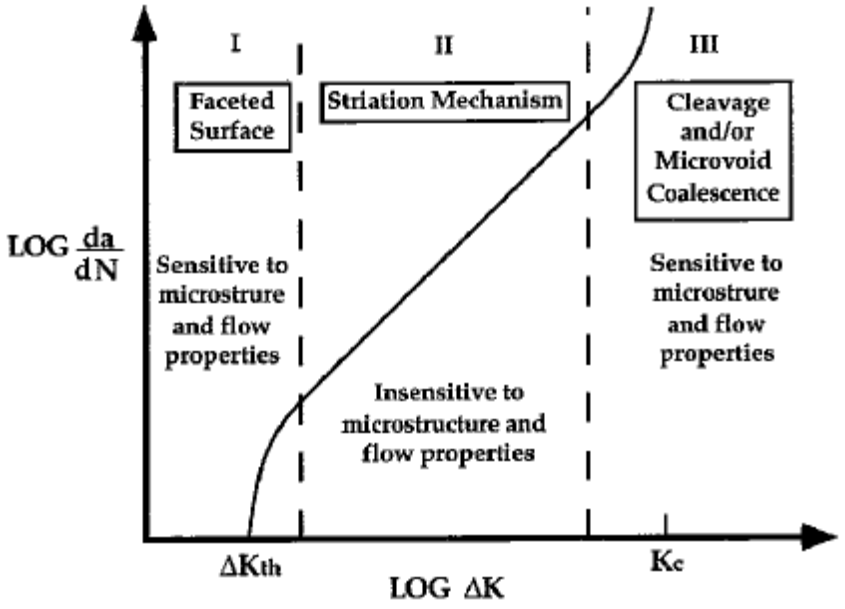

Figure 1.10 Log-log plot of da/dN verses ΔK demonstrating typical fatigue crack behavior in metals [22].

1.5 Osteoporosis and Related Diseases

Unbalanced regulation of the bone remodeling processes, bone resorption and bone formation, will give rise to a variety of metabolic bone diseases, including osteoporosis and Paget's disease. For example, osteoporosis may be caused either by increased bone resorption in which bone formation fails to keep up, or by decreased bone formation with little change in the rate of resorption. The result of this age-related skeletal disease is low bone mass and deterioration of bone microstructure (Figure 1.11). Besides the many different forms of osteoporosis, Paget's disease is a bone wasting disease in which there is an increase in bone loss due to over activity of osteoclasts. In an attempt to compensate for bone loss, bone will undergo rapid formation. However, this dramatic increase in new bone production leads to the formation of unorganized bone structure. For example, over expanded bone and increased formation of blood vessels may occur. With the latter, various neurological complications can arise. These changes can ultimately result in reduced bone strength and increased bone fragility.

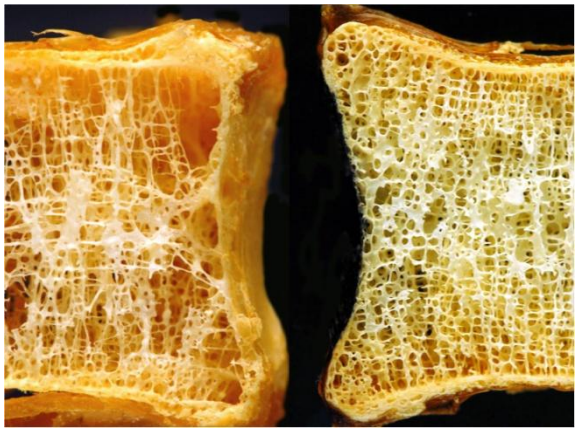

Figure 1.11 Depicted in this image is the microarchitecture of both an osteoporotic (left) and healthy (right) human lumbar. Good bone quality, visualized in healthy tissue, provides structural support to the bone. Poor bone quality, visualized in osteoporotic tissue, does not provide bone with structural support [6].

Fractures due to osteoporosis are associated with great morbidity and mortality with 25% of hip fracture patients dying within one year of fracture occurrence. Furthermore, these fractures are difficult to foresee, and the fact that osteoporosis is generally not diagnosed until after a severe fracture demonstrates the quiet nature of this disease. Osteoporosis affects approximately ten million Americans, 80% of whom are women [23]. Annual healthcare costs due to osteoporotic fractures alone are estimated to increase to approximately $25 billion by 2025 [23]. The prevention of fractures due to osteoporosis, and other bone wasting disease, is important for medical research. Understanding the underlying mechanisms of osteoporotic fractures will lead to the development of better strategies and methods of treatment, and prevention. As such, methods for early detection and pharmaceutical countermeasures that would help restore the structural and mechanical properties of bone must be developed.

1.6 Osteoporosis Treatments

Apart from diet and exercise, the most common countermeasures for osteoporosis are drug treatments that stimulate bone formation and inhibit bone resorption. Described in this section are two effective interventions (Figure 1.11).

One bone formation stimulating class of drugs is based on parathyroid hormone (PTH), a protein secreted into the circulatory system that functions to regulate calcium and phosphate levels in the body [24]. A healthy individual has about 1,135 grams of calcium contained in the body, of which about 99% is found in bones [24]. Proper regulation of these ions is vital to muscle, bone and nerve function. PTH given exogenously stimulates bone formation and has been found to improve several properties

of bone such as bone density and size, as well as bone microarchitecture (Figure 1.12) [25]. However, using PTH as an anabolic agent to treat osteoporosis has faced many challenges. Administration of PTH causes an initial stimulation of bone formation, later to be followed by the promotion of bone resorption [25,26]. Therefore, an optimal 'anabolic window', defined as the time period in which the activity of PTH is maximally anabolic, is desired for safe and effective treatment [25]. In part due to the difficulty of establishing this window, other methods of treatment have been favored.

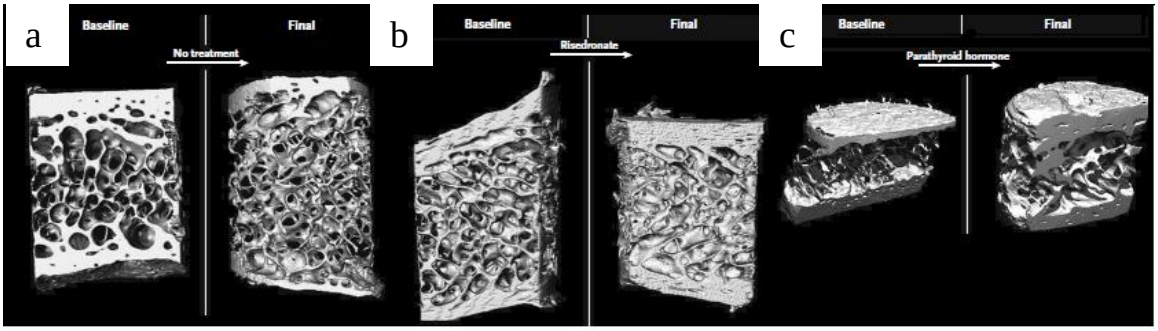

Figure 1.12 Biopsies from the iliac crest were collected before treatment and three years after. Microcomputed tomography of biopsies: (a) no treatment demonstrates thinning of cortical and trabecular regions and loss of overall structure. (b) Treatment with antiresorptive agent risedronate proves to be an effective measure, as the overall bone tissue structure is maintained. (c) Parathyroid hormone treatment promotes the thickening of cortical and trabecular regions [18,28].

Anti-resorptive agents that inhibit bone resorption, such as bisphosphonates, are the most commonly used treatment for osteoporosis. The general chemical formula of all bisphosphonates contain a nonhydrolyzable P-C-P backbone, however differences in side chains allows for diversity among bisphosphonates (Figure 1.13). Bonded to each phosphorous are double bound oxygen and two hydroxyl groups. Attached to the carbon are two side chains, known as R_1 and R_2, which account for the diversity and potency among bisphosphonates. Most bisphosphonates will contain a hydroxyl group at the R_1 position, making them more potent than those which lack the hydroxyl group [28].

Bisphosphonates like aldendronate and pamidronate, which contain a nitrogen atom in an alkyl chain, have been found to be 10-100 fold more potent than those that do not contain nitrogen atoms at all (etidronate and clodronate). Compounds which contain a tertiary nitrogen atom are even more potent, and compounds, like risedronate, containing a nitrogen within a heterocyclic ring are 10,000 fold more potent than etidronate [28].

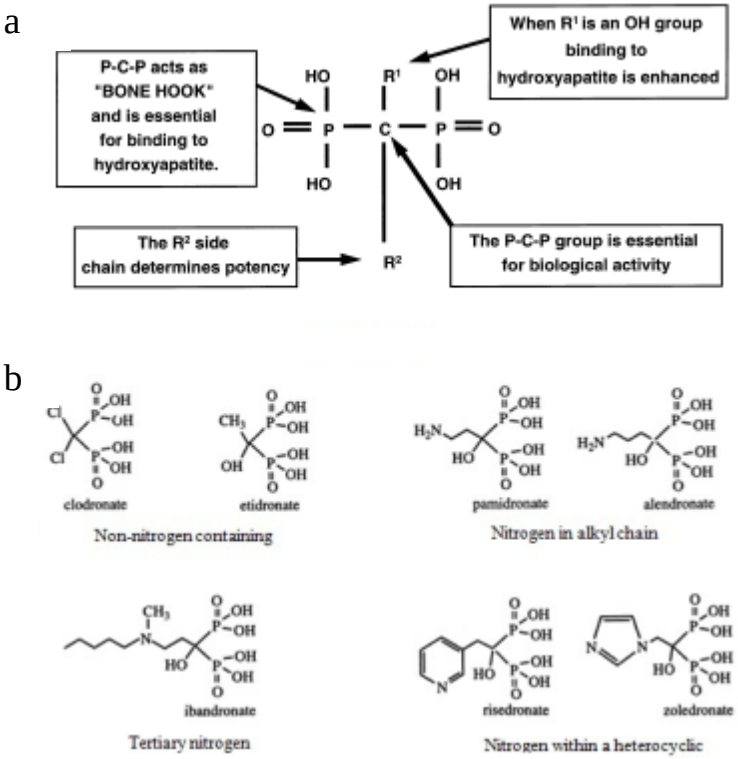

Figure 1.13 Bisphosphonate structures. (a) General structure of bisphosphonates [29]. (b) Clinically important bisphosphonates [28].

When administered, the hydroxyl group of the R_1 chain and the phosphonate groups act as molecular hooks which allow the bisphosphonate to quickly dock to bone mineral surfaces. Upon resorption, osteoclasts take up bisphosphonates as they degrade the bone by endocytosis. The bisphosphonate becomes internalized and functions to disrupt signaling pathways which facilitate the normal functioning of osteoclasts to resorb bone. Specifically, bisphosphonates interfere with osteoclasts ability to develop a

ruffled border which normally isolates the acidic environment that breaks down bone [29]. This disruption will ultimately lead to apoptosis of the osteoclast, releasing the bisphosphonate back into bone tissue (Figure 1.14) [29].

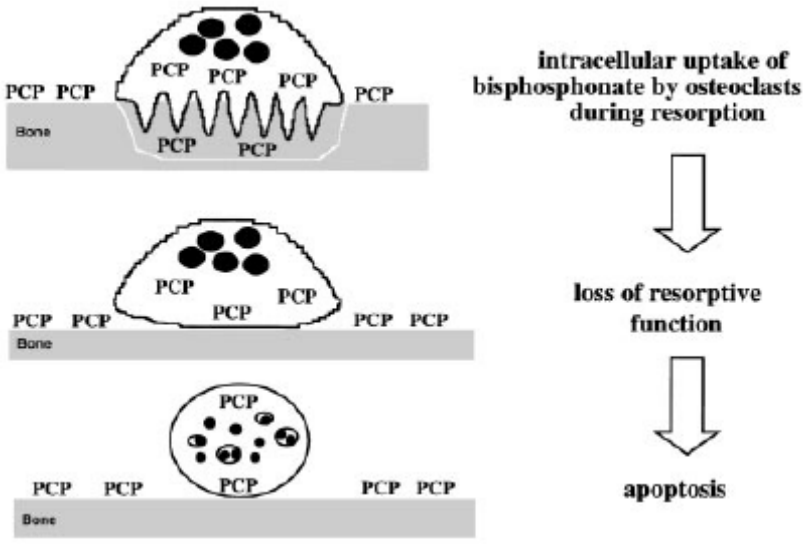

Figure 1.14 Action of bisphosphonate interrupting osteoclasts activity [29].

Bisphosphonates have been found to restore bone mineral density (BMD) and improve the biomechanical properties of bone [30]. Boivin *et al.* [2010] reported a 9.3% higher mean degree of mineralization of bone (MDMB) of cortical bone and a 7.4% higher MDMB of trabecular bone after two years of alendronate treatment. The authors suggested that reduction of activation frequency and bone remodeling activity induces a prolonged mineralization, which increases the mineral bone density at the tissue level. Increased mineralization may partially explain why short-term treatments with bisphosphonates improve the biomechanical properties of bone, including strength (the load at which a material fails) and stiffness (a materials ability to resist deformation under an applied load prior to failure). Regardless of the mode of action, short-term treatment with bisphosphonates reduces osteoporotic fracture risk in both men and women.

Although bisphosphonates are effective at reversing osteoporotic bone loss, there are concerns over the long-term use of this drug and their association with atypical fractures [31]. These fractures have been described as atypical due to their bilateral occurrence, as well as their location and fracture pattern. Over the past three years, reports of atypical fractures of the subtrochanteric region closer to the midshaft of the femur have increased in patients with long term bisphosphonate regimens. These reports have raised concerns over the long-term safety of bisphosphonates for osteoporosis treatment [31,32]. Radiographs of atypical fractures show unusual cortex beaking and thickening of the proximal femoral shaft (Figure 1.15).

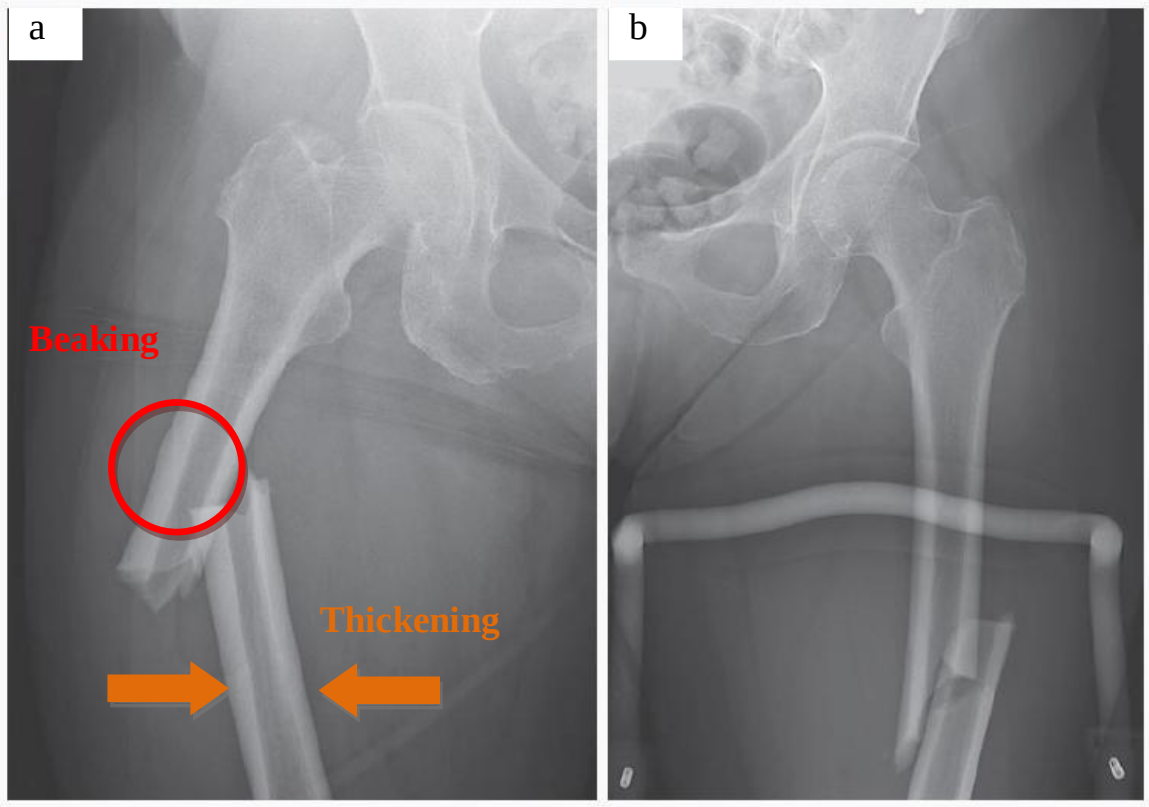

Figure 1.15 It has recently been proposed that patient using antiresorptive treatment exhibit cortical thickening prior to atypical fracture. More commonly, fracture occurs in the proximal region of the femur. (a) Femoral shaft fracture in a 83 year old woman with 9 years of treatment. (b) A similar fracture in a 77 year old woman with 5 years of treatment [32].

Recent experimental and numerical evaluations of bisphosphonate treated bone tissue have shed some light on the effects of bisphosphonate on micro-damage evolution and fracture. In 2008, Allen *et al*. reported a 30% reduction in the apparent toughness of cortical bone after three years of treatment with alendronate in healthy canines. These authors attributed the reduction in toughness to changes in tissue morphology and architecture [33]. In a more recent study, O'Neal *et al.* [2010] analyzed the effects of micro-damage on local mechanical stresses in the trabecular microarchitecture. These authors observed that a lower stress was needed to initiate fracture in the alendronate-treated group compared to control. They concluded that alendronate changes the microarchitecture of the bone and reduces its ability to resist the formation of linear microcracks [34]. These studies suggest a possible alteration in the tissue-level properties of bone that may promote bone tissue fragility [34]. Regardless, no significant effort has been put forward in developing a thorough understanding of changes in the material properties, particularly fatigue-related properties of bisphosphonate-treated bone. Therefore, the effects of bisphosphonates on fatigue-related fragility fractures remain unknown.

1.7 Objectives

Osteoporosis is a serious public health issue and can drastically alter an individual's life. The disease which has many risk factors, some predisposed by genetics and others that result from life choices. A number of previous studies have demonstrated that the use of bisphosphonates does restore some desired structural and mechanical properties to the bone of osteoporotic patients [29,30]. However, there are several concerns associated

with long term use of bisphosphonates, particularly those associated with fatigue-life and bone fragility. Previous mechanical evaluations of bisphosphonate-treated bone have been primarily conducted with monotonic loading of whole bones. While such tests provide important information regarding the structural-level properties of bone, they do not provide data on tissue-level mechanical properties. In addition, monotonic evaluation does not accurately replicate the everyday loading of bone which occurs in a cyclic manner. Thus, the study conceived of and completed for this thesis provides an evaluation of the tissue-level mechanical properties of bisphosphonate-treated canine cortical bone tissue subjected to cyclic loading.

Specifically, the objectives of this study were:

1. Evaluate the fatigue-life response of control and alendronate treated cortical bone tissue.
2. Quantify and compare any differences in stiffness as a function of stress amplitude for the control and drug-treated groups.
3. Quantify and compare the micro-structure of cortical bone as a function of drug treatment and stress amplitude.

CHAPTER 2

MEASURING BONE QUALITY

Bone quality is a term used to describe bone health. Therefore, bone quality encompasses all aspects of bone tissue that function to provide mechanical stability and mineral homeostasis. This is an extensive list, partially introduced in the previous chapter. In this chapter and the work for this thesis, the mechanical aspect of quality will be defined as dependent on both structure and bone tissue material composition. At the material level, a balance between mineral and collagen is vital to bone tissue's ability to absorb energy. To resist fracture bone must be flexible. To resist permanent deformation bone must also be stiff [18]. If these competing properties are not properly in balance then normal cyclic loading will lead to a reduction in material properties and reduced fatigue life resulting in premature fracture.

Determining an accurate way to measure bone quality can be difficult. However, properly assessing bone quality is vital for identifying and treating bone diseases like osteoporosis. Most of the literature on the subject defines bone quality based on mineral content. In addition to mineralization, architecture, turnover (remodeling), and damage accumulation are key components that have been identified to define the mechanical quality of bone [6]. Finally, measures of the mechanical properties of bone would provide the most direct assessment of bone quality. While measuring mechanical properties is not currently used for assessment in the clinic, laboratory methods can be applied to animal models for diseases and treatments, have been applied in the work for this thesis and will therefore be addressed in the final section of this chapter.

2.1 Architectural, or Structural, Properties of Bone

There are many clinical methods, invasive and noninvasive, that can be used to characterize bone quality. Although highly invasive, histological processing of bone biopsies is the most accurate method used to investigate bone structure. With this technique, the excised bone tissue provides a snap shot of the current state of bone within a patient. From a biopsy, cross-sectional area, perimeter(s) of structures within the cross-sectional area, distances between and number of features within an area can serve as primary measurements [35]. Additional primary measurements include tissue volume (TV) and bone volume (BV) [35]. These attributes provide a structural profile of individual features which can stand alone and do not require referents. Use of referents allows for further interpretation of the specimen. For example, bone volume fraction (BV/TV) is a characteristic which is indirectly measured from bone by dividing BV by TV. Although histological assessment of a biopsy may provide as accurate a representation of bone quality as currently possible, obtaining the biopsy, usually in the form of a 7-8 mm diameter plug (Figure 1.12) from the iliac crest is painful for the patient. Advances in imaging technology may provide less invasive and safe monitoring of bone quality.

2.2 Measurement of Bone Mineral

2.2.1 Bone Mineral Density (2D)

Noninvasive measurements of the mineralization process in bone serve as strong indicators of bone quality and risk of fracture. The current clinical gold standard for assessing fracture risk is achieved by measuring bone mineral density (BMD) through the

use of dual-energy x-ray absorptiometry (DEXA) [36]. DEXA measures areal bone mineral density (aBMD), providing a global assessment of bone's mineral substance due to x-ray attenuation by the tissues of the body. aBMD (g/cm^2) is the amount of bone mass per unit area [38]. Therefore, DEXA imaging provides a two-dimensional (2D) representation of the mineral content within bone independent of bone size and tissue type [39].

Although DEXA provides a global assessment of the mineral content in bone, its 2D representation of bone quality may prove misleading as in the case of fluoride treatments that greatly enhanced both DEXA-measured BMD *and* fracture risk. Two other significant limitations of DEXA are that it does not distinguish between cortical and cancellous tissues, and gender and skeletal region have a large influence on the values reported [39].

2.2.2 Mineralization of Bone

As described previously in Chapter 1, Boivin *et al.* [2000] suggested that osteoporotic women treated with alendronate experience an increase in bone strength as a result of increased mean degree of mineralization of bone (MDMB) [30]. Using x-ray techniques similar to DEXA but carried out on bone biopsies, MDMB (grams of mineral/cm^3 of bone) indicated changes in bone mineralization due to treatment. Measurements on biopsies from 53 postmenopausal osteoporotic women treated with alendronate for 2 or 3 years suggested that the treatment leads to a prolonged secondary mineralization phase that in turn increases MDMB (Figure 2.1) [30]. The authors hypothesized that this increased mineralization was due to reduced activation frequency of remodeling BMUs.

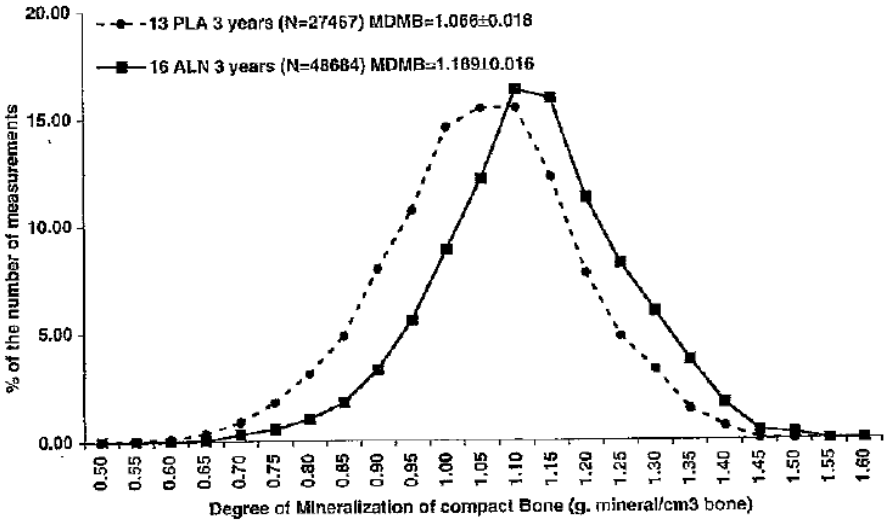

Figure 2.1 Bell-shaped curves depicting the degree of mineralization in compact bone from iliac crest biopsies. Alendronate treatment shifted the curve to the right, indicating an increased mineralization [30].

2.2.3 Bone Mineral Density (3D)

Recent advancements in technology have brought improved methods for investigating bone mineral composition in three dimensions (3D) that make distinctions between cortical and cancellous bone tissue possible [39]. Quantitative computed tomography (QCT) and high-resolution peripheral quantitative computed tomography (HR-pQCT) are two such techniques [39]. In contrast to 2D-DEXA or conventional x-rays, CT techniques allow 3D recreations using computer software. This allows depth or thickness measurements and quantification of volumetric bone mineral density (vBMD) [35,39,40]. In the investigation for this thesis a similar CT technique was utilized to determine vBMD with even finer detail. This is known as *ex vivo* micro-CT. Micro-CT can be used on biopsies harvested from humans or animal models to measure mineralization and architecture at resolutions below 20 µm. *In vivo* lab and clinical CT have more limited resolution, approaching 100 µm, but allow several longitudinal time-point measurements

to be made on the same tissue area as adaptation to a treatment occurs over weeks to years.

2.3 Turnover, or Remodeling

Biochemical markers of bone resorption and formation serve as a minimally invasive technique for investigating overall bone cell activity. Markers of bone resorption include both plasma and urine derived markers, specifically tartrate-resistant acid phosphatases (TRAP) and hydroxyproline respectively. During normal bone turnover, osteoclasts release TRAP into circulation at a relatively constant rate. However, metabolic bone disorders which result in increased bone turnover exhibit elevated plasma TRAP levels. Hydroxyproline accounts for about 13% of the total amino acid content of mature collagens and about half of the body's collagen resides within bone [66]. Upon collagen degradation, molecules free hydroxyproline that are not able to be reused for the synthesis of new collagen. Therefore, a large majority of endogenous hydroxyproline present in urine can be attributed to collagen degradation from bone [66]. Changes in the concentration of TRAP and hydroxyproline suggest alterations in bone resorption.

Serum derived markers, such as alkaline phosphatase (ALP), osteocalcin (OC), and procollagen type I propeptides (PINP), serve as biochemical markers for bone formation. ALP is an enzyme which plays an important role in the formation of osteoid as well as the mineralization process [66]. ALP activity in serum is largely attributed to bone formation. Synthesized by osteoblasts, OC is a small protein which binds hydroxyapatite [66]. Levels of serum OC associated with osteoblast activity serves as a biochemical marker as levels of OC correlate with bone formation rates [66]. Derived

from collagen type I, these peptides form both amino (N-) and carboxy (C-) terminal extension peptides which can be attributed to type I collagen formation. Changes in the presence of these biochemical markers indicate bone formation.

2.4 Damage Accumulation

Two possible consequences of altering remodeling activity in cortical bone are changes in the numbers or sizes of vascular pores of the Haversian systems, and/or changes in the numbers or sizes of microdamage. In either case the differences compared to normal, untreated bone, that may arise can be thought of in terms of damage accumulation within the tissue.

2.4.1 Porosity

In terms of total bone volume, human cortical porosity is about 2-3%, and cancellous porosity can range from 70-80% [1]. As described in the introduction, bone has a highly sophisticated network of blood vessels which run both longitudinally and horizontally throughout the mineralized structure. Maintenance of these features allow for proper nutrient and waste exchange. Therefore, any alterations in bone porosity can directly and indirectly affect the mechanical integrity of bone as a structure. Despite the known detrimental effects of altered porosity few studies have investigated porosity in bone treated with a bisphosphonate.

A decade ago, Roschger *et al.* [2001] examined mineral density, mineral/collagen composition, and the porosity of cortical bone from iliac crest biopsies of postmenopausal osteoporotic women. This investigation demonstrated significant

increases in structural and mineralization uniformity with alendronate, compared to placebo control. The most compelling result was a highly significant reduction (-46%, Figure 2.2) in cortical porosity in the alendronate treated group [41]. The authors suggested that significant increases in porosity can lead to brittle bone and increased risk of fracture. Therefore, alendronate could contribute to the observed reduction in fractures.

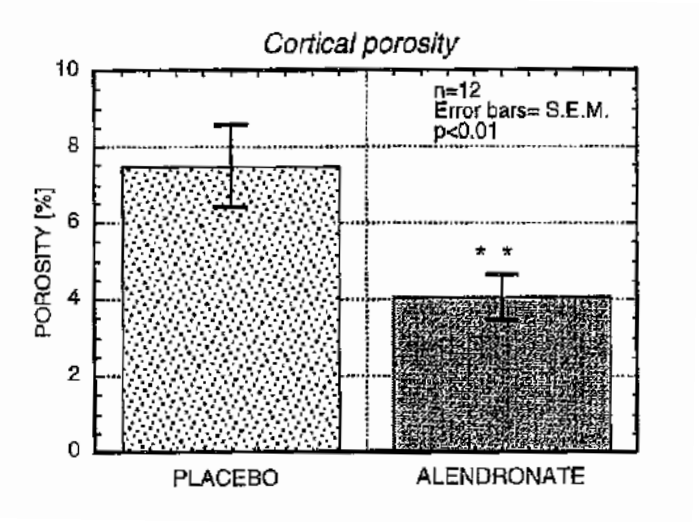

Figure 2.2 Cortical porosity measurements for placebo and alendronate treatments in osteoporotic women. Alendronate treatment significantly reduced porosity [41].

2.4.2 Microdamage

The presence of microdamage within bone tissues has been well documented [42-45]. As previously described, microdamage is the formation of minute cracks within bone, which arise during daily cyclic loading as a mechanism of energy dissipation. It is generally accepted that, as bone ages and remodeling becomes unbalanced, damage begins to accumulation within bone tissue. This notion has been confirmed by Diab and Vashishth, who used enbloc staining to demonstrate differences in the amount and patterns of microdamage accumulation among old and young bone tissues. Sharply defined lines

were identified to be linear microcracks and areas of pooled stain were identified as diffuse damage [43,44]. Results from this investigation showed that older bone exhibited significantly more linear microcracks than young bone, while young bone exhibited significantly more diffuse damage than older bone tissues [45]. Additionally, this investigation has shown that linear microcrack formation initiates within interstitial bone and is either confined to this region or arrested by cement lines [45]. Similar histological processes have been utilized to investigate microdamage accumulation in canines treated with bisphosphonates [33,47,48].

Previous studies have demonstrated that bisphosphonate treatment results in increased microdamage accumulation using canine models. An investigation of bone turnover, microdamage accumulation and biomechanical properties of bone conducted by Allen *et al.* [2006] provides insight into the affects of bisphosphonate treatment on damage accumulation. Following 1 year treatment with clinical doses of risedronate or alendronate, these authors have shown a significant increase in damage accumulation in treated bone when compared to untreated bone [47]. While this investigation was not able to identify a correlation between microdamage accumulation and reduced mechanical properties, a significant non-linear correlation between damage accumulation and activation frequency was identified. However, comparison of individual treatments and microdamage yielded data which suggests that suppression of remodeling does not act as an accurate predictor of microdamage accumulation [47].

To further illustrate the complications of microdamage accumulation and its association with reduced activation frequency and mechanical properties, Allen and Burr have demonstrated that the increase in damage accumulation associated with

bisphosphonate treatment occurs early in treatment [48]. In a similar study, histomorphometric analysis of canines treated with alendronate for 1 and 3 years yielded no significant increase in damage accumulation based on treatment duration [47]. While this investigation did identify higher microcrack density in 3 year treated verterbral trabecular bone, the accumulation of microdamage was not found to be significant. These authors suggest that while microdamage can be associated with turnover suppression, this affect is observed only early in treatment and does not progress in longer treatment duration [47].

2.5 Determining the Mechanical Properties of Bone

2.5.1 Whole Bone vs Tissue-Level Mechanical Tests: Importance of Specimen Size

Conducting whole bone mechanical tests provides a "global assessment" of bone's mechanical integrity [49]. Values of strength, stiffness, and the amount of energy to failure (toughness) can be determined, providing insight into the functional integrity of the skeleton. For example, Mashiba *et al.* [2000] suggested that short-term (12 months) alendronate treatment leads to alteration in the cortical microstructure of dog ribs which in turn alters the bone's mechanical integrity. While no difference was found in strength and stiffness, there was a significant decrease in bone toughness in the alendronate-treated group which the authors attributed, without significant proof, to an increase in microdamage accumulation [51]. Although this type of whole-bone analysis provides useful mechanical information, the contribution of individual features within the tissue, including microstructure and microdamage, can only be implied.

While whole-bone testing considers how the bone as a complete structure responds to load, tissue-level mechanical testing explores bone tissue independent of the size and shape of the whole bone [49]. Quality and quantity of collagen fibers, as well as mineral density, play a central role in determining tissue-level mechanical properties such as elastic modulus and ultimate stress [50]. By investigating the mechanical properties of uniform bone beams across different treatments, changes due to the architectural make-up of bone can be characterized. For the investigation in this thesis, bone beams were excised from the cortices of canine ribs and mechanically tested in bending.

2.5.2 Methods of Mechanical Testing

Tension, compression, bending, torsion and shear tests serve as ways to assess mechanical properties (Figure 2.3). The goal of these tests is to determine the stiffness, load to failure and total energy absorbed prior to failure for the structure or material in specific loading modes.

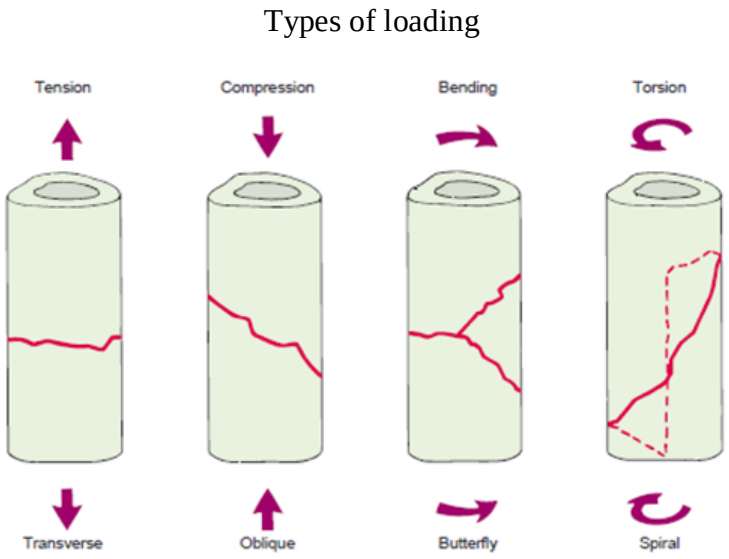

Figure 2.3 Tension, compression, bending, and torsion are four ways in which a bone can experience load. Engineers utilize techniques that test materials under these conditions to investigate mechanical properties. Depending on the direction of the applied force, unique fracture patterns are exhibited in the cortical shaft of a long bone [52]. In practice, loading as shown here results in mixed modes of loading at the tissue-level. Shear loading is one mode present under nearly all loading conditions, is not shown here and is difficult to obtain as a pure mode in practice [53].

In tension and compression tests the ends of the specimen are either pulled away from or pushed toward one another, effectively elongating or compressing the specimen, respectively. In general, specimens are prepared such that the majority of strain will be concentrated in the central portion of the specimen. Whole-bone and tissue-level mechanical properties have been measured in cortical bone [54]. The stresses developed in a sample during this type of uniaxial loading are directly related to the cross-sectional area of the sample.

Since long bones are subject to large bending forces during normal function, tests that utilize bending forces provide useful data on mechanical properties [33,54,55]. To perform a bending analysis the load is applied perpendicular to the longitudinal axis, placing one surface in tension and the other in compression [54]. Cross-sectional

moments determine resistance to bending and are measured along the axes that contains the center of mass [56]. Bending tests are generally conducted under either three- or four-point configurations (Figure 2.4). The three-point configuration may create high shear stress within the mid-span of the test beam [56]. For this investigation, the 4-point bending configuration was used to minimize the amount of internal shear stresses within the bone beams and not introduce artificial stress concentrations at the mid-span.

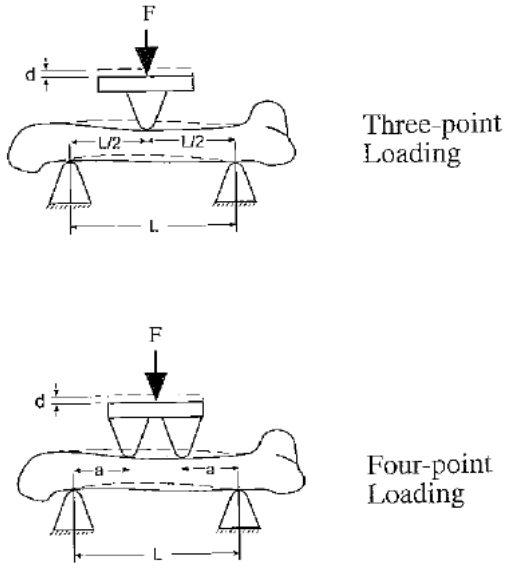

Figure 2.4 Bending can be applied to whole bones, as well as machined beams in either 3- or 4-point configurations [56].

Allen *et al.* [2008] demonstrated changes in whole-bone mechanical properties, namely decreased post-yield bone toughness, by subjecting whole ribs to 3-point bending to failure, following three years of bisphosphonate treatment. Toughness represents the capacity for energy to be absorbed prior to fracture. Although changes in post-yield toughness have not been clinically defined, it is generally accepted that a reduction inhibits bone's ability to resist fracture [56]. Interestingly, no differences were found between the groups for ultimate load or stiffness. The reduction in toughness (~20%) was

most pronounced in the higher alendronate-dosed group (Aln 1.0 mg/kg) when compared to control [33].

Torsion is applied with twist about a single axis of rotation. The polar moment of inertia, which represents the addition of both maximum and minimum moments in bending, largely determines resistance to torsion. The torsion test can provide properties of shear when applied to a prismatic beam of constant cross-section. Unfortunately, the most closely prismatic of long bones does not present a good approximation of even a straight cylindrical tube and torsional tests are extremely difficult to perform correctly [57].

2.5.3 Quasi-Static versus Dynamic Loading

Bone normally experiences a large range of loads and loading rates. Therefore, it is plausible to subject bone to one of the previously described modes of loading at different rates in the laboratory. The application of a steadily increasing load to a test specimen until fracture is known as monotonic, or quasi-static loading. Monotonic testing determines properties of stiffness, yield load, ultimate load, and elastic and plastic deformations [56]. However, monotonic testing does not represent the way in which bones are loaded daily in normal use. A more realistic approach to investigate bone properties is with cyclic, or fatigue, loading. In fatigue, cyclic loads are applied until failure to determine the number of cycles, or fatigue life, of the structure or material.

During fatigue the progressive failure of a specimen is monitored. Specimens will fracture at stress levels much lower than those required to fracture the material under quasi-static loading [58]. The reason for this is that cyclic loading causes micro-

architectural structures within the material to break down, ultimately leading to fracture [59]. Fatigue-life is generally characterized using a stress-life diagram, also known as an S-N curve. Since testing of individual specimens is to failure the generation of a S-N curve requires multiple specimens of uniform geometry to be tested under various stress amplitudes with the number of cycles to failure recorded for each [58,60]. From this diagram, values of fracture strength (σ_f) and endurance strength (σ_e) can be determined. Depicted in Figure 2.5 are the results of a fatigue study of both cortical and cancellous bone from human cadavers [60]. σ_f of cortical bone and cancellous bone were 210.2 MPa and 134.4 MPa, respectively. σ_e was 150 MPa in cortical bone and 83 MPa in cancellous bone.

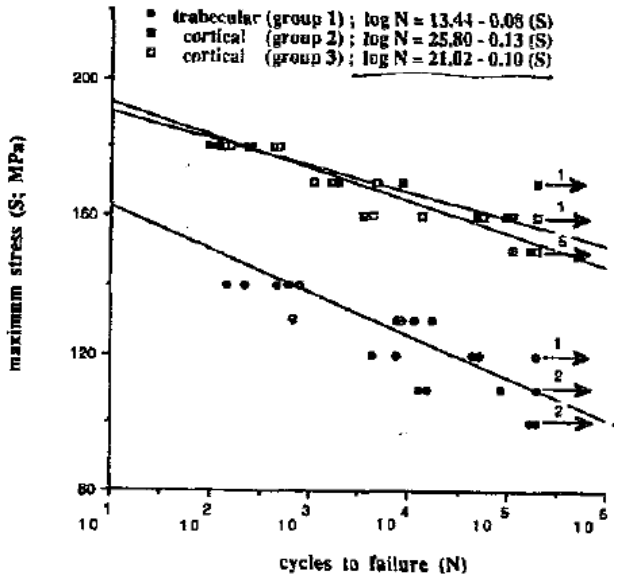

Figure 2.5 Fatigue-life diagram of cancellous and cortical bone specimens. The y-axis represents the stress at which bending was applied. Along the x-axis is the number of cycles to failure [60]. Note: cycles to failure is plotted on a logarithmic scale.

2.6 The Relevance of Measuring Bone Quality after Drug Treatment

Presented here are pertinent publications in which the biomechanical safety and efficacy of bisphosphonate drugs for dosage, treatment duration, and insertion of a "drug

holiday" were investigated. Additional manuscripts exploring a possible association of bisphosphonate use with low energy atypical fractures of the femur have also been included. All presented studies investigated either the quality or fragility of bisphosphonate-treated bone.

2.6.1 Bisphosphonate Treatment Restores Bone Quality in Osteoporotics

Liberman *et al.* [1995] found that postmenopausal osteoporotic women receiving alendronate for three years had improved BMD and fracture risk profiles compared to placebo controls. A dose-dependent effect was noted for BMD. In this population, patients on placebo who had lower base-line lumbar spine BMD values demonstrated high incidences of new vertebral fractures over the course of the 3-year study. Additionally, significant loss of BMD was noted at all sites in the placebo-treated group. Conversely, BMD of the spine, femoral neck, trochanter, and total body significantly increased after 2 years with all alendronate treatment regimens [61]. While the higher dose group (10 mg/day) exhibited greater mean BMD than the lower dose (5 mg/day) at all sites, no differences in fracture risk were found due to dose.

This study was extended to investigate long term effects [62]. Patients continued their regimens through three extensions (years 4-10). In general, continued 10 mg/day alendronate treatment was found safe, yielding mean increases in BMD of 14% in the spine, 5% in the femoral neck, 10% in the tronchanter, and 7% at the total proximal femur, compared to base-line values. Non-vertebral fractures during years 8 through 10 were highest in a group that discontinued treatment (12%) and lowest in the 10 mg/day alendronate group (8%). Again, any differences due to dose were not found statistically

significant. The authors argued that discontinuation of alendronate treatment will cause a loss in bone quality.

In a short-term study conducted by Cummings *at al.* [1998] referred to as the Fracture Intervention Trial (FIT), alendronate administration was investigated in women with low BMD. Patients were assigned to either placebo or 5 mg/day alendronate groups. After two years, the alendronate treatment was increased to 10 mg/day for two years. Again, alendronate treatment was deemed safe and effective at restoring BMD at all sites, and decreasing vertebral fracture risk by about half. After four years, placebo patients had lost an average of 1% BMD from their femoral neck, while alendronate-treated gained 4%. Similarly, an average loss of 2% BMD was observed in the total hip of placebo patients, while alendronate treated patients exhibited a 3% increase.

2.6.2 Possible Implications of Discontinuation of Treatment or "Drug Holiday"

The bulk of the literature supports the view that bisphosphonates are an effective method to restore bone quality in osteoporotic patients. However, many doctors and patients believe that long-term administration can lead to adverse changes in bone quality that might lead to fracture. In light of this, a "drug holiday" has been advocated in which patients receiving bisphophonates are prescribed time away from drug treatment. Detractors argue that discontinuation of treatment will cause a loss in bone quality.

The most comprehensive study addressing the discontinuance of bisphosphonate treatment was the extension of the FIT trial, known as the FIT Long-term Extension (FLEX). After the first five years of treatment, alendronate was either continued or discontinued for the next five years [37]. Women who received alendronate at either dose

(5 or 10 mg/day) for the total ten-year period maintained BMD at the total hip and had suppressed remodeling compared to those switched to placebo. However, and most significantly, women who discontinued alendronate treatment showed no increase in fracture risk compared to those who continued treatment. Whether the fracture-risk benefit of taking alendronate for 5 years will persist beyond a 5 year "holiday" is unknown.

2.6.3 Atypical Fracture: A Case of Decreased Cortical Bone Quality

Though administration of bisphosphonates has proven successful in osteoporotic patients at reducing the risk of fracture [36,37], recent publications have suggested that the drug may be linked with atypical fractures of the femur [63,64]. This is a difficult case to prove. There are many factors which contribute to an individual's risk of fracture, usually ahead of bisphosphonate drugs. Daily habits, like diet, smoking and exercise, can play key roles in one's bone quality. Slight differences in genetics that affect metabolic pathways can also account for difference in the structural and material properties of bone. Pre-existing disease, like diabetes, can significantly affect bone quality. There is no way to ensure that patients are 100% compliant with their drug regimens when bisphosphonates are prescribed. All these factors make for difficulty in differentiating the risks of bisphosphonates.

2.6.4 Low Energy Fractures Associated with Alendronate

In a recently published case study, Neviaser *et al.* [2008] were able to identify a radiographic abnormal or atypical fracture pattern of the femoral shaft consistent with patients treated with alendronate resulting from low energy trauma. Characteristic of this atypical fracture was the beaking of the cortex and hypertrophied diaphyseal cortices around the fracture site, as well as the transverse pattern of fracture across the midshaft [65]. Additionally, this investigation identified the fracture occurring from minimal or no trauma. Of the 70 total patients identified to have had fracture resulting from low-energy trauma, 25 had been using alendronate [65]. The exact treatment regimen was determined for 16 of the 25 individuals taking alendronate. The duration of treatment for the 10 individuals which exhibited atypical fracture was 6.9 years, while the remaining 6 individuals who did not exhibit this fracture pattern had an average duration of 2.5 years [65]. More significantly, 19 of the 20 patients which were identified to have exhibited this atypical fracture pattern were taking alendronate [65].

2.7 Measuring Bone Tissue Quality Under Dynamic Loading

This thesis explores new methods for measuring bone tissue quality after drug treatment; fatigue analysis after bisphosphonate treatment has not previously been explored. Fatigue offers testing in a more “real–life” mode of loading. Further, the mechanical tests developed allow assessment of whether a bisphosphonate’s ability to prevent biomechanical property degradation at the structural level comes with any other effects at the tissue level. To fully understand the effects of a drug on bone quality, it is imperative to measure biomechanical properties at all levels of composition.

This work also addresses the question of how bisphosphonate treatment might play a role in atypical fracture. As discussed previously, treatment for up to five years improves BMD [47,48,33,29,30] and reduces fracture risk [37]. Bisphosphonate usage slows down the rate of turnover thus decreasing the rate of bone loss. However, recent articles demonstrate that long-term bisphosphonate use may be associated with atypical fracture of the femur [67,68,69]. To investigate possible mechanisms behind these fractures this investigation was designed to develop a novel approach for investigating tissue-level bone quality, particularly mechanical properties.

CHAPTER 3

METHODS AND MATERIALS

An experimental study was designed to characterize the influence of a bisphosphonate on the fatigue-life of cortical bone tissue. Bone tissues tested in this investigation are part of a collaborative effort between the labs of Drs. David B. Burr and Matthew J. Allen of the Indiana University School of Medicine and the group of Dr. J. Christopher Fritton at the New Jersey Medical School. The work encompassed in this thesis included specimen preparation of bone tissue beams, that were then mechanically tested, imaged with optical microsocopy and quantified for histomorphometrical features. Details pertaining to the animal model from which bone tissue beams were tested for this thesis, are described in detail elsewhere [33]. Pertinent methods are presented here for a complete understanding of the current study.

3.1 Animal Model

Thirty six skeletally mature female beagles between 1 and 2 years of age were treated daily with an oral dosage, based on body weight, of either vehicle control (Cont, 1mL/kg saline) or alendronate (Aln, 0.2 mg/kg or 1.0 mg/kg; Merck, Rahway, NJ) for 3 years. The low dose of Aln (0.2 mg/kg) corresponds to that used for the treatment of postmenopausal osteoporosis, and the high dose (1.0 mg/kg) is equivalent to that used for treatment of Paget's disease. At 3 years, the dogs were sacrificed by intravenous administration of sodium pentobarbital (0.22 mg/kg Beuthanasia-D Special; Schering-Plough, Union, NJ). Bones were excised, cleaned of soft tissue, wrapped in saline-soaked

gauze and frozen at -20ºC (Allen 2008). For the present study, the 11th rib from each canine was obtained. All procedures and protocols were approved by the Indiana University School of Medicine Animal Care and Use Committee.

3.2 Specimen Preparation

Prior to bone sectioning, whole ribs were scanned using a microCT (Skyscan 1172, Belgium) along with density calibration phantoms (0.25 gm/cc and 0.75 g/cc). Scans were performed at an isotropic voxel resolution of 17 µm with the specimens submerged in a saline bath. Two ribs were scanned at a time. The images were reconstructed using NRecon software (V1.6.1.1, SkyScan) with compensation for misalignment. Cortical tissue mineral density (Ct.TMD) was measured in a 8 mm section in the mid-span.

Canine ribs were removed from the freezer and allowed to thaw at room temperature for 1 hour. All cuts were made on a semi-automated Isomet 5000 (Buehler) precision saw (Figure 3.1). The entire rib was potted in cement (Bondo®, 3M) and fixed to an aluminum plate (Figure 3.2). The first three cuts were made to divide the rib into three to four approximately equal sections. Next, primary sections, 1.5 mm in thickness, were cut from each of the four cylindrical sections (Figure 3.3). This dimension represents the maximum width that could be obtained given the curvature and the geometry of the rib bone. Primary sections, depicted in Figure 3.4 a, were bonded to a plastic slide using cyanoacrylate, a rapidly polymerizing acrylic resin, fixed to an aluminum plate and mounted on the saw. Secondary sections, 0.5 mm in thickness, were then obtained from the medial and the lateral cortex resulting in beams of rectangular

cross-section (0.5 mm x 1.5 mm) and 10 mm length (Figure 3.4 b). The limited amount of cortical bone tissue allowed for 3 to 6 beams to be successfully extracted from each rib.

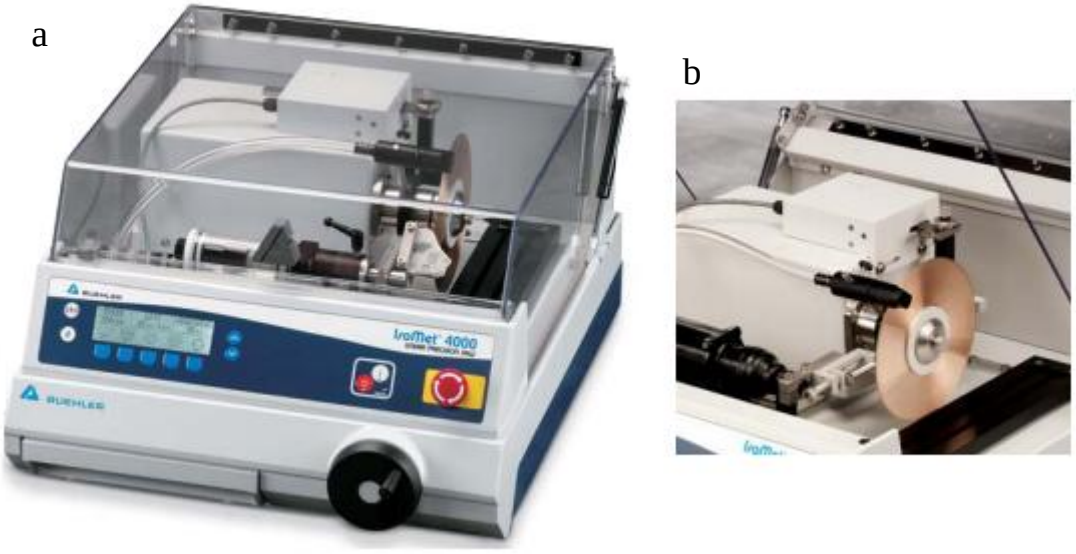

Figure 3.1 Image here is the a) Buehler Isomet 5000 precision slicer used in this study. b) A close up of the precision blade used to make cuts [70].

Figure 3.2 Depicted here is an 11th beagle dog rib potted in Bondo® and attached to an aluminum plate. This assembly was mounted on the slicer and three to four approximately cylindrical rib sections were obtained. Minor cuts made to the ends of ribs removed irregular bone geometry, depicted by dotted lines. Major cuts made to cut rib into cylindrical sections, depicted by dot hashed line.

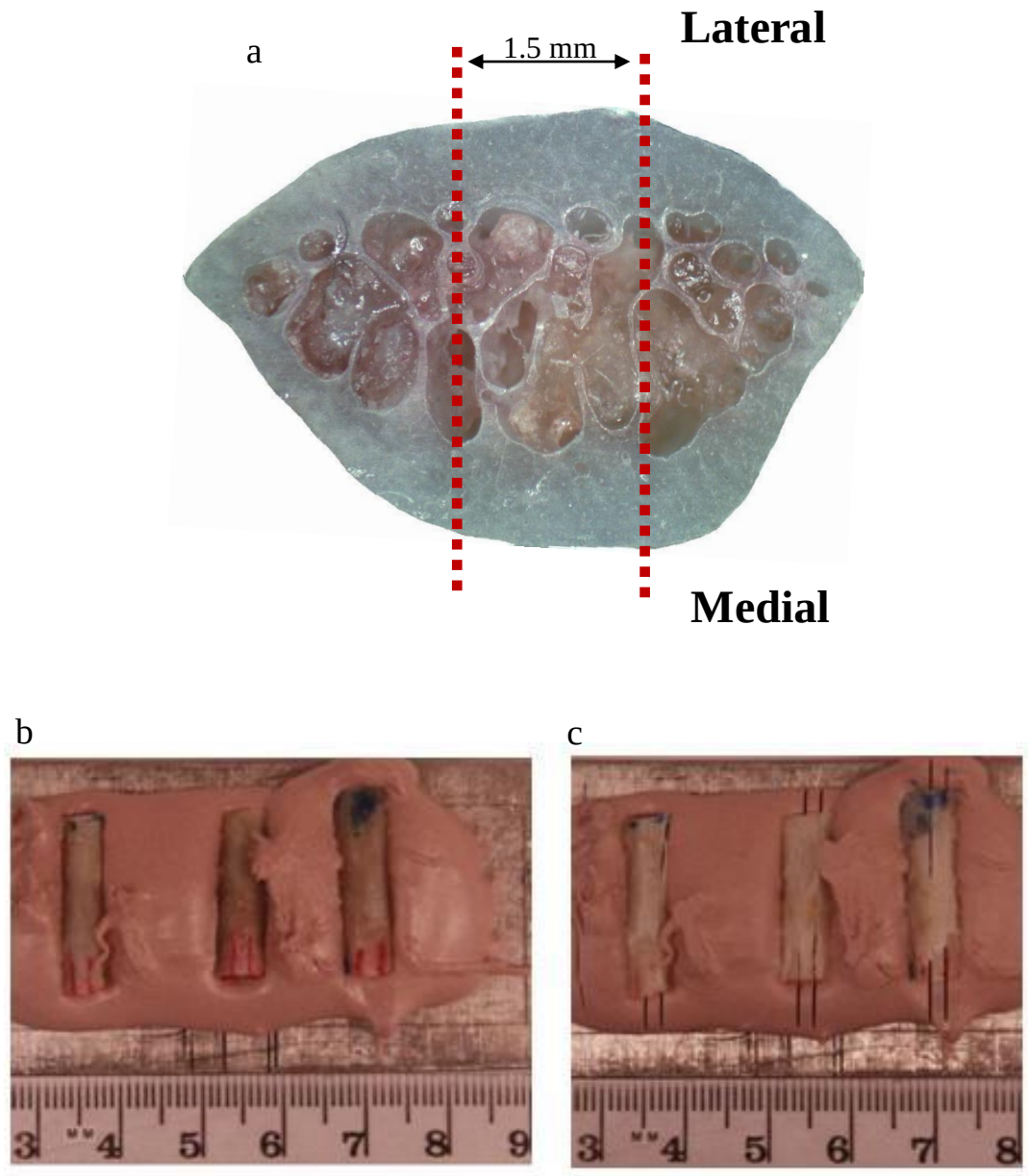

Figure 3.3 a) Cross-section of a cylindrical section with medial and lateral cortices labeled. A primary cut, 1.5 mm in length, is illustrated in red dashed lines. b) Cylindrical sections were again potted in Bondo®, attached to an aluminum plate, and mounted in the slicer. Marked in red is the maximum cortex in each rib section. c) Primary section cuts, 1.5 mm in thickness, were made using the previously described methods along the red lines.

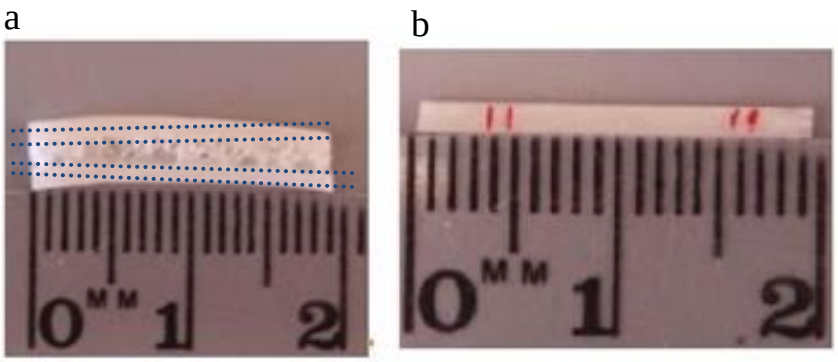

Figure 3.4 From each primary section, both a lateral and medial beam was cut from a region of maximum cortex. a) Imaged here is a primary section, 1.5 mm in thickness. b) Secondary bone beams were cut from primary sections, using the previously described method, to produce beams of rectangular cross section (0.5 mm x 1.5 mm) and 10 mm in length. Imaged here is the periosteal side of a beam.

3.3 Mechanical Fatigue Testing Setup

Beams were mounted onto a 4-point bending fixture with the periosteal side in tension and the endosteal side in compression. The beams were then cyclically loaded using a TestBench system (Electro Force, Bose) with 225 N load cell and displacement transducer. All tests were conducted with the specimen submerged in a saline bath (Figure 3.5 a). The upper (loading) fixture pins were 2 mm apart, while the lower (support) fixture pins were 6 mm apart (Figure 3.5 b, c). For proper alignment, the beam was placed in shallow groves located within the center of the lower fixture (Figure 3.5 d).

Prior to cyclic loading, a small preload of 0.4 N was applied using the preset function in the Wintest Software (Version 4.1, Bose Enduratec) and the load cell was tared to zero. Additionally, load and displacement limits were established to prevent the fixtures from coming into contact with one another and potentially damaging the load cell. Fatigue loading was carried out under load control at a frequency of 2 Hz until, either the beam fractured (N_f) or the cycles reached a predefined number of $2.5X10^5$. Each beam was cyclically loaded at one predetermined stress value (Figure 3.6). The

stress amplitudes (σ_a) used in this investigation ranged from 45 to 85 MPa. Loads and load-line displacements were recorded at 100 Hz for 0.5 sec, representing 1 cycle, at specific increments over the fatigue life. Cycle sampling of the collected data varied depending on the preselected σ_a values, as well as the N_f. To best represent any changes in material properties, cycles were sampled at positions which represent the major intervals of the logarithmic scale of the plot. In all cases, the sampling was selected to accurately capture the loss of modulus over time.

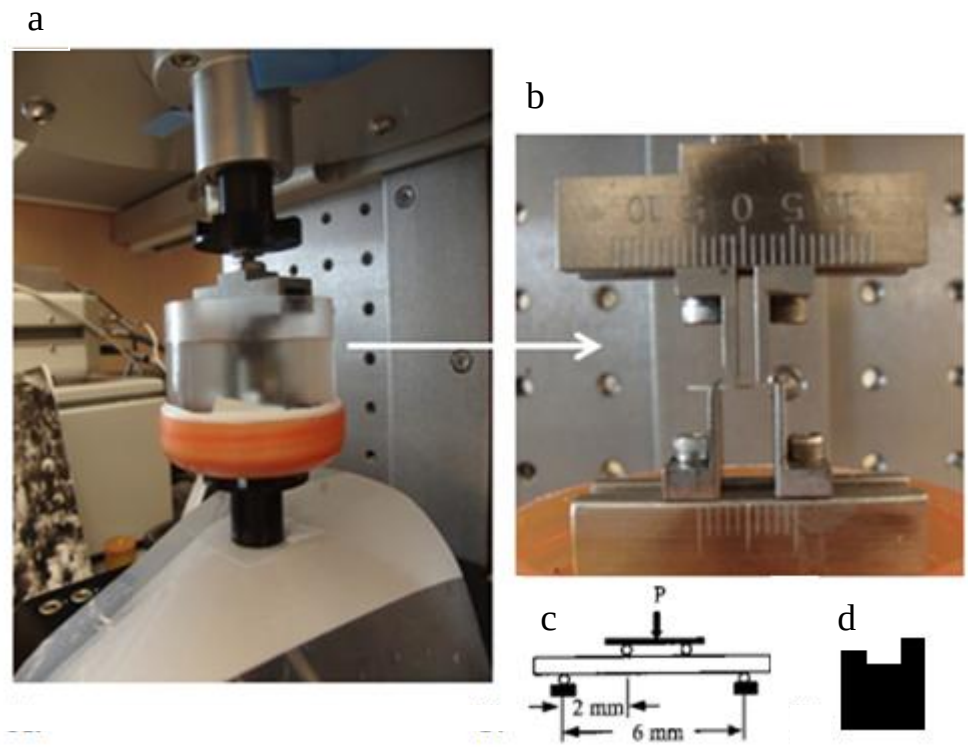

Figure 3.5 a) Bose Test Bench loading system, with saline bath to keep specimen hydrated. b) 4-point bending fixture with beam between grips. c) Schematic of 4-point bending configuration. d) Side view of lower fixture, illustrating the grooves which hold the sample in place (not to scale).

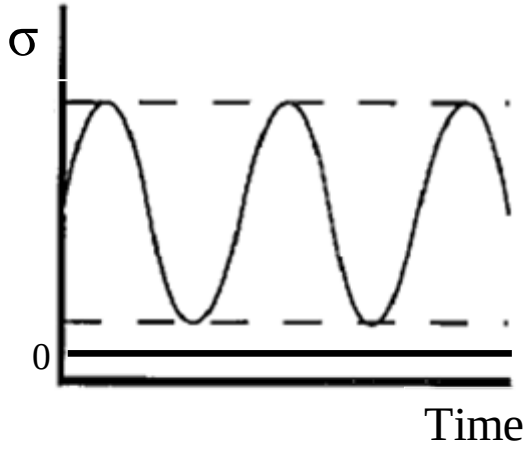

Figure 3.6 Preselected σ_a provided maximum and minimum stress values at which a particular bone beam was fatigued between [71].

Stress (σ), the measure of average force per unit area acting on a body, and strain (ε), the measure of deformation, were calculated using specimen geometry and sampled values of load and load-line displacement [59]. Using simple beam theory, values of applied σ and ε were obtained using the following equations:

$$\sigma = \left(\frac{3a}{bh^2}\right) P$$

$$\varepsilon = \left(\frac{3h}{a(3L-4a)}\right) \delta$$

where a is the distance between the inner and outer supports, L is the distance between the outer supports (Figure 3.5 C), b and h are the specimen thickness and height, respectively, P is the applied load and δ is the load-line deflection.

3.4 Fatigue-Life Analysis (S-N Curve)

The fatigue-life of bone beams were characterized using stress-life diagrams (S-N curves). Multiple specimens of the uniform geometry previously described were subjected to a range of σ_a values and the number of cycles to failure (N_f) were recorded. Beams were tested until either fracture or 250,000 cycles were reached. Once completed, σ_a was plotted as a function of N_f to generate a S-N curve. Distribution in the S-N curve was modeled using the following power law:

$$\sigma_a = A(N_f)^B$$

where A and B are the fatigue-life coefficient and exponent, respectively.

From the S-N diagram, fatigue properties were determined, including values of fatigue fracture strength (σ_f) and endurance strength (σ_e). σ_f represents the amount of σ needed to propogate an existing crack or flaw and was determined by finding the y-intercept of the S-N curve at the cycle 1 [71]. This value is also represented as the fatigue life coefficient (A) generated using the previously described power law. Theoretically, the stress below which a material will show no evidence of failure under fatigue loading is known as σ_e [71]. Using a power fit, this value can be determined for each bone beam.

3.5 Elastic Modulus

Investigation of the relationship between σ and ε provides basic material properties, as depicted in Figure 3.7. Forming a straight line, the region between points O and P (O representing the origin where no load is applied and P representing the proportionality limit) demonstrates that any change in stress will result in a linearly proportional change in strain [72]. Just beyond the proportionality limit is the elastic limit, denoted as E. This

value represents the maximum amount of stress that can be applied to a material in which no permanent deformation will occur. If subjected to σ values above this limit, the material will no longer resume its original shape and size upon unloading [72]. Just beyond the elastic limit is the yielding point, denoted as Y, and the yield strength, denoted as σ_y. At this point, extensive elongation, or yielding, can take place without a corresponding increase in load [72]. At point U, the maximum amount of σ is applied to the material without causing fracture. This is known as ultimate strength (σ_u) of the material. Representing fracture or rupture of a material, point R depicts what stress the material will fail under loading.

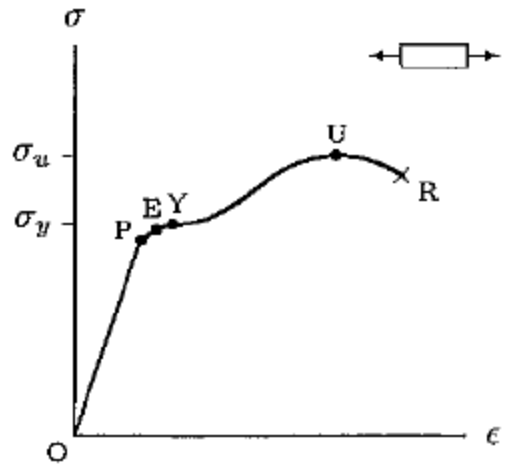

Figure 3.7 General stress-strain curve of a material. Point O represents the origin where there is no initial load or deformation. Point P represents the proportionality limit. Point E represents the elastic limit. Point Y represents the yield point. Point U represents the ultimate strength of the material. Point R represents the point of rupture or fracture of the material [72].

As force is applied to a material, that material will tend to deform. A materials tendency to behave in an elastic manner, where an increase in σ results in a linearly proportional increase in ε, is described as Young's Modulus or elastic modulus (E) and can be determined by investigating σ and ε behaviors of the material. Fatigue damage can

be monitored by E degradation. Reported as a ratio of initial modulus or percent loss in modulus, the most common ways to quantify elastic modulus (Figure 3.8), are by measuring (1) the maximum beam deflection using linear elastic beam theory (LEBT) [43,73,44 ,74], (2) the unloading stiffness [75,76,77,78,79,80,81,82,83], (3) the secant stiffness [84, 42,77,85,86], and (4) the tangent or loading stiffness [76]. Of these four methods for quantifying elastic modulus or stiffness degradation, secant stiffness has demonstrated accuracy for bone [87] and was used for this investigation.

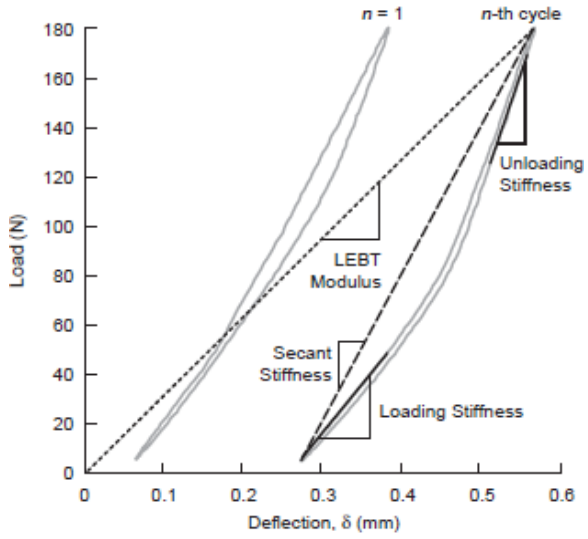

Figure 3.8 This load vs. deflection graph displays two hysteresis loops from a sample under 4-point bending fatigue. N=1 represents the initial loading cycle and the n^{th} cycle represents the final loading cycle. From these hysteresis loops, mechanical measures of damage can be quantified in terms of elastic modulus [87]. Secant stiffness and loading stiffness were evaluated in this investigation.

Hysteresis loops were generated at various cycles sampled along the logarithmic scale of cycles to failure. From each hysteresis loop generated per cycle, secant stiffness and loading stiffness were calculated [87]. The secant stiffness was calculated by determining the slope of the line which connects (σ_{max}, ε_{max}) and (σ_{min}, ε_{min}) for each

cycle (Figure 3.8). The loading stiffness was determined by a linear least square fit (R>0.95) to the initial loading portion of each hysteresis loop.

3.6 Specimen Preparation for Histomorphometrical Image Analysis

Following mechanical testing, all specimens underwent dehydration and staining for micro-structural analysis. Each specimen was stained with 1% basic fuchsin dissolved in ascending concentrations of ethanol (80%, 90%, and 100%) for 48 hours at each. (Appendix A). After sequential staining, samples were washed with 100% ETOH for 1 hour to remove any excess stain. Next, each sample underwent a series of Xylene clearing to remove alcohol within the tissue. Finally, each sample was infiltrated using a series of polymethyl-methacrylate (PMMA) solutions and placed in a warm environmental room (~35ºC) to polymerize, thus embedding the sample within a plastic block (Appendix B).

The plastic blocks were then cut to obtain 300 μm thick sections, transverse to the beam length (Appendix C). The sections were polished using grinding papers (Handimet 2 Roll Grinder, Buehler) of increasing grit size, 400 to 800. Cross sections were then cleaned with 100% ETOH and fixed to plexiglass slides with acetylnitrile. Once fused, cross-section thickness was reduced to approximately 100 μm using 1200 grit grinding paper. Next, cross sections were polished using a polishing wheel (Ecomet III, Buehler) with decreasing alumina slurries (average diameters of 5.0 μm, 0.3 μm and 0.05 μm) until a mirror finish was achieved (Appendix D).

3.7 Histomorphometrical Image Analysis

Bone beam cross sections were imaged under a bright field microscope (Eclipse 50i, Nikon) at 10X magnification using an image capture camera (Q Imaging Go-5) and software (Q Capture), then stitched together using a graphics editing program (Figure 3.9 a) (Adobe Photoshop CS5). For each bone beam, three to five cross sections from the mid-span were imaged and analyzed.

Once reconstructed, cross sectional regions were analyzed for porosity, osteonal and inter-osteonal (also known as interstitial) space. Briefly, within Photoshop four image layers (perimeter, osteonal boundary, porosity with osteonal boundaries, and porosity without osteonal boundaries) were created and assigned separate colors (blue, green, yellow, and yellow respectively). Within each layer, the respective micro-structural features were outlined using an interactive pen and tablet display (Wacom Cintiq 21UX) connected to a computer workstation (Dell Optiplex GX780). Each layer was used to quantify one of the following parameters: total bone beam area, total osteonal area, total porosity within osteonal boundaries and total porosity not within osteonal boundaries. Also reported was the number of pores per cross section.

Quantification of these totals was achieved using an image processing program (NIT Image J 1.43u). Each individual layers was first imported into Image J and made binary (Figure 3.9 d, f, h, h, j). After establishing the desired measurements, Image J quantified outlined areas within the given layer. The pixel area of each layer was then converted into μm. This was achieved by imaging a calibrated scale marker at the same magnification and measuring an arbitrary length along the scale marker to determine the amount of pixels contained within the measured length. Primary measurements include

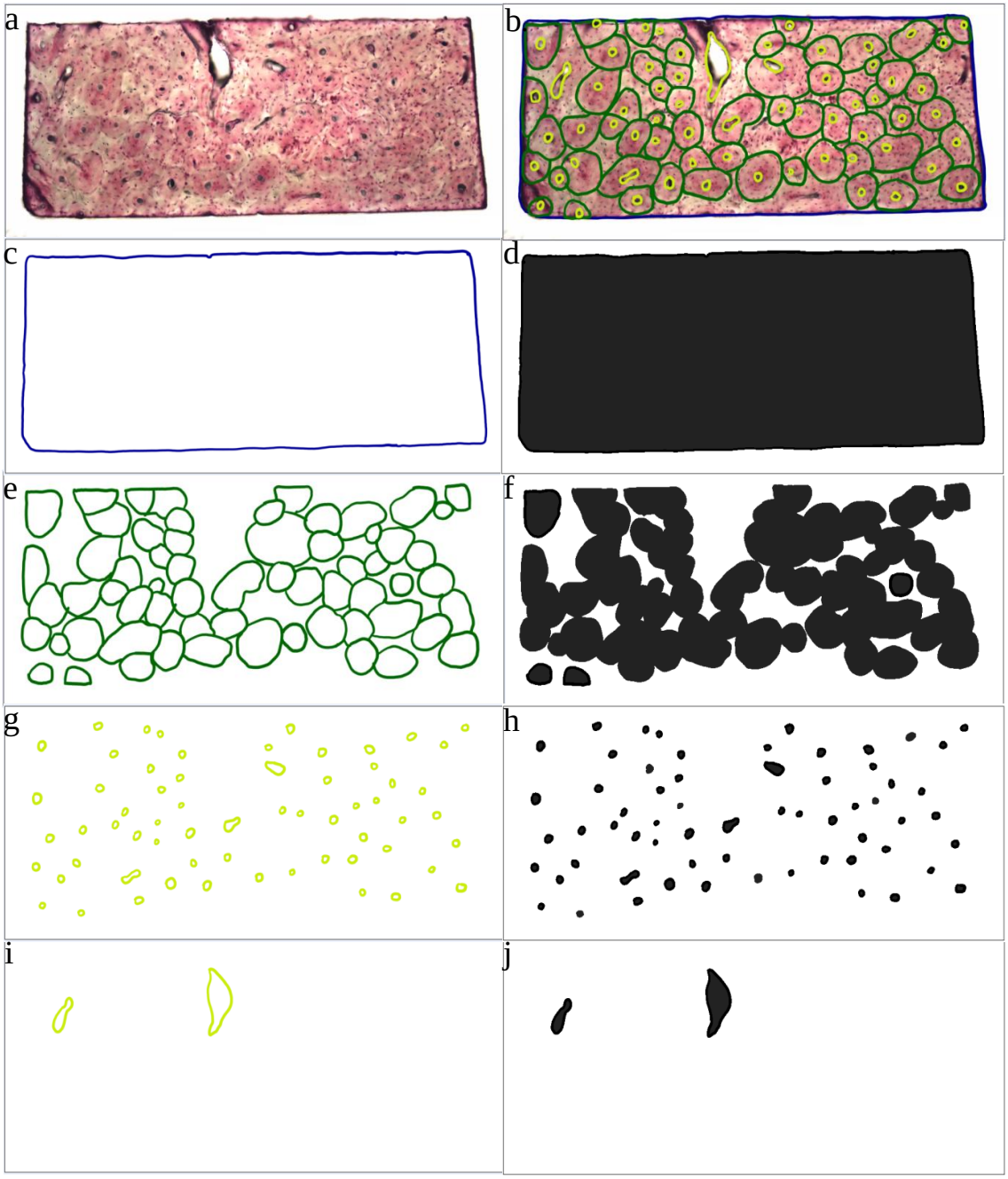

Figure 3.9 Once each cross sections is recreated, layers are added and bone parameters were outlined. a) Reconstructed cross section of a bone beam. b) All four layers of outlined features of bone displayed on bone beam. c) Blue colored outline of the perimeter. d) Perimeter made binary within Image J. e) Green colored outline of osteonal boundaries. f) Osteonal boundaries made binary. g) Yellow colored outline of porosity with osteonal boundaries. h) Porosity with osteonal boundaries made binary. i) Yellow colored outline of porosity without osteonal boundaries. j) Porosity without osteonal boundaries made binary.

total perimeter and total osteonal area. Total porosity was found by adding the total porosity with osteonal boundaries and the total porosity without osteonal boundaries. Total interstitial area was determined by subtracting the total osteonal area from the total perimeter. All areal values are reported in μm^2.

3.8 Statistical Analysis

To investigate variance among the data, methods of statistical analysis were employed. The use of non-parametric analysis of variance, specifically the Kruskal-Wallis test, was utilized to determine variance among data sets within each treatment with 95% confidence ($p<0.05$). To investigate variance between treatment groups, data sets were analyzed using one way analysis of variance (ANOVA) with 95% confidence ($p<0.05$). Post-hoc analysis was utilized to adjust for multiple comparisons in both of the previously described situations. Specifically, Bonferroni adjusted post-hoc analysis was used to correct for error which may arise when comparing multiple sets of data.

CHAPTER 4

RESULTS

The primary objective of this study was to characterize the effects of bisphosphonate treatment on tissue-level mechanical properties of cortical bone. Evaluations of the fatigue-life were conducted by applying cyclic loading to beam specimens obtained from 11^{th} ribs of beagles. In addition, microstructural evaluation was conducted using conventional bone histomorphometry techniques.

4.1 Tissue Mineral Density (TMD)

Results from the microCT evaluation showed no significant differences in the cortical tissue mineral density (TMD). The TMD for control, Aln 0.2 and Aln 1.0 was found to be 1.16±0.04 g/cc, 1.19±0.03 g/cc, and 1.15±0.06 g/cc, respectively (Figure 4. 1).

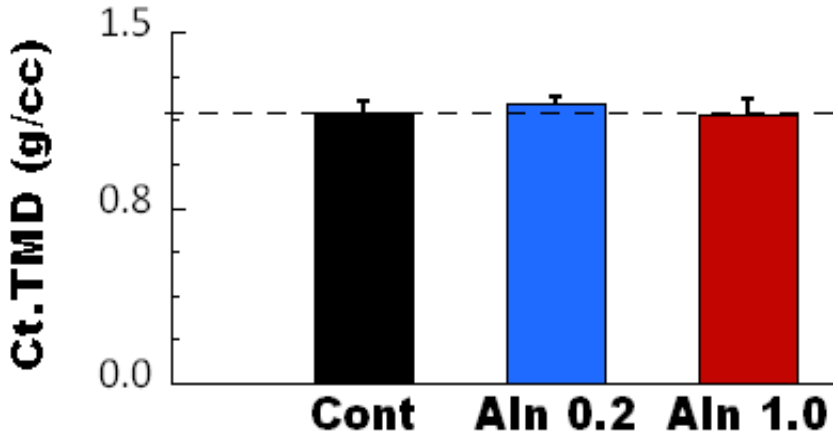

Figure 4.1 Tissue mineral density values for cortical bone in the mid-span of ribs. Results indicate that TMD is maintained throughout the treatment with no significant difference among the three groups.

4.2 Mechanical Investigation

The comparison of loading and unloading hysteresis loops for individual cycles during fatigue testing illustrates any changes in material properties as a function of cycle number. Degradation of stiffness was observed in all beams and is illustrated in Figure 4.2. As the number of cycles increased, the hysteresis loops lost uniformity, eventually leading to a non-linear loop just prior to fracture.

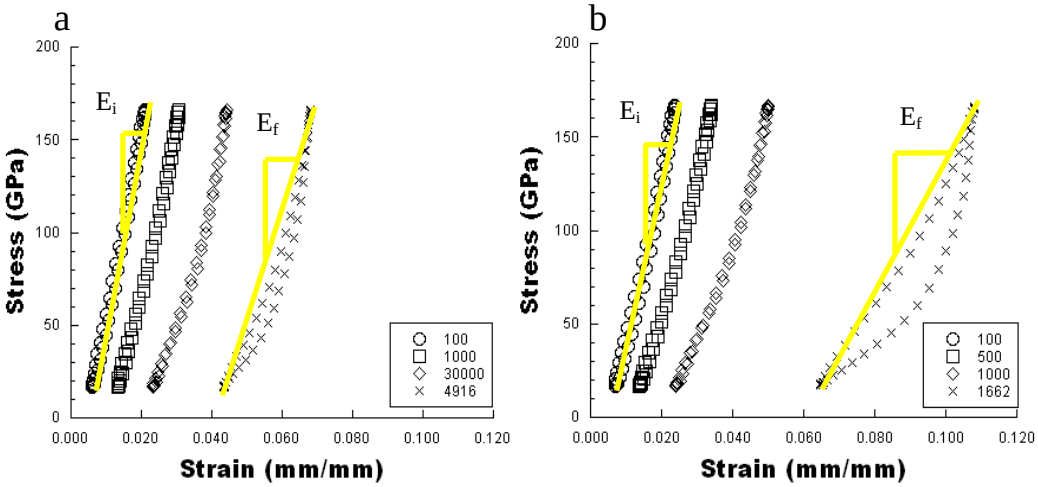

Figure 4.2 The gradual degradation of mechanical properties can be observed by stress-strain data at various cycles throughout the loading period. Both a) and b) represent bone beams tested at a stress amplitude of 75 MPa. a) Hysteresis loops illustrating stiffness degradation of a control specimen. b) Hysteresis loops illustrating stiffness degradation of an Aln 1.0 treated specimen.

Beams from the lateral cortex exhibited almost half the initial stiffness of beams obtained from the medial cortex (Appendix G). Analysis for porosity, as described in Chapter 4, showed larger average pore size in these beams with lower stiffness. Consequently, two criteria were used to detect possible outliers, stiffness and porosity. Lateral beams having an order magnitude larger pore size, and exhibiting initial stiffness

below the lower quartile of the medial beams were considered outliers (Figure 4.3) for the following analyses.

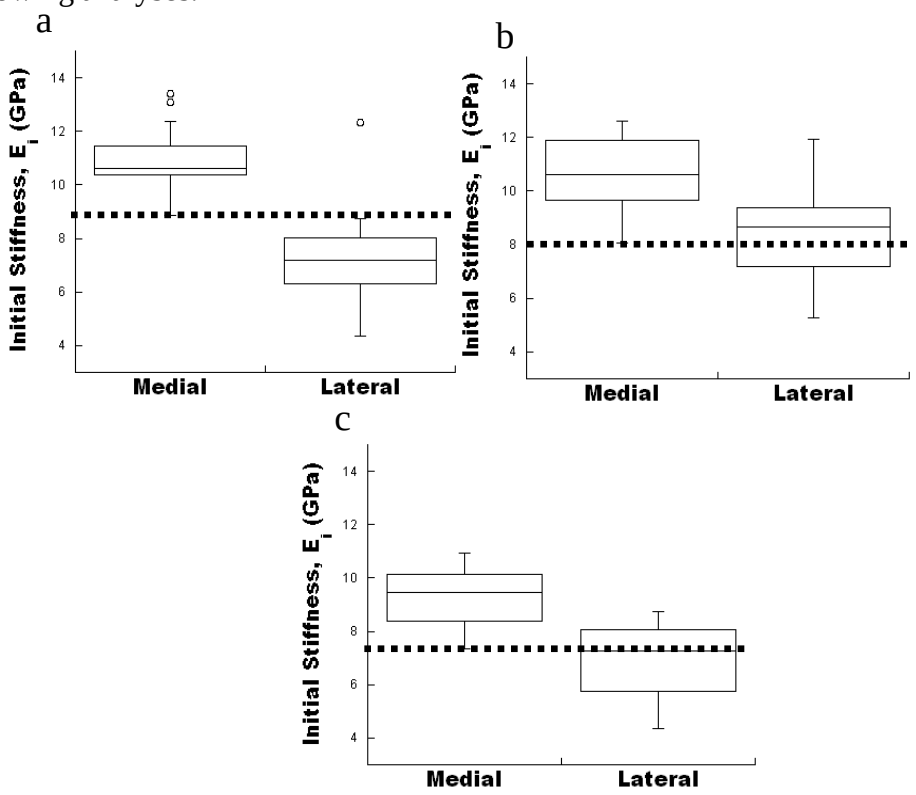

Figure 4.3 Comparison of initial stiffness in medial and lateral cortices. Box plots for (a) control ($p<0.0001$), (b) Aln 0.2 ($p<0.001$) and (c) Aln 1.0 ($p<0.0001$). Beams from the lateral cortex exhibited lower mean stiffness than beams from the medial cortex. Note the dashed line at the lower quartile of initial stiffness. Any lateral beams that exhibited initial stiffness values below this line were considered to be outliers.

4.2.1 Stiffness

Initial and final stiffness values from each group are summarized in Appendix E, along with loss in stiffness normalized by dividing stiffness differences (E_i-E_f) by initial stiffness (E_i). When compared to control, Aln exhibited a reduction in stiffness with Aln 1.0 exhibiting a significant difference in E_i vs. both control and Aln 0.2 ($P < 0.05$) (Figure 4.4). The average stiffness losses for control, Aln 0.2 and Aln 1.0 were 44 ± 15%, 51 ± 13%, and 54 ± 9%, respectively. Stiffness loss as a function of stress amplitude is plotted

in Figure 4.5. Stiffness loss exhibited a significant relationship with stress amplitude for the control group only.

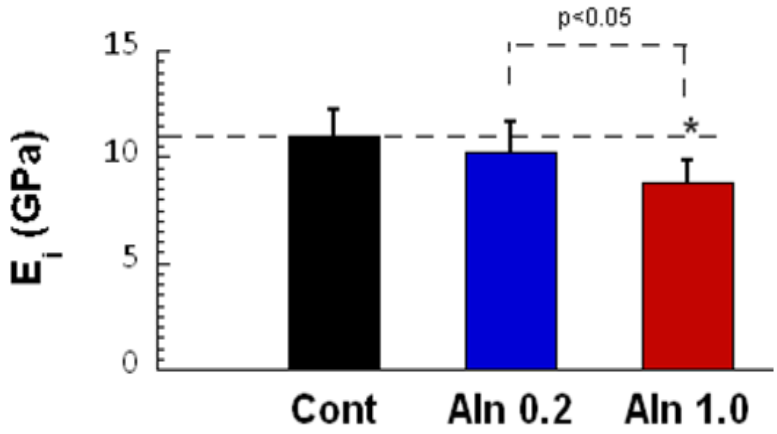

Figure 4.4 Comparison of initial stiffness for the three groups. * p<0.05 vs control unless specified.

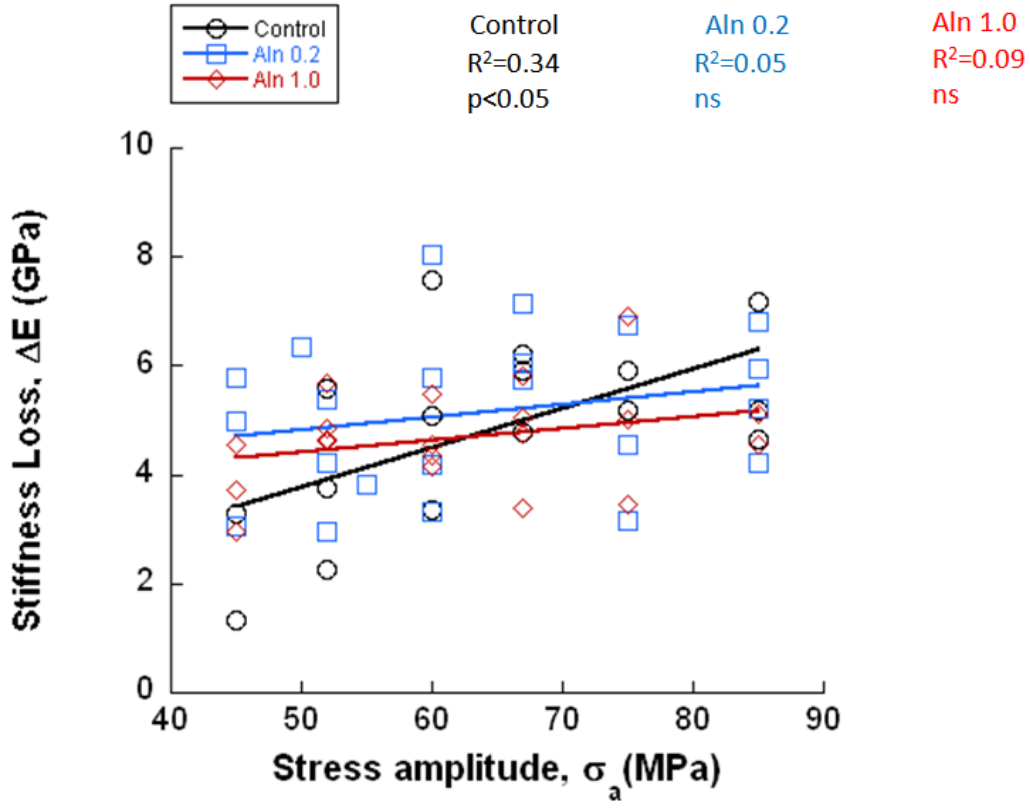

Figure 4.5 This figure demonstrates that changes in stiffness were not caused by changes in applied stress.

4.2.2 Fatigue-Life

Stress-life diagrams (S-N curves) for the three groups are shown in Figure 4.6. Note that each data point represents one beam specimen. Beams from the Aln 1.0 group required lower number of cycles to failure compared to beams from the control and Aln 0.2 groups. The power law fit to the pooled response of each group shows a dose-dependent reduction in fatigue-life of Aln treated cortical bone. Aln also had lower fatigue fracture strength (power law coefficient) with Aln 1.0 exhibiting the lowest strength (130 MPa) compared to Aln 0.2 (153 MPa) and control (164 MPa).

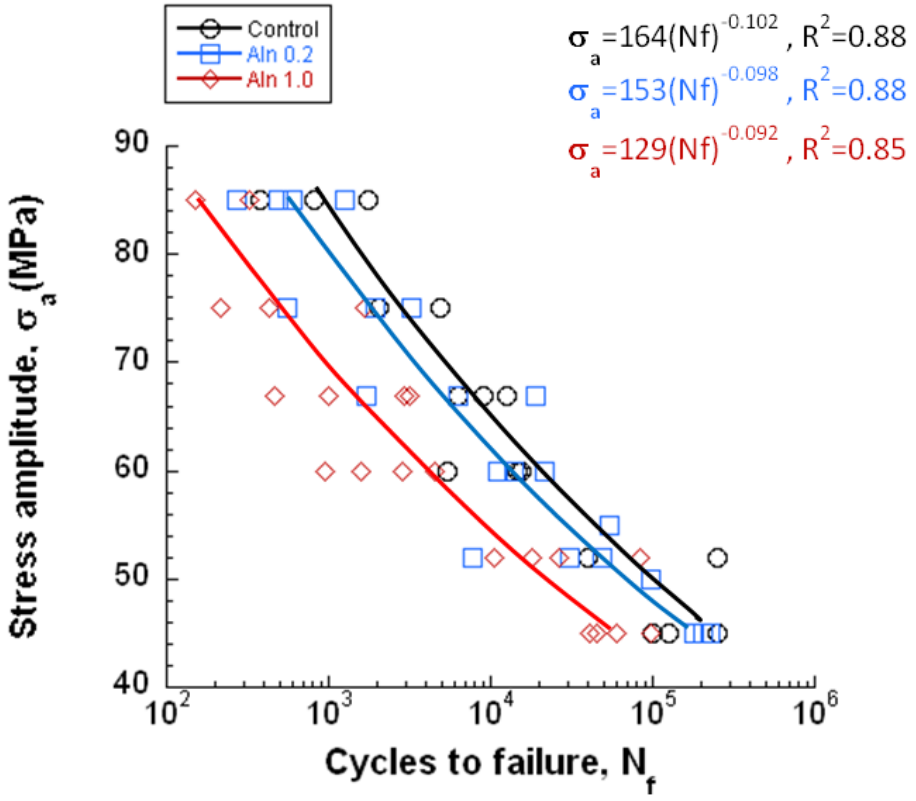

Figure 4.6 S-N curves for control and Aln treated bone.

Endurance strength (σ_e) represents the stress below which a material will show no evidence of failure when subjected to fatigue loading. σ_e for control, Aln 0.2 and Aln 1.0 were 45, 42 and 38 MPa, respectively.

Table 4.1 Calculated Average Cycles to Failure for Each Group.

σ_a	Cont	Aln 0.2	Aln 1.0
85	629	388	94
75	2149	1386	366
67	6506	4366	1243
60	19225	13410	4104
52	78364	57471	19322
45	324099	250040	92447

4.3 Structural Investigation

4.3.1 Histomorphometry

Any alterations in one area of the microstructure of bone tissue due to alendronate treatment might contribute to the decreased mechanical properties observed. For example, microdamage accumulation tends to be confined to the space between osteons, known as the interstitial or inter-osteonal area [45]. Total beam area is comprised mainly of osteonal and inter-osteonal areas, with resorptive area being a slight contributor. As summarized in Figure 4.7 alendronate treatment did not have a significant effect on total pore area, pore number or average pore size.

Since pore area normally occupies little (<3.5%) of the total beam area in the beams of cortical bone that were examined, an inverse relationship exists between osteonal and inter-osteonal areas. As a result differences seen in one tissue area are reflected in the other. A large difference was observed between Aln 1.0 treated and control bone microstructure, with Aln 1.0 exhibiting a 20% smaller osteonal area (Figure 4.8).

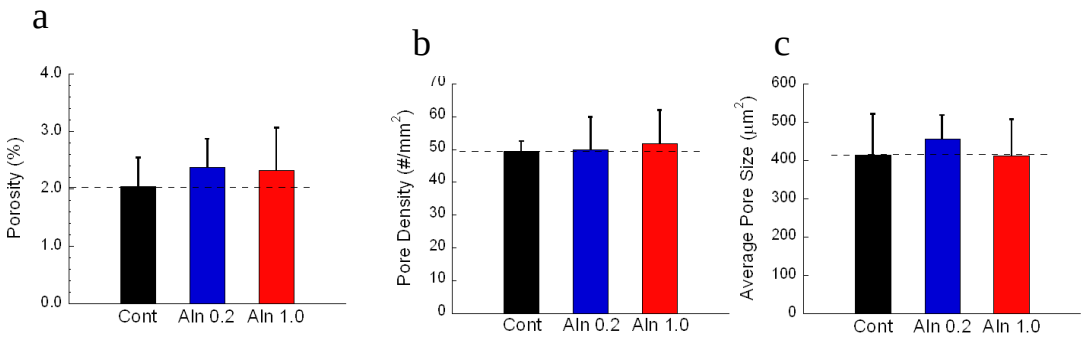

Figure 4.7 a) % Area of pores (normalized to beam cross-sectional area) for each group. b) The density or number of pores per mm^2. c) Average pore size (μm^2). No significant differences were found between groups.

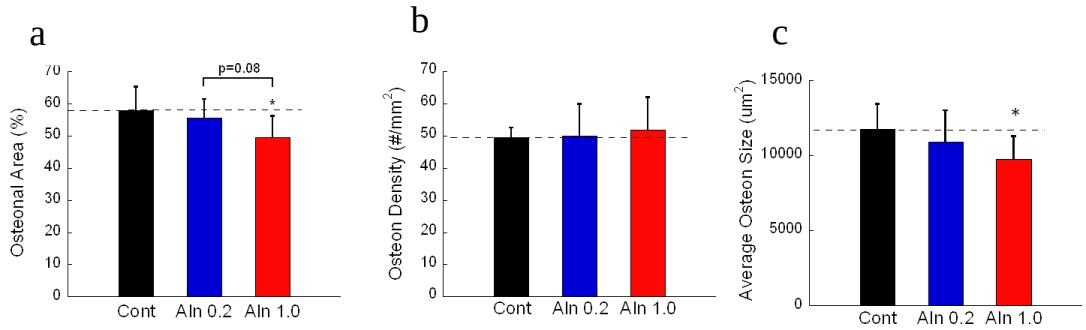

Figure 4.8 a) % Area of osteons (normalized to beam cross-sectional area) for each group. b) The density or number of osteons per mm^2. c) Average osteon size (μm^2). Significant differences exist between control and Aln 1.0 ($p<0.05$).

CHAPTER 5

DISCUSSION

"Cyclic fatigue tests of bone treated with BPs (bisphosphonates) have not been performed to determine whether the reduced toughness measured quasi-statically translates into reduced residual strength and shorter fatigue life of the bone under more physiologically relevant cyclic loading conditions. From a clinical standpoint, cyclic fatigue studies of BP treated bone are critical to interpreting fracture risk" --Allen and Burr 2011

This thesis represents the first study to investigate the implications of long-term bisphosphonate treatment on the fatigue-life of cortical bone. In collaboration with Drs. Matthew Allen and David Burr, 90 cortical bone beams with uniform geometry were cut from the ribs of 36 skeletally mature beagles divided into 3 treatment groups. The beams were cyclically loaded under 4-point bending, and evaluated for both mechanical and structural properties. Differences in these properties between the three groups suggest mechanisms behind the deterioration of tissue-level properties associated with long-term bisphosphonate use that would lead to a determination of reduced toughness of whole bone as Allen and Burr referred to in the above quote.

5.1 Mechanical Properties and Porosity

As introduced in Chapter 1, recent publications have suggested that a side-effect of long-term bisphosphonate use to treat low bone mass in patients may be a slight increased risk of low energy, atypical fractures of the femoral midshaft. Thus, many research investigations are underway to determine how bisphosphonate treatment alters bone quality and how dosing may alter these qualities.

If not properly removed, microdamage can provide a pathway for catastrophic crack propagation and material failure. This serves as an attractive mechanism to explain low energy fractures associated with long-term bisphosphonate use. Clinical studies have demonstrated that bone quality becomes altered with age in humans [45]. It is still unknown whether microdamage accumulation is affected in individuals taking bisphosphonates and whether or not microdamage accumulation is associated with atypical fractures [49].

5.2 Mechanical Properties and Structure

Results demonstrated that mechanical properties of cortical bone are altered after alendronate treatment. This was exhibited by reductions in initial stiffness and number of cycles to failure in alendronate-treated bone compared to control. Although an association between mechanical and structural properties has not been directly made, the results strongly suggest that bisphosphonate treatment changes the organization and composition of bone tissue and this can compromise mechanical integrity.

As reviewed in the first two chapters, a major indicator of bone's mechanical integrity is stiffness. The initial stiffness of high-dose, alendronate-treated bone was significantly lower than control bone (~15%). This suggests that tissue-level structural components that normally contribute to healthy bone quality are altered by alendronate treatment.

To further define alendronate's effects on mechanical and structural properties, stiffness loss was investigated as a function of stress amplitude. Control beams exhibited a linear relationship of stiffness loss with increasing stress amplitude, i.e. as expected

bone has greater stiffness loss at higher loads. Conversely, alendronate treated bone exhibited an extremely weak relationship between stiffness loss and stress amplitude. This occurred regardless of dose and indicates that long-term bisphosphonate treatment impairs bone quality. To investigate possible mechanisms behind these mechanical differences, structural properties of cortical bone were investigated.

In general, the composition and organization of structural components contribute to bone's strength and stiffness, or ability to withstand load. As introduced in Chapter 1, cortical bone tissue is populated with Haversian systems including canals and osteocyte lacunae; each structure performs a specific and vital function while also contributing to the overall porosity of cortical tissue. As reviewed in the first two chapters, bisphosphonate treatment could lead to increased tissue uniformity and reduced porosity. Therefore, these two characteristics may offer insight into the observed reduction in fatigue-related, material properties of bisphosphonate treated bone. Roschger *et al.* [2001] demonstrated a 46% reduced cortical porosity in alendronate-treated iliac crest bone from postmenopausal osteoporotic women compared to non-osteoporotic women. Additionally, they found that alendronate treatment increased mineralization uniformity. While this parameter was not explicitly investigated in this study, increased mineralization uniformity could be a consequence of reduced remodeling in conjunction with a prolonged secondary mineralization phase within older interstitial bone. The amount of this type of cortical bone was found increased in the alendronate-treated bone examined for this thesis.

Somewhat surprisingly, differences in porosity were not found; all groups exhibited similar porosity in line with normal porosity for rib bone of skeletally mature

female beagles. Porosity is largely determined by the number and size of Haversian canals. Neither was found to be affected. The contribution of lacunae was not directly investigated in this study. However, microCT measured BMD, which is largely affected by both Haversian canals and lacunae, was not found different between the 3 groups. The largest effect of alendronate treatment appeared to be on the compositional proportion of osteonal to interstitial cortical bone.

Combined, the results of this investigation suggest that tissue-level structural components normally contributing to healthy bone's stiffness are altered by alendronate treatment and contribute to reduced stiffness. These structural effects may also alter the way in which stiffness declines over time during cyclic loading. While numbers of osteons were not affected by treatment, the average size of each osteon was reduced, indicating that activation of remodeling BMUs was not affected by alendronate but the BMU size was made smaller. This is not unexpected given that bisphosphonate use has been shown to reduce the amount of bone resorbed by each osteoclast as was pointed out in Chapter 1. Another consequence of a smaller average osteon size was an increase in interstitial space. The interstitial area represents bone that is older when compared to osteonal bone. As interstitial area increases, the anisotropy of cortical bone is also reduced.

5.3 Fatigue-life

As pointed out in Chapter 1, an anisotropic material exhibits toughness due to an ability to resist crack initiation and extension. These toughening mechanisms improve a material's ability to withstand cyclic loading and depend on the capacity for energy

dissipation. The formation of microdamage, in the form of linear cracks and diffuse damage in bone serves as one mechanism by which energy is dissipated. In healthy bone, this damage is resorbed and replaced at a steady rate by remodeling. However, as bone ages, removal occurs at reduced rates. Furthermore, aged tissue demonstrates different microdamage accumulation patterns [45]. Older bone accumulates more linear microcracks compared to younger bone which accumulates more diffuse damage [45]. This suggests that as bone tissue ages, increased microdamage accumulates that may contribute to the progressive deterioration of bone quality and mechanical properties.

Previous studies completed with quasi-static loading of whole ribs from the same beagles examined for this thesis demonstrated a decreased toughness (~20%) after 1 year of high-dose alendronate treatment [33,51]. The study for this thesis represents the first fatigue evaluation of bisphosphonate-treated bone, and only the second time that bisphosphonate-treated bone tissue has been mechanically tested after machining beams of consistent geometry. Aln 1.0 treated bone required 5-fold or even fewer cycles to failure compared to the other groups. Taken together with an approximate 20% reduction in fatigue strength these results imply that high-dose alendronate treatment directly alters bone's ability to withstand cyclic loading, and could result in premature fracture.

Although this study did not include microdamage analysis, recent publications have investigated microdamage accumulation in canine ribs following 1 and 3 years of bisphosphonate treatment [47,33,51]. Mashiba *et al.* [2007] concluded that 1 year of high dose alendronate treatment resulted in significant damage accumulation five to seven fold greater than control. Similarities between that study and this investigation suggest that microdamage accumulation in alendronate treated bone may be associated with the

reduction in fatigue-life observed. However, studies conducted by Allen *et al.* [2008] demonstrate no significant difference in damage accumulation within beagle ribs between 1 and 3 years of alendronate treatment. Because there was a significant 20% reduction in toughness for 3-year treated whole ribs only, the authors concluded that the reduction in mechanical properties of alendronate-treated bone was not significantly attributed to damage accumulation. This current study was not designed to examine differences in treatment duration or damage accumulation and therefore, the contribution of treatment duration or damage levels on cycles to failure observed in alendronate-treated bone are only be speculative.

During healthy remodeling of cortical tissue, old or damaged osteons are replaced with new osteons of similar shape and size, maintaining the overall osteonal area (Figure 5.1). The conservation of osteon size not only maintains the amount of interosteonal area where damage can accumulate, but also ensures that osteons remain in close proximity to one another providing structural reinforcement.

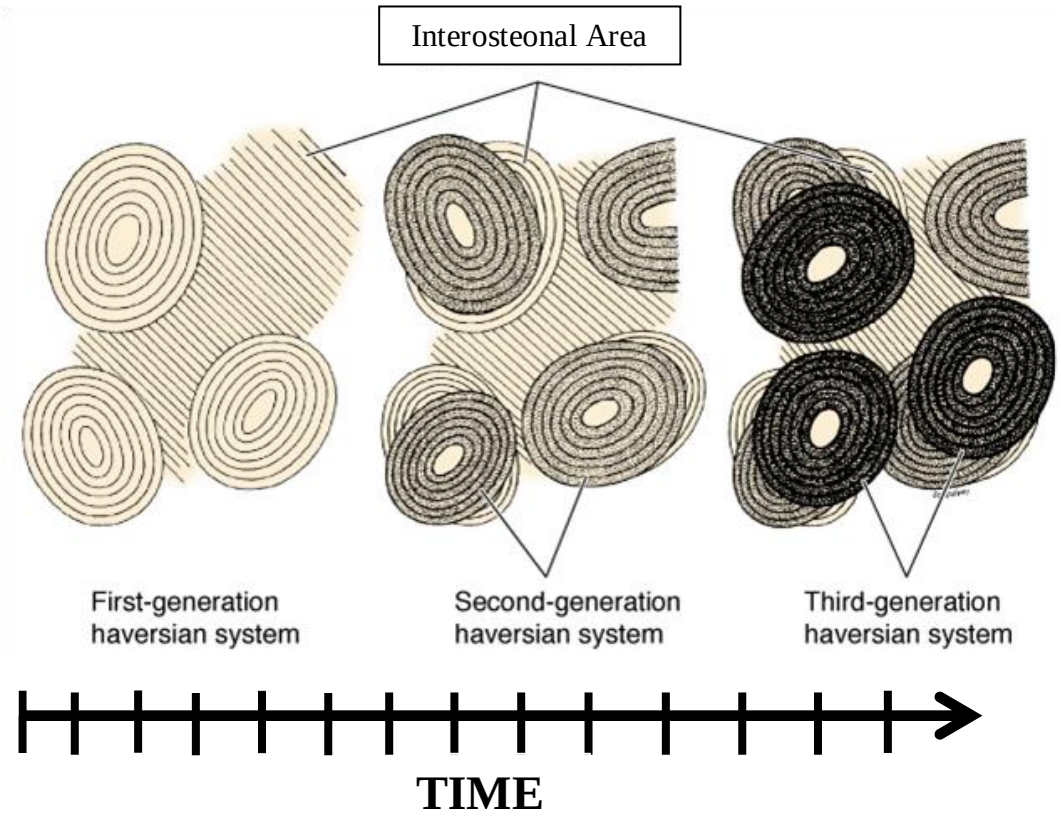

Figure 5.1 Healthy cortical remodeling results in the production of Haversian canals (osteons) similar in shape and size across generations [2].

However, this study has demonstrated that high dose alendronate treatment results in a 17% reduction in osteonal area, while conserving the total number of osteons. This indicates that with high dose alendronate treatment, the overall size of individual osteons is significantly decreased in cortical tissue as a function of time (Figure 5.2). This reduction in osteon size has two implications: 1) lack of osteon reinforcement, and 2) an increase in the space between osteons (i.e. interosteonal area). Due to the shrinking of osteons over time, these structures can no longer reinforce one another as observed in healthy remodeling. Additionally, an increase in interosteonal area suggests that there is more area for damage to accumulate between osteons (Figure 5.3). Previous research has demonstrated a five to seven fold increase in damage accumulation within cortical bone

treated with high dose alendronate [51]. Therefore, it can be suggested that an increase in interosteonal area may lead to in an increase in damage accumulation, resulting in the reduction of tissue-level mechanical properties of cortical bone.

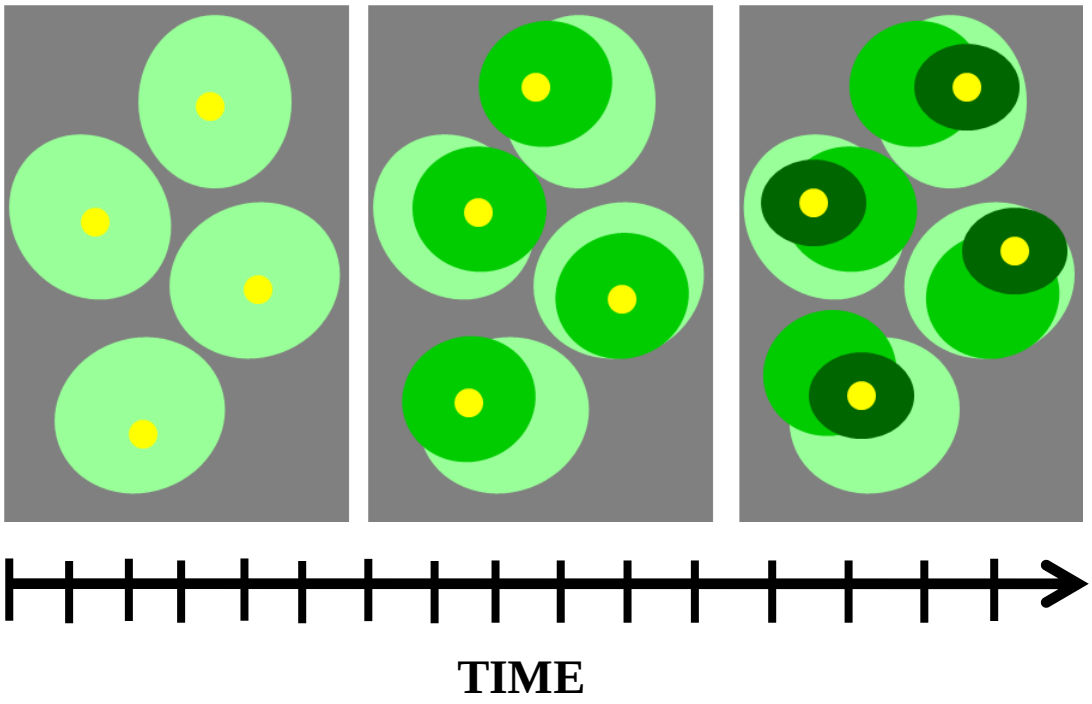

Figure 5.2 The gradual reduction in osteon size over time is illustrated here. Yellow dots represent Haversian pores.

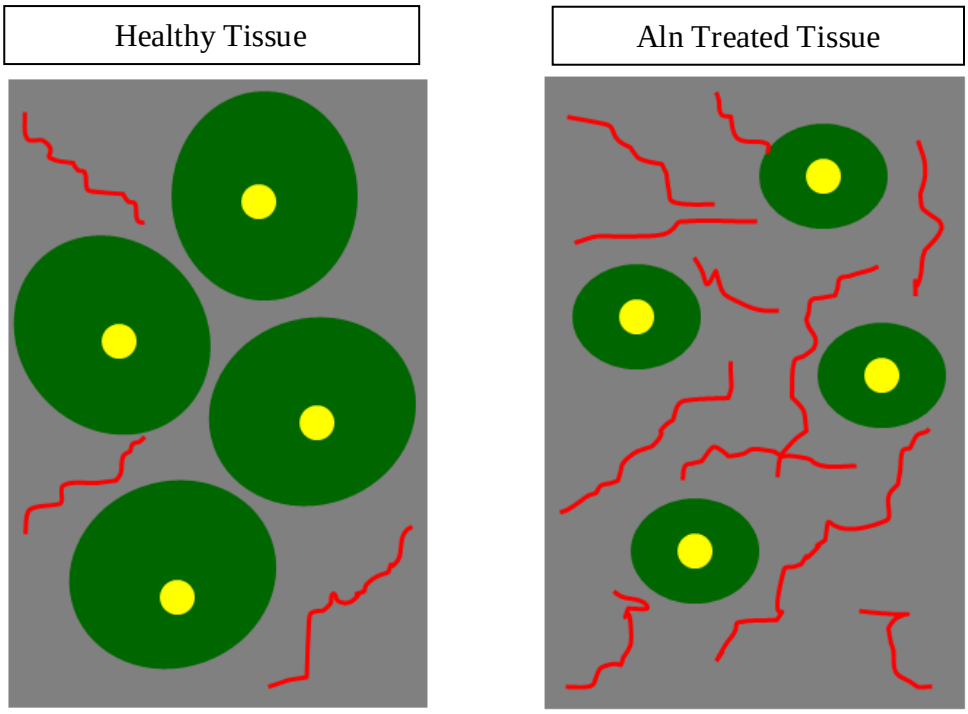

Figure 5.3 This cartoon illustrates the increase in interosteonal area observed in long-term alendronate treated tissue, which suggests an increase in area for damage to accumulate when compared to healthy tissue.

5.4 Limitations

Limitations to this investigation exist in both the animal model, and preparation and testing of bone tissues from the animal model utilized. Ideally, the effects of drugs on human tissues are best studied in tissues from patients and appropriate controls. However, such a controlled study as conducted for this thesis would not be possible in a patient population where taking biopsy specimens large enough for mechanical testing is painful and collecting a large enough sample size is not feasible in a 2-year study time frame. Canine bone tissue exhibits remodeling similarities to that in human bone that allow for its use in determining the effects of drugs on bone tissue. Many other animals, including rodents, do not exhibit bone remodeling and could not serve as models for human bone conditions.

Limitations concerning the beagle dog model are described in detail elsewhere [90]. In summary, canines were not estrogen-deficient and did not exhibit low bone mass prior to treatment. The goal of this study was to investigate the effects of alendronate treatment on normally remodeling bone. Now that this thesis has determined the fatigue effects of alendronate on normal bone further work should investigate these effects in osteoporotic conditions which normally warrant bisphosphonate treatment.

This study was limited to one duration of alendronate treatment. Three years of treatment in this model is considered to be long-term, equivalent to at least 5 years of use in humans due to the higher metabolism of dogs. While likely that the duration of treatment would affect outcomes, conclusions regarding the duration of treatment cannot be made. For example, whether the one year of treatment that has been associated with an increased accumulation of microdamage in the beagle rib would show similar fatigue loading effects to the 3-year results found in the current study is unknown. The dose of alendronate administered was found to affect fatigue life and other mechanical properties differently; the effects on initial strength, and fatigue life and strength appeared to be proportional to dose administered. The high dose administered in this study was chosen to be equivalent to that given clinically for Paget's disease as reviewed in Chapter 1. The low dose was chosen to be equivalent to that given for treating osteoporosis.

A final limitation of this study regarding the model was that only one bone from the beagle was examined. The choice of rib bone versus another load-bearing bone was made to capture any effects of alendronate on remodeling. Canine ribs (and those in humans) undergo significant remodeling compared to other bones due to the relatively high frequency of loading associated with breathing. However, further investigations of

the mechanisms behind cyclic loading and atypical fractures should take into account differences that exist in cortical bone at different anatomical locations.

No previous studies have investigated the fatigue-life or tissue-level properties of bisphosphonate-treated rib bone. Several limitations regarding the preparation and testing of bone tissues were confronted in this investigation, some foreseen and some not. Rib cortices were thin enough to present significant machining challenges. Each individual rib was visually surveyed to identify thicker cortical regions for both primary and secondary cuts. However, human error occurred during cutting and three ribs produced no purely cortical beams. This difficulty in machining beams was foreseen and whole-rib microCT data was collected prior to beam fabrication in an attempt to identify thicker regions of bone to target for beam excision. In theory, this prior mapping should aid the machining process and further work should be devoted to improving the yield of bone beams from thin cortices.

Other limitations pertained to the mechanical loading setup. The longest fatigue loading on beams tested under low stress amplitudes sometimes resulted in beams becoming wedged between the lower loading pins. Investigation of these beams determined that the edges of the loading pins began to chew away material as the beam reached higher cycles of loading. In these cases, the initial decrease in elastic modulus was followed by an unexpected increase in modulus. To avoid this possibly confounding interpretation, the experiment was designed to allow beams a maximum of 250,000 loading cycles. Establishing such a cycle limit has been used in previous fatigue-loading studies. It is unlikely that this limit significantly affected the determination of fatigue life relationships.

5.5 Major Results

Direct links between long-term bisphosphonate use and atypical fracture are difficult to establish. This study does suggest that bisphosphonate induced remodeling suppression directly alters tissue-level cortical properties and can compromise the overall integrity of canine rib bone tissue subjected to fatigue loading.

Bisphosphonate treatment was found to significantly decrease the initial stiffness of cortical bone beams compared to controls. Additionally, the relationship of stiffness loss with the amplitude of loading observed in control beams was not observed in alendronate-treated bone, suggesting a smaller dependence on energy to fracture in treated versus healthy canine cortical bone tissue.

Of greatest importance, this investigation examined the effects of cyclic loading on bisphosphonate-treated cortical bone for the first time and found significant effects on reducing fatigue life by > 3-fold or greater. While others have reported mechanical properties of bisphosphonate treated bone using quasi-static and whole bone testing to demonstrate a global assessment of bone, this study has utilized methods of testing at the bone-tissue level.

5.6 Further Work

Considering that bisphosphonates suppress remodeling and that microdamage is generally confined to older, highly mineralized regions of bone tissue, a plausible explanation for the observed reduction in cycles to failure exhibited by alendronate-treated bone may be due to excessive damage accumulation. In principle, cracks would propagate more easily through a material with voids or damage compared to a solid.

Therefore, it can be suggested that extensive damage accumulation from suppressed remodeling would require fewer cycles to failure. Quantifying damage within the unloaded portions of the beams would constitute an important addition to the study for this thesis.

Although fatigue analysis of bone simulates real world conditions of cyclic bone loading, quasi-static and creep testing also provide mechanical information vital to the overall assessment of bone tissue. To further develop and strengthen this investigation, creep loading of bone beams excised from ribs of the same animals should be conducted. This would provide an even more comprehensive analysis of the mechanical properties affected by alendronate treatment. Eventually, such studies as this one will bring to full light the mechanisms behind the affects that reduced remodeling has on bone tissue quality and lead to improved long-term treatment for osteoporosis and other bone disease.

CHAPTER 6

CONCLUSIONS

As the first study to investigate changes in tissue-level fatigue-life of bisphosphonate treated cortical bone, results from this study offer insight into the possible link between long-term treatment and atypical fractures of the femur. While this investigation showed that high and low dose alendronate successfully maintained cortical tissue mineral density, results also demonstrate that alendronate treatments reduce the tissue-level mechanical properties of cortical bone under fatigue loading. High dose alendronate treated cortical bone exhibited a significant 21% reduction in initial stiffness when compared to control. High dose alendronate treatment also resulted in a 5-fold reduction in the number of cycles to failure, indicating that high dose alendronate treated bone will fracture with 5 times fewer cycles when compared to control. Additionally, the high dose alendronate treatment exhibited a significant reduction in osteonal area (-17%). This 17% reduction in osteonal area indicates a 17% increase of interosteonal area.

This study has demonstrated that long-term treatment of alendronate does alter cortical bone micro-structure. As a result of altered micro-structure, the overall mechanical integrity of alendronate treated cortical bone becomes compromised resulting in the reduction of mechanical properties, specifically the significant reduction in the amount of cycles required to fracture cortical bone beams. This reduction in cycles to failure offers a possible mechanism by which low energy, atypical fractures may be associated with long-term bisphosphonate treatment.

APPENDIX A

BASIC FUCHSIN STAINING PROTOCOL

Basic stain for calcified bone specimens

ALL STEPS OF PROTOCOL ARE TO BE CONDUCTED IN OR NEAR SINK
****Gloves, safety goggles, and lab coat or apron for all steps of protocol****

Basic Fuchsin (Pararosaniline Chloride) 99%, pure---Acros Organics
C.I.: #42500 CAS: 569-61-9 Molecular weight 323.83

:::CAUTION:::

This stain is toxic and is a suspected carcinogen. **ALWAYS** wear gloves, safety goggles, and lab coat or apron while working with this stain. Avoid contact with skin. All work should be done in or near a sink.

Solutions:

1% BASIC FUCHSIN STOCK

Basic Fuchsin Powder	1.0 gram
100% Ethanol	100.0 ml

Let 1% stock solution mix for 48 hours prior to dilution

80% BASIC FUCHSIN

1% Basic Fuchsin Stock	8.0 ml
Distilled Water	2.0 ml

90% BASIC FUCHSIN

1% Basic Fuchsin Stock	9.0 ml
Distilled Water	1.0 ml

100% BASIC FUCHSIN

1% Basic Fuchsin Stock	10.0 ml

Procedure:	Duration
1) 80% Basic Fuchsin	48 hours on magnetic stir plate
2) 90% Basic Fuchsin	48 hours on magnetic stir plate
3) 100% Basic Fuchsin	48 hours on magnetic stir plate

*****Continue with embedding protocol for ETOH washing, Xylene clearing, and PMMA infiltration*****

APPENDIX B

EMBEDDING PROTOCOL

Polymethyl methacrylate embedding for calcified bone specimens

****To be conducted after Basic Fuchsin staining protocol****
ALL STEPS OF PROTOCOL ARE TO BE CONDUCTED UNDER HOOD
Gloves, safety goggles, and lab coat or apron for each step in protocol
Xylene CAS: 1330-20-7
PMMA CAS: 9011-14-7

Procedure:	Duration
1) ETOH WASH	
Fresh 100% ETOH	10 minutes
Fresh 100% ETOH	1 hours (additional washings if excess dye)
2) CLEARING	
Xylene I	3 hours on shaker
Xylene II	24 hours on shaker (overnight)
Xylene III	3 hours on shaker
3) INFILTRATION	
Hard PMMA I	24 hours on shaker (room temperature overnight)
Hard PMMA II	24 hours (refrigerator overnight)
Hard PMMA III	24 hours (refrigerator overnight)

After successful infiltration, bone specimens are placed into a small jar with a thin layer of hardened PMMA. Additional liquid PMMA III is added to submerge the specimen, and left to settle for 2-3 days. Jars can then be placed in a hotroom (~40ºC) until completely hardened. To free hardened PMMA with embedded sample, place jar in thick plastic bag and hit with hammer until glass jar breaks. Carefully pour glass shards into glass receptacle and remove plastic block. Rinse block with water to remove small glass pieces. Gently grind both surfaces to remove any remaining glass and make surfaces parallel.

PMMA II contains:	100 ml PMMA I and 1 gram Benzoyl Peroxide
PMMA III contains:	100 ml PMMA I and 2.5 grams Benzoyl Peroxide

*****Continue with slicing protocol*****

APPENDIX C

SECTIONING PROTOCOL

Block sectioning of embedded calcified bone specimen

****To be conducted after PMMA embedding protocol****
PRIOR TO CONDUCTING THIS PROTOCOL, review Buhler Isomet 500 Precision Saw hand book for detailed operating instructions

Note: Vice mounting on micrometer can be moved along the x-axis. Left and right directional buttons located on the front display allow for –X and +X movement, respectively. Blade mounting can be moved along the y-axis. Up and down directional buttons located on the front display allow for –Y and +Y movement, respectively. Additionally, hand crank locate on the front panel allows for more efficient movement along the y-axis.

Block Specimen Preparation:

1. Label the wall of each block with the bone beam number_letter with a Shapry.
2. To track the upper left corner of all sections to be cut, color half of the top face of the block with a Sharpy parallel to the length of the bone beam.
3. Using a caliper, measure the thickness of the block and write this value on the block using a Sharpy.
4. Using glue, fix the block to a plastic slide.
5. Next, fix the plastic slide/block assembly to an aluminum plate using glue and mount the plate in the vice within the saw.

Precision Sectioning Protocol: **Review user hand book before operating saw**

1. Turn on Buheler Isomet linear precision saw.
2. Hard home the system.
    i. Using the hand crack on the front of the slicer, slowly glide the blade (to the right) towards the back of the unit until the display reads "WARNING ARM LIMIT"
    ii. Then, glide the blade (to the left) towards the front, stopping just as the warning disappears.
3. Using the hand crank, slowly glide the blade along the y-axis towards the specimen. Rotate crank left.
4. Using the left and/or right directional buttons, advance the specimen along the x-axis to aligning the blade with the location of the initial cut.

5. Once the blade is properly aligned, slowly glide the blade close to the face of the block and note the distance. Rotate crank left.
6. Glide blade 4 mm away from the block. Rotate crank right.
7. Zero the system by pushing the zero button. The distance remaining should then read 0 mm.
8. Input the desired cutting parameters
    i. Blade Speed
    ii. Feed Rate
    iii. Cutting Length
    iv. Sample thickness
    v. Specimen Quantity
    vi. Blade Thickness

9. Ensure cutting liquid is directed over specimen.
10. Recheck cutting parameters, as well as specimen alignment.
11. To begin sectioning, push Start Cycle.
12. To pause sectioning, wait until blade has returned to its point of origin and the micrometer has advanced the specimen, then push Pause Cut. To restart, put Start Cycle.
13. Once the entire specimen is sectioned, remove the aluminum plate from the saw.
14. Remove the block from the plastic slide and rinse the block with water and dry.

*****Continue with mounting protocol for disassembling of block and mounting of sections onto slides*****

APPENDIX D

MOUNTING PROTOCOL

Section mounting for calcified bone specimens

****To be conducted after PMMA embedding protocol****
PROTOCOL MUST BE CONDUCTED UNDER VENTILATION

Acetonitrile:: CAS Number: 75-05-8
Chemical Formula: CH_3CN
Molecular Weight: 41.05 g mol^{-1}

Caution: Acetonitrile is flammable and can cause irritation to the eyes. One should be in a well-ventilated area when handling acetonitrile.

Specimen Preparation

1. To prepare the specimen for mounting, first remove each section one by one from the block. Place the same face down with each section.
2. Dry each section and number each section using a pen or marker.
3. Using a scissor, remove the upper left corner of each section.
4. Using grinding papers under water irrigation grind the bottom surface of each section.
5. Next, use a polishing wheel and decreasing alumina diameter slurries to polish each section to a mirror finish.
6. Finally, to remove microscopic debris, place the sections in a beaker containing deionized water into a sonicating water bath for about two minutes.
7. Dry off sections and prepare them for mounting.

Specimen Mounting

1. Set Up
    a. Small beaker with 100% ETOH with dropper.
    b. Dropper filled with Acetonitrile. **TO BE USED UNDER GOOD VENTILATION.**
    c. To prepare the plastic slides, remove the paper covering from one side and write the beam number_letter and slice number on opposite side. Prepare a slide for each sample.

2. Section Mounting
    a. Using forceps and a dropper, clean the exposed surface of slides pertaining to one beam using 100% ETOH.
    b. Allow all slides to be completely dry before advancing to the next setp.
    c. Using forceps and a dropper, clean both surfaces of one segment with 100% ETOH.
    d. Next, apply one to two drops of acetonitrile to the sterile surface of the slide.
    e. Apply the sterile cross section to the slide utilizing capillary forces by drawing the acetonitrile across the section, reducing the formation of bubbles.
    f. Immediately, apply pressure across the cross section.
        --Apply the thumb roll for 15 sections. Also can use a water filled tube as a rolling pin to evenly apply pressure across the section.
    g. Next, apply perpendicular pressure with thumb for 30 sections.
    h. Once all sections from one beam have been mounted, stack slides on top of one another, placing a piece of parafilm between the samples.
    i. Apply a clamp and allow adequate time for plastics to properly fuse.
    j. Repeat these steps with remaining beam section.

3. Thickness Reduction :: 300 microns to ~100 microns
    a. Once section and slide are fused, measure the thickness of the slide using a caliper and write this value on the back of the slide.
    b. Using 600 grit grinding paper under water irrigation, reduce the thickness of the cross section. Monitor progress by measuring the thickness of the specimen and slide periodically.
    c. Once target specimen thickness is achieved, polish section using decreasing alumina diameter slurries until mirror finish.
    d. Place slides in sonicating water bath for two minutes to remove microscopic debris.

4. Labeling
    a. Wipe both surfaces with a kim wipe to remove any surface debris.
    b. Write the beam number_letter and slice number on white labels and apply them to the slides.
    c. Place slides in slide box.

APPENDIX E

DATA FOR ALL THREE GROUPS

The following tables contain the data from this investigation for all three groups. Yellow boxes indicate beams which came from the medial position and green boxes indicate beams that came from the lateral position.

Table E1. Control Data

Beam Number	Stress (MPa)	N_f (Cycles)	Secant E_i (GPa)	Secant E_f (GPa)	Secant Loss (GPa)	Secant Loss (%)
59315_B	45	125000	10.77	9.44	1.33	12.34
59234_A	45	100000	9.42	6.13	3.29	34.96
60644_B	45	250000	11.09			
59315_D	52	250000	11.54	7.79	3.75	32.48
60667_A	52	250000	13.39	11.12	2.27	16.93
60628_F	52	40000	12.34	6.76	5.58	45.24
60632_B	60	15319	10.60	3.03	7.57	71.43
59234_C	60	5405	8.87	5.52	3.35	37.82
59677_C	60	14731	10.34	5.25	5.09	49.25
60632_D	67	12564	10.39	5.59	4.80	46.22
60628_D	67	6260	10.40	4.48	5.91	56.88
60707_B	67	9067	12.39	6.16	6.22	50.24
60632_F	75	4916	11.28	6.08	5.20	46.07
59257_D	75	2053	11.33	5.40	5.93	52.31
60628_B	85	382	9.65	4.99	4.66	48.29
60644_H	85	806	10.43	5.25	5.18	49.64
60628_E	85	1756	13.09	5.89	7.19	54.95
Average			11.02	6.18	4.83	44.07
STDEV			1.24	1.92	1.69	14.66

Table E2. Aln 0.2 Data

Beam Number	Stress (MPa)	N_f (Cycles)	Secant E_i (GPa)	Secant E_f (GPa)	Secant Loss (GPa)	Secant Loss (%)
60636_F	45	226880	10.62	4.84	5.77	54.38
59256_F	45	205000	10.01	6.95	3.06	30.58
59258_E	45	180000	11.21	6.23	4.98	44.43
60636_A	50	97986	11.26	4.91	6.34	56.35
60592_B	52	31000	9.47	5.25	4.22	44.59
60592_F	52	7705	8.05	5.09	2.96	36.77
60636_E	52	49173	10.08	4.70	5.38	53.36
59258_D	55	53804	10.45	6.64	3.81	36.43
59258_B	60	11000	11.90	3.87	8.03	67.48
60592_D	60	21825	11.10	5.33	5.77	52.00
60636_C	60	13936	9.91	5.72	4.19	42.30
60631_G	60	600	8.77	5.43	3.34	38.08
60631_D	67	19000	12.62	6.88	5.74	45.49
60631_H	67	6250	12.28	5.13	7.15	58.24
59256_A	67	1696	8.68	2.62	6.06	69.81
59256_G	67	3561	8.89	2.42	6.47	72.79
59219_F	75	3282	10.75	6.20	4.55	42.31
60631_F	75	1956	12.38	5.64	6.75	54.50
59256_C	75	550	8.84	5.68	3.16	35.75
59219_B	85	485	8.68	4.47	4.21	48.54
60631_B	85	604	9.64	2.84	6.80	70.51
60642_E	85	1250	11.93	6.71	5.22	43.74
60631_E	85	273	8.68	2.74	5.94	68.40
Average			10.27	5.06	5.21	50.73
STDEV			1.39	1.37	1.42	12.52

Table E.3 Aln 1.0 Data

Beam Number	Stress (MPa)	N_f (Cycles)	Secant E_i (GPa)	Secant E_f (GPa)	Secant Loss (GPa)	Secant Loss (%)
59211_D	45	60000	10.58	10.58	-	-
60641_C	45	45000	7.91	4.94	2.97	37.51
60593_A	45	98689	7.57	3.03	4.55	60.06
59238_A	45	40555	8.35	4.64	3.71	44.44
59231_A	52	18204	8.88	4.03	4.86	54.68
60641_B	52	26135	10.07	4.40	5.67	56.33
59238_B	52	84406	10.93	6.30	4.63	42.37
60750_E	52	10500	8.74	4.08	4.65	53.25
59231_D	60	4550	10.20	5.85	4.35	42.64
59236_D	60	953	8.58	4.03	4.55	53.04
59211_A	60	1591	8.21	2.74	5.47	66.63
60809_A	60	2881	7.76	3.60	4.16	53.64
59231_C	67	2930	9.57	4.53	5.04	52.70
59211_B	67	3206	9.38	4.62	4.76	50.75
60643_A	67	466	8.22	2.42	5.80	70.58
60657_D	67	1007	7.35	3.97	3.38	45.99
60750_D	75	218	7.33	3.86	3.47	47.31
60643_C	75	425	8.55	3.53	5.02	58.71
60643_D	75	1662	10.10	3.19	6.92	68.46
60593_B	85	321	7.57	3.03	4.55	60.06
59231_E	85	152	8.06	2.92	5.13	63.71
Average			8.76	4.30	4.68	54.14
STDEV			1.11	1.74	0.91	9.15

APPENDIX F

OUTLIER DATA FOR ALL THREE GROUPS

The following tables contain the data of outlier beams from this investigation for all three groups. Yellow boxes indicate beams which came from the medial position and green boxes indicate beams which came from the lateral position.

Table F1. Control Data

Beam Number	Stress (MPa)	N_f (Cycles)	Secant E_i (GPa)	Secant E_f (GPa)	Secant Loss (GPa)	Secant Loss (%)
59210_A	45	35000	8.73	5.33	3.40	38.90
60628_A	52	14000	7.89	4.72	3.18	40.22
59315_C	52	3000	6.43	4.86	1.57	24.41
60634_A	52	1000	8.14	5.23	2.91	35.74
60644_A	60	298	6.70	2.30	4.39	65.60
60632_E	60	5000	9.91	4.69	5.22	52.68
59315_A	67	70	6.16	4.42	1.74	28.21
59234_B	67	28	4.35	3.63	0.71	16.44
60632_A	75	1200	7.62	2.97	4.65	61.05
60628_C	75	56	6.19	4.00	2.19	35.39
60632_C	85	414	7.54	2.92	4.62	61.24
59677_D	85	60	6.80	3.78	3.02	44.38
Average			7.21	4.07	3.13	42.02
STDEV			1.43	0.97	1.41	15.54

Table F2. Aln 0.2 Data

Beam Number	Stress (MPa)	N_f (Cycles)	Secant E_i (GPa)	Secant E_f (GPa)	Secant Loss (GPa)	Secant Loss (%)
60631_C	45	740	6.59	4.88	1.71	25.90
59256_E	45	20000	7.36	3.50	3.86	52.46
60642_A	52	250	6.70	4.11	2.59	38.62
60592_E	52	3000	7.93	4.47	3.46	43.59
59258_C	55	19052	7.40	3.91	3.48	47.08
59219_C	67	204	6.90	2.80	4.09	59.34
60592_A	67	95	6.99	2.65	4.34	62.12
60642_F	75	57	5.28	3.65	1.62	30.72
59219_A	75	600	7.84	4.60	3.24	41.31
Average			7.00	3.84	3.15	44.57
STDEV			0.80	0.77	0.98	12.15

Table F3. Aln 1.0 Data

Beam Number	Stress (MPa)	N_f (Cycles)	Secant E_i (GPa)	Secant E_f (GPa)	Secant Loss (GPa)	Secant Loss (%)
60657_C	45	2000	6.32	4.58	1.75	27.59
60750_G	52	5000	7.10	4.67	2.43	34.19
59236_B	60	463	6.61	3.65	2.96	44.75
59236_C	75	349	5.76	4.19	1.57	27.28
59231_B	75	81	5.67	4.00	1.68	29.53
59211_C	75	86	5.56	2.76	2.80	50.41
59236_A	85	258	5.35	-	-	-
60641_D	85	39	5.69	3.80	1.88	33.10
59211_E	85	29	4.36	3.62	0.75	17.12
60643_E	85	256	7.21	2.57	4.64	64.33
Average			5.96	3.76	2.27	36.48
STDEV			0.86	0.72	1.12	14.32

APPENDIX G

STIFFNESS DATA BY LOCATION

The following tables contain stiffness data from both medial (med) and lateral (lat) positions. Yellow boxes indicate beams which came from the medial position and green boxes indicate beams which came from the lateral position

Table G1. Control Data

Stress Amplitude	Secant E_i (GPa)		Secant E_f (GPa)		Secant Loss (GPa)		Secant Loss (%)	
	Lat	Med	Lat	Med	Lat	Med	Lat	Med
45	8.73	10.09	5.33	7.78	3.40	2.31	38.90	23.65
52	8.70	12.46	5.39	9.45	3.31	3.01	36.40	24.70
60	8.30	9.94	3.50	4.60	4.81	5.34	59.14	52.83
67	5.25	11.06	4.03	5.41	1.23	5.65	22.33	51.11
75	6.91	11.30	3.49	5.74	3.42	5.56	48.22	49.19
85	7.17	11.06	3.35	5.38	3.82	5.68	52.81	50.96
Average	7.51	10.99	4.18	6.39	3.33	4.59	42.97	42.08
STDEV	1.35	0.91	0.94	1.84	1.17	1.52	13.20	13.92

Table G2. Aln 0.2 Data

Stress Amplitude	Secant E_i (GPa)		Secant E_f (GPa)		Secant Loss (GPa)		Secant Loss (%)	
	Lat	Med	Lat	Med	Lat	Med	Lat	Med
45	8.80	10.32	4.87	5.90	5.14	5.90	40.93	42.48
50	11.26	-	4.91	-	6.34	-	56.35	-
52	8.24	8.76	4.43	5.17	3.81	5.17	45.19	40.68
55	7.40	10.45	3.91	6.64	3.48	6.64	47.08	63.57
60	9.34	11.50	5.57	4.60	3.76	4.60	40.19	59.74
67	7.86	12.45	2.62	6.00	5.24	6.00	66.02	51.87
75	7.32	11.57	4.65	5.92	2.67	5.92	35.93	48.40
85	10.30	9.16	4.73	3.66	5.58	3.66	56.07	59.52
Average	8.81	10.60	4.46	5.41	4.50	5.59	48.47	52.32
STDEV	1.41	1.34	0.88	1.01	1.25	1.22	10.16	8.96

Table G.3 Aln 1.0 Data

Stress Amplitude	Secant E_i (GPa)		Secant E_f (GPa)		Secant Loss (GPa)		Secant Loss (%)	
	Lat	Med	Lat	Med	Lat	Med	Lat	Med
45	7.54	-	4.30	-	3.24	-	42.40	-
52	7.92	9.96	4.38	4.91	3.54	5.05	43.72	51.13
60	7.53	9.39	3.33	4.94	4.20	4.45	55.01	47.84
67	6.39	9.06	3.62	3.86	2.77	5.20	41.48	58.01
75	6.13	8.71	3.23	3.52	3.10	5.19	44.56	57.88
85	7.54	7.57	4.30	3.03	3.24	4.55	42.40	60.06
Average	7.10	8.94	3.77	4.05	3.37	4.89	45.44	54.98
STDEV	0.79	0.89	0.54	0.85	0.54	0.36	5.48	5.23

APPENDIX H

POROSITY DATA

The following tables contain the porosity data using in this investigation.

Table H1. Control Data

Beam Number	Beam Area (mm^2)	Total Porosity (mm^2)	Porosity (%)	Number of Pores (#)	Average Pore Size (mm^2)	Pore Density (#/mm^2)
60632_D	0.65	0.010	1.59	33.67	0.00031	51.67
60628_B	0.61	0.013	2.14	32.00	0.00041	52.05
60628_D	0.70	0.016	2.27	33.33	0.00048	47.51
59315_B	0.73	0.013	1.75	34.00	0.00038	46.39
59234_A	0.57	0.017	2.94	27.50	0.00061	48.01
59234_C	0.51	0.006	1.18	24.00	0.00025	47.01
59315_D	0.75	0.015	2.03	37.33	0.00041	49.72
60667_A	0.63	0.013	2.10	35.20	0.00038	55.47
60628_F	0.71	0.017	2.37	33.33	0.00050	47.22
Average	0.65	0.013	2.04	32.26	0.00041	49.45
STDEV	0.079	0.0035	0.50	4.07	0.00011	3.04

Table H2. Aln 0.2 Data

Beam Number	Beam Area (mm^2)	Total Porosity (mm^2)	Porosity (%)	Number of Pores (#)	Average Pore Size (mm^2)	Pore Density (#/mm^2)
59258_D	0.87	0.018	2.02	50.75	0.00035	58.26
60636_F	0.79	0.025	3.20	54.67	0.00047	68.86
59219_B	0.85	0.022	2.61	38.00	0.00058	44.90
59219_F	0.78	0.010	1.29	24.67	0.00041	31.77
60592_D	0.82	0.017	2.11	42.00	0.00041	51.03
59256_F	0.67	0.022	3.21	23.00	0.00094	34.35
59258_E	0.72	0.019	2.67	37.40	0.00052	51.68
60636_A	0.74	0.018	2.39	40.25	0.00044	54.48
60636_C	0.61	0.014	2.36	28.33	0.00051	46.42
60636_E	0.86	0.022	2.51	46.50	0.00047	53.99
60642_E	0.72	0.014	1.92	36.20	0.00038	50.03
60631_E	0.69	0.015	2.21	36.60	0.00041	53.40
59256_A	0.76	0.016	2.09	32.80	0.00048	43.18
59256_C	0.65	0.017	2.58	34.00	0.00050	51.99
Average	0.75	0.018	2.37	37.51	0.00049	49.59
STDEV	0.081	0.0040	0.50	9.09	0.00014	9.36

Table H3. Aln 1.0 Data

Beam Number	Beam Area (mm^2)	Total Porosity (mm^2)	Porosity (%)	Number of Pores (#)	Average Pore Size (mm^2)	Pore Density (#/mm^2)
59231_A	0.49	0.0104	2.13	29.00	0.00036	59.235
59231_D	0.98	0.0246	2.50	67.00	0.00037	68.113
60641_B	0.78	0.0204	2.62	48.33	0.00042	62.227
59236_D	0.82	0.0153	1.88	48.00	0.00032	58.891
60643_A	0.64	0.0135	2.12	22.67	0.00060	35.555
60657_D	0.69	0.0177	2.58	38.50	0.00046	56.113
60641_C	0.62	0.0081	1.31	27.50	0.00029	44.588
59211_A	0.45	0.0084	1.85	24.00	0.00035	53.043
60750_E	0.61	0.0096	1.58	24.00	0.00040	39.443
59238_A	0.74	0.0204	2.76	36.50	0.00056	49.310
59231_E	0.72	0.0163	2.26	39.75	0.00041	55.314
60809_A	0.71	0.0298	4.22	28.50	0.00105	40.405
Average	0.69	0.0162	2.32	36.15	0.00046	51.853
STDEV	0.14	0.0068	0.74	13.21	0.00020	10.079

APPENDIX I

OSTEONAL AND INTEROSTEONAL DATA

The following tables contain the osteonal and interosteonal data using in this investigation.

Table I1. Control Data

Beam Number	Osteonal Area (mm^2)	Osteonal Area (%)	Average Osteon size (mm^2)	Interosteonal Space (%)
60632_D	0.35	53.37	0.010	45.04
60628_B	0.30	49.59	0.010	48.27
60628_D	0.43	61.81	0.013	35.93
59315_B	0.50	68.44	0.015	29.81
59234_A	0.29	51.22	0.011	45.84
59234_C	0.30	58.60	0.012	40.23
59315_D	0.49	64.70	0.013	33.27
60667_A	0.41	64.17	0.012	33.73
60628_F	0.35	49.32	0.010	48.31
Average	0.38	57.91	0.012	40.05
STDEV	0.08	7.25	0.002	7.09

Table I2. Aln 0.2 Data

Beam Number	Osteonal Area (mm^2)	Osteonal Area (%)	Average Osteon size (mm^2)	Interosteonal Space (%)
59258_D	0.51	58.34	0.010	39.64
60636_F	0.47	59.49	0.009	37.30
59219_B	0.48	56.56	0.013	40.83
59219_F	0.19	24.93	0.008	73.78
60592_D	0.51	62.03	0.012	35.86
59256_F	0.36	53.33	0.016	43.45
59258_E	0.42	58.39	0.011	38.94
60636_A	0.41	56.07	0.010	41.54
60636_C	0.27	44.33	0.010	53.31
60636_E	0.38	43.68	0.008	53.81
60642_E	0.42	57.51	0.011	40.57
60631_E	0.43	62.85	0.012	34.94
59256_A	0.43	56.80	0.013	41.11
59256_C	0.34	51.97	0.010	45.45
Average	0.40	53.31	0.011	44.32
STDEV	0.089	9.94	0.0021	10.17

Table I3. Aln 1.0 Data

Beam Number	Osteonal Area (mm^2)	Osteonal Area (%)	Average Osteon size (mm^2)	Interosteonal Space (%)
59231_A	0.28	56.92	0.0096	40.95
59231_D	0.57	57.55	0.0084	39.94
60641_B	0.42	54.54	0.0088	42.84
59236_D	0.47	57.39	0.0097	39.30
60643_A	0.32	49.77	0.0140	48.11
60657_D	0.31	45.13	0.0080	52.30
60641_C	0.26	42.13	0.0094	56.57
59211_A	0.23	50.68	0.0096	47.47
60750_E	0.23	37.28	0.0095	61.14
59238_A	0.34	45.87	0.0093	51.37
59231_E	0.38	52.47	0.0095	45.27
60809_A	0.31	44.61	0.0110	51.17
Average	0.34	49.53	0.0097	48.03
STDEV	0.10	6.59	0.0015	6.81

APPENDIX J

CREEP DATA

The following tables contain strain (ε) data for elastic, e, (recovered) and plastic, p, (accumulated) deformation at initial (o) and final (n) cycles.

Table J1. Control Data

Beam Number	εp, o	εe, o	εp, n	εe, n	Creep εp, o / εp, n	Secant εe, o / εe, n
59315_D	0.0033	0.0062	0.0262	0.0134	0.1265	0.4606
59677_C	0.0046	0.0080	0.0352	0.0235	0.1310	0.3414
60628_E	0.0054	0.0089	0.0825	0.0288	0.0660	0.3095
60628_F	0.0032	0.0057	0.0337	0.0154	0.0959	0.3667
60632_F	0.0053	0.0089	0.0435	0.0246	0.1207	0.3628
60644_H	0.0064	0.0107	0.0387	0.0320	0.1651	0.3349
60667_A	0.0028	0.0051	0.0109	0.0094	0.2545	0.5455
60707_B	0.0041	0.0072	0.0292	0.0259	0.1412	0.2760
59257_D	0.0054	0.0092	0.0349	0.0277	0.1560	0.3333
60632_B	0.0564	0.0099	0.0895	0.0394	0.6305	0.2504
60632_D	0.0020	0.0117	0.0322	0.0240	0.0629	0.4875
60628_B	0.0024	0.0161	0.0457	0.1275	0.0520	0.1263
60628_D	0.0021	0.0115	0.0723	0.0304	0.0285	0.3768
59315_B	0.0015	0.0071	0.0104	0.0092	0.1457	0.7687
59234_A	0.0590	0.0079	0.0872	0.0157	0.6771	0.5046
59234_C	0.0023	0.0117	0.0267	0.0218	0.0864	0.5394
Average	**0.010**	**0.009**	**0.044**	**0.029**	**0.184**	**0.399**
STDEV	**0.019**	**0.003**	**0.025**	**0.027**	**0.191**	**0.149**

Table J2. Aln 0.2Data

Beam Number	εp, o	εe, o	εp, n	εe, n	Creep εp, o / εp, n	Secant εe, o / εe, n
59219_B	0.0002	0.0233	0.059	0.038	0.003	0.613
59219_F	0.0002	0.0156	0.023	0.024	0.007	0.655
60592_B	0.0044	0.0073	0.036	0.020	0.122	0.367
60592_D	0.0043	0.0076	0.039	0.023	0.108	0.337
60592_F	0.0057	0.0075	0.033	0.020	0.174	0.369
60636_A	0.0037	0.0061	0.069	0.020	0.053	0.303
60636_C	0.0050	0.0074	0.051	0.021	0.099	0.353
60636_E	0.0041	0.0070	0.062	0.061	0.066	0.115
60636_F	0.0030	0.0059	0.030	0.024	0.101	0.245
59256_A	0.0031	0.0139	0.091	0.050	0.034	0.280
59256_C	0.0036	0.0141	0.037	0.026	0.100	0.533
59256_F	0.0035	0.0059	0.029	0.013	0.123	0.455
59256_G	0.0081	0.0095	0.086	0.052	0.094	0.184
60631_B	0.0088	0.0116	0.067	0.059	0.131	0.197
60631_D	0.0003	0.0105	0.034	0.019	0.010	0.542
60631_E	0.0104	0.0126	0.075	0.057	0.138	0.222
60631_F	0.0050	0.0082	0.052	0.026	0.095	0.315
60631_G	0.0002	0.0140	0.035	0.022	0.006	0.625
60631_H	0.0047	0.0078	0.045	0.026	0.104	0.302
60642_E	0.0061	0.0097	0.041	0.025	0.150	0.382
59258_B	0.0039	0.0072	0.023	0.031	0.167	0.234
59258_D	0.0024	0.0095	0.024	0.017	0.101	0.569
59258_E	0.1401	0.2108	0.032	0.014	4.344	14.635
Average	**0.010**	**0.019**	**0.047**	**0.030**	**0.275**	**0.993**
STDEV	**0.028**	**0.042**	**0.020**	**0.015**	**0.888**	**2.978**

Table J3. Aln 1.0 Data

Beam Number	εp, o	εe, o	εp, n	εe, n	Creep εp, o / εp, n	Secant εe, o / εe, n
59231_E	0.0095	0.0136	0.0680	0.0548	0.1392	0.2482
59236_D	0.0062	0.0092	0.0395	0.0295	0.1574	0.3134
59238_A	0.0054	0.0072	0.0672	0.0238	0.0808	0.3023
59238_B	0.0044	0.0066	0.0317	0.0166	0.1404	0.3991
60593_A	0.0036	0.0061	0.0365	0.0220	0.0995	0.2771
60643_A	0.0090	0.0098	0.0728	0.0495	0.1242	0.1978
60643_C	0.0098	0.0108	0.0798	0.0393	0.1227	0.2742
60643_D	0.0065	0.0105	0.0658	0.0464	0.0995	0.2271
60750_D	0.0098	0.0135	0.0574	0.0383	0.1713	0.3531
60809_A	0.0083	0.0098	0.1163	0.0334	0.0716	0.2921
60750_E	0.0059	0.0073	0.0372	0.0217	0.1578	0.3350
59231_A	0.0576	0.0093	0.1247	0.0258	0.4617	0.3600
59231_C	0.0019	0.0129	0.0407	0.0297	0.0460	0.4331
59231_D	0.0017	0.0112	0.2710	0.0023	0.0063	4.8261
60641_B	0.0025	0.0092	0.0371	0.0237	0.0687	0.3892
59211_B	0.0023	0.0132	0.0484	0.0293	0.0477	0.4507
59211_D	0.0017	0.0076	0.0055	0.0080	0.3088	0.9495
60593_B	0.0084	0.0135	0.0523	0.0466	0.1607	0.2884
60657_D	0.0598	0.0171	0.1126	0.0347	0.5311	0.4920
60641_C	0.0032	0.0088	0.0317	0.0182	0.0996	0.4858
59211_A	0.0028	0.0135	0.0806	0.0436	0.0347	0.3086
Average	**0.0105**	**0.0105**	**0.0703**	**0.0303**	**0.1490**	**0.5811**
STDEV	**0.0163**	**0.0029**	**0.0551**	**0.0136**	**0.1324**	**0.9850**

Table J4. Control Outliers

Beam Number	εp, o	εe, o	εp, n	εe, n	Creep εp, o / εp, n	Secant εe, o / εe, n
59210_A	0.005	0.006	0.041	0.017	0.122	0.381
59677_D	0.017	0.016	0.085	0.035	0.200	0.474
60632_E	0.005	0.009	0.044	0.026	0.118	0.337
60634_A	0.006	0.008	0.031	0.020	0.197	0.380
60644_A	0.010	0.011	0.095	0.050	0.104	0.226
60632_A	0.058	0.017	0.142	0.050	0.408	0.337
60632_C	0.057	0.019	0.027	0.211	2.105	0.090
60628_A	0.061	0.011	0.104	0.022	0.588	0.512
60628_C	0.006	0.018	0.061	0.033	0.100	0.530
59315_A	0.063	0.018	0.098	0.030	0.645	0.610
59315_C	0.004	0.014	0.042	0.021	0.092	0.644
59234_B	0.010	0.021	0.114	0.050	0.085	0.426
Average	**0.025**	**0.014**	**0.074**	**0.047**	**0.397**	**0.412**
STDEV	**0.026**	**0.005**	**0.038**	**0.053**	**0.573**	**0.157**

Table J5. Aln 0.2 Outliers

Beam Number	εp, o	εe, o	εp, n	εe, n	Creep εp, o / εp, n	Secant εe, o / εe, n
59219_A	0.0083	0.0112	0.0423	0.0293	0.1950	0.3811
59219_C	0.0104	0.0106	0.0716	0.0426	0.1457	0.2479
60592_A	0.0123	0.0107	0.0666	0.0454	0.1853	0.2358
60592_E	0.0059	0.0087	0.0360	0.0232	0.1627	0.3758
59256_E	0.0031	0.0104	0.1052	0.0068	0.0294	1.5325
60631_C	0.0092	0.0079	0.0221	0.0183	0.4181	0.4311
60642_A	0.0076	0.0093	0.0474	0.0249	0.1611	0.3728
60642_F	0.0175	0.0182	0.0938	0.0330	0.1864	0.5508
59258_C	0.0077	0.0101	0.0844	0.0334	0.0912	0.3018
Average	**0.0091**	**0.0108**	**0.0633**	**0.0286**	**0.1750**	**0.4922**
STDEV	**0.0041**	**0.0030**	**0.0282**	**0.0120**	**0.1056**	**0.4017**

Table J6. Aln 1.0 Outliers

Beam Number	εp, o	εe, o	εp, n	εe, n	Creep εp, o / εp, n	Secant εe, o / εe, n
60643_E	0.0123	0.0157	0.0960	0.0644	0.1286	0.2438
60750_G	0.0074	0.0086	0.0600	0.0104	0.1230	0.8333
59236_B	0.0330	0.0139	0.0764	0.0339	0.4320	0.4112
59236_C	0.0428	0.0172	0.1119	0.0272	0.3822	0.6323
60657_C	0.0609	0.0125	0.0874	0.0197	0.6964	0.6381
59231_B	0.0046	0.0228	0.0707	0.0386	0.0644	0.5903
60641_D	0.0042	0.0276	0.0531	0.0370	0.0801	0.7471
59211_C	0.0038	0.0263	0.0801	0.0533	0.0468	0.4923
59211_E	0.0035	0.0373	0.0763	0.0382	0.0456	0.9767
Average	0.0192	0.0202	0.0791	0.0359	0.2221	0.6183
STDEV	0.0212	0.0090	0.0179	0.0163	0.2292	0.2213

REFERENCES

1. Cowin, S. Bone Mechanics Handbook 2nd Edition. New York New York: CRC Press LLC, 2001.

2. Mescher A. Junqueira's Basic Histology, 12th Edition. New York New York: The McGraw-Hill Companies, Inc, 2010.

3. Alberts B, Johnson A, Lewis J, Raff M, Roberts K, Walter P. Molecular Biology of The Cell 5th Edition Reference Edition. New York New York: Garland Science Taylor & Francis Group, 2008.

4. Ozkaya N, Nordin M. Fundamentals of Biomechanics: Equilibrium, Motion, and Deformation. New York New York: Springer Science +Business Media, LLC, 1999.

5. Bonewald L. Osteocytes as Dynamic Multifunctional Cells. Annals of the New York Academy of Sciences 2007; 1116: 281–90.

6. Marcus R, Feldman D, Nelson D, Rosen C. Osteoporosis 3rd Edition Volume 1. Burlington MA 01803: Elsevier Academic Press, 2008.

7. Pollard T, Earnshaw W. Cell Biology 1st Edition. Philadelphia PA: Elsevier Science, 2002.

8. Fawcett DW, William B. A Textbook of Histology 12th Edition. New York: Chapman & Hall, 1994.

9. Weiss L. Cell and Tissue Biology: A Textbook of Histology. Baltimore, Maryland: Urban & Schwarzenberg, 1988.

10. Einhorn T, O'Keefe R, Buckwalter J. Orthopaedic Basic Science: Foundations of Clinical Practice 3rd Edition. Rosemont, Il: American Academy of Orthopaedic Surgeons, 2007.

11. Riggs B, Parfitt A. Perspective Drug Use to Treat Osteoporosis: The Critical Need for a Uniform Nomenclature Based on Their Action on Bone Remodeling. Journal of Bone and Mineral Research 2005; 20: 177–84.

12. Frost HM. Some ABCs of skeletal pathophysiology. III: Bone balance and the delta B.BMU. Calcified Tissue International 1989; 45: 131–3.

13. Parfit AM. The two faces of growth: benefits and risks of bone integrity. Osteoporosis International 1994; 4: 382–98.

14. Seeman E. Structural basis of growth-related gain and age-related loss of bone strength. Rheumatology 2008; 47:iv2–iv8.

15. Murkami H, Takahashi N, Sasaki T, Udagawa N, Tanaka S, Nakamura I, Zhang D, Barbier A, and Suda T. A Possible Mechanism of the Specific Action of Bisphosphonates on Osteoclasts: Tiludronate Preferentially Affects Polarized Osteoclasts Having Ruffled Boarders. Bone 1995;17: 137–44.

16. Thomas T. Intermittent parathyroid hormone therapy to increase bone formation. Joint Bone Spine. 2006; 73: 262–9.

17. Boyce TM, Fyhrie DP, Glotkowski MC, Radlin EL, Schaffler MB. Damage type and strain mode association inhuman bone fatigue. Journal of Orthopaedic Research 1998; 16: 332–9.

18. Seeman E and Delmas P. Bone Quality- The Material and Structural Basis of Bone Strength and Fragility. The New England Journal of Medicine 2006; 354: 2250–61.

19. Wood WA. Formation of Fatigue Cracks. Philosophical Magazine 1958; 31:692–9.

20. Suresh S. Fatigue of Materials. Cambridge University Press New York NY 1991.

21. Thompson N, Wadsworth NJ, Louat N. The origin of fatigue fracture in copper. Philosophical Magazine 1956: 113–26.

22. Anderson TL. Fracture Mechanics; Fundamentals and Applications 2nd Edition. 1994.

23. National Osteoporosis Foundation. "Fast Facts on Osteoporosis." www.nor.org 8/20/2010

24. Saxton D, Pelikan P, Nugent P, Hyland P. The Addison-Wesley Manual of Nursing Practice. Menlo Park, California: Addison-Wesley Publishing Company, Inc, 1983.

25. Bilezikian, J. Combination Anabolic and Antriresorptive Therapy for Osteoporosis: Opening the Anabolic Window. Current Osteoporosis Report 2008: 6:24–30

26. Chaing T, Chang I, Lee H, Huang C, Cheng Y. Osteopontin regulates anabolic effect in human nemopausal osteoporosis with intermittent parathyroid hormone treatment. Osteoporosis International 2010; 22: 577–85.

27. Jiang Y, Zhao JJ, Mitlak BH, Wang O. Recombinant human parathyroid harmone (1-34) [teriparatide] improves both cortical and cancellous bone structure. Journal of Bone Mineral Research 2003; 18: 1932–41.

28. Rogers M, Frith J, Luckman S, Coxon F, Benford H, Monkkonen J, Auriola S, Chilton K, Russell R. Molecular mechanisims of action of bisphosphonates. Bone 1999; 24: 73S–9S.

29. Russell R. G. G., Rogers M.J. Bisphosphonates: from the laboratory to the clinic and back again. Bone 1999; 25: 97–106.

30. Boivin G, Chavassieux P, Santora A, Yates J, Meunier P. Alendronate increase bone strength by increasing the mean degree of mineralization of bone tissue in osteoporotic women. Bone 2000; 27: 687–94.

31. Allen M, Burr D. Bisphosphonate effects on Bone Turnover, Microdamage, and Mechanical Properties: What we think we know and what we know that we don't know. Bone 2010; 49: 56–65.

32. Lenart B, Lorich D, Lane J. "Atypical Fractures of the Femoral Diaphysis in Postmenopausal Women Taking Alendronate." The New England Journal of Medicine. 2008; 358: 1304–06.

33. Allen M, Reinwald S, Burr D. Alendronate reduces bone toughness of ribs without significantly increasing microdamage accumulation in dogs following 3 years of daily treatment. Calcif Tissue Int 2008; 82: 354–60.

34. O'Neal J, Diab T, Allen M, Vidakovic B, Burr D, Guldberg R. One year of alendronate treatment lowers microstructural stress associated with trabecular microdamage initiation. Bone online release 2010; 47: 241–7.

35. Parfitt AM, Drezner MK, Glorieux FH, Kanis JA, Malluche H, Meunier PJ, Ott SM, Recker R. Bone histomorphometry: Standardization of nomenclature, symbols and units. Journal of bone and mineral research 1987; 2: 595–609.

36. Cummings SR, Bates D, Black DM. Clinical use of bone densitometry: scientific review. Journal of the American medical association 2002; 288: 1889–97.

37. Black DM, Schwartz AV, Ensrud KE, Cauley JA, Levis S, Quandt SA, Satterfield S, Wallace RB, Bauer DC, Palermo L, Wehren LE, Lombardi A, Santora AC, Cummings SR. Effects of continuing or stopping alendronate after 5 years of treatment. Journal of the American medical association 2006; 296: 2927–38.

38. Mazess RB, Barden HS, Bisek JP, Hanson J. Dual-energy x-ray absorptiometry for total-body and regional bone-mineral and soft-tissue composition. American journal of clinical nutrition 1990; 51: 1106–12.

39. Liu XS, Cohen A, Shange E, Yin PT, Stein EM, Rogers H, Kokolus SL, McMahon DJ, Lappe JM, Recker RR, Lang T, Gou XE. Bone density, geometry, microctructure, and stiffness: relationships between peripheral and central skeletal sites assessed by DXA, HR-pQCT, and cQCT in premenopausal women. Journal of bone and mineral research 2010; 25: 2229–38.

40. Donnelly E. Methods for assessing bone quality: a review. Clinical Orthopaedics and Related Research 2010; 469: 2128–38.

41. Roschger P, Rinnerthaler S, Yates J, Rodan GA, Fratzl P, Klaushofer K. Alendronate increases degree of uniformity of mineralization in cancellous bone and decreases the porosity in cortical bone of osteoporotic women. Bone 2001; 29: 185–91.

42. Burr DB, Turner CH, Naick P, Forwood MR, Ambrosius W, Hasan MS, Pidaparti R. 1998. Does microdamage accumulation affect the mechanical properties of bone? Journal of Biomechanics. 1998; 31: 337–45.

43. Boyce TM, Fyhrie DP, Clotkowski MC, Radin EL, Schaffler MB. Damage type and strain mode associations in human compact bone bending fatigue. Journal of Orthopaedic Research 1998; 16: 322–9.

44. Diab T, Condon K, Burr D, Vashishth. Age-related change in the damage morphology of human cortical bone and its role in bone fragility. Bone 2006; 38: 427–31.

45. Diab T and Vashishth D. Morphology, localization and accumulation of in vivo microdamage in human cortical bone. Bone 2007; 40: 612–8.

46. Burr DB, Hooser M. Alterations to the en bloc basic fuchsin staining protocol for the demonstration of microdamage produced in vivo. Bone 19995; 17: 431–3.

47. Allen M, Iwata K, Phipps R, Burr D. Alterations in canine vertebral bone turnover, microdamage accumulation, and biomechanical properties following 1-year treatment with clinical treatment doses of risedronate or alendronate. Bone 2006; 39: 872–9.

48. Allen M, Burr D. Three years of alendronate treatment results in similar levels of vertebral microdamage as after one year of treatment. Journal of Bone and Mineral Research 2007; 22: 1759–65.

49. Allen MR and Burr DB. Bisphosphonate effect on bone turnover, microdamage, and mechanical properties: what we think we know and what we know that we don't know. Bone 2011; 49: 56–65.

50. van der Meulen MC, Jepsen KJ, Milic B. Understanding bone strength: size isn't everything. Bone 2001; 29: 101–4.

51. Mashiba T, Hirano T, Turner CH, Forwood MR, Johnston CC, Burr DB. Supressed bone turnover by bisphosphonates increases microdamage accumulation and reduces some biomechanical properties in dog rib. Journal of Bone Mineral Research 2000; 15: 613–20.

52. Browner B. Skeletal Trauma, 4th edition. W.B. Saunders Company. 2008.

53. Arcan, M., Hashin Z., and Voloshin. A., 1978, A Method to Produce Uniform Plane Stress States with Applications to Fiber-Reinforced Materials. Experimental Mechanics, 1978; 18:141–6.

54. Reilly and Burstein The elastic and ultimate properties of compact bone tissue. Journal of Biomechanics. 1975; 8: 393–6.

55. Komastsubara S, Mori S, Mashiba T, Li J, Nonaka K, Kaji Y, Akiyama T, Miyamoto K, Cao Y, Kawanishi J, Norimatsu H. Supressed bone turnover by long-term bisphosphonate treatment accumulated microdamage but maintains intrinsic material properties in cortical bone of dog rib. Journal of bone and mineral research 2004; 19: 999–1005.

56. Turner CH and Burr DB. Basic biomechanical measurements of bone: a tutorial. Bone 1993; 14: 595–608.

57. Levenston ME, Beaupre GS, van der Meulen MC. Improved method for analysis of whole bone torsion tests. 1994; 9: 1459–65.

58. Carter DR and Hayes WC. Fatigue life of compact bone-I effects of stress amplitude, temperature and density. Journal of biomechanics 1976; 9: 27–34.

59. Hibbeler, RC. Mechanics of Materials 6th Edition. Pearson Prentice Hall Upper Saddle River, NJ 2005.

60. Choi K and Goldstein SA. A comparison of the fatigue behavior of human trabecular and cortical bone tissue. Journal of biomechanics 1992; 25: 1371–81.

61. Liberman UA, Weiss SR, Broll J, Minne HW, Quan H, Bell NH, Rodrigues-Portales J, Downs RW, Dequeker J, Favus M, Seeman E, Recker RR, Capizzi T, Santora II AC, Lombardi A, Shah RV, Hirsch LJ, Kapf DB. Effect of oral alendronage on bone mineral density and the incidence of fractures in postmenopausal osteoporosis. The new England journal of medicine 1995; 333: 1437–43.

62. Bone HG, Hosking D, Devogelaer JP, Tucci JR, Emkey RD, Tonino RP, Rodrigues-Portales JA, Downs RW, Gupta J, Santora AC, Liberman UA. Ten years' experience with alendronage for osteoporosis in postmenopausal women. The New England journal of medicine 2004; 350: 1189–99.

63. Shane E, Burr D, Ebeling PR, Abrahamsen B, Adler RA , Brown TD, Cheung AM, Cosman F, Curtis JR, Dell R, Dempster D, Einhorn TA, Genant HK , Geusens P, Klaushofer K , Koval K, Lane JM, McKiernan F, McKinney F, Ng A, Nieves J, O'Keefe R, Papapoulos S, Sen HT, CH van der Meulen M, Weinstein RS, Whyte M. Atypical subtrochanteric and diaphyseal demoral fractures; report of a task force of the American society for bone and mineral research. Journal of bone mineral research 2010: 25; 2267–94.

64. Girgis and Seibel. Atypical fractures and bisphosphonate use. The New England Journal of Medicine. 2010; 362: 1848–9.

65. Neviaser A, Lane J, Lenart B, Edobor-Osula F, Lorich D. Low-energy femoral shaft fractures associated with alendronate use. Journal of Orthopaedic Trauma. 2008; 22: 346–50.

66. Delmas PD, Eastell R, Garnero P, Seibel MJ, Stepan J. The use of biochemical markers of bone turnover in osteoporosis. Osteoporosis International. 2000; 6: S2–17.

67. Singer FR. Metabolic bone disease: atypical femoral fractures. Journal of biomechanics 2010; 44: 244–7.

68. Somford MP, Bilateral dractures of the demur diaphysis in a patient with rheumatoid artheiris on long-term treatment with alendronate: clues to the mechanism of increased bone fragility. Journal of Bone and Mineral Research. 2009; 24: 1746–40.

69. Abrahamsen B, Eiken P, Eastell R. Subtrochanteric and diaphyseal demur fractures in patients treated with alendronate: a register-based national cohort study. Journal of Bone Mineral Research 2009; 24: 1095–102.

70. Operation and maintenance instruction. IsoMet® liner precision saw. Buehler USA, Illinois.

71. Suresh S. Fatigue of Materials. The Press Syndicate of the University of Cambridge, New York New York. 1991.

72. Ozkaya N, Nordin M. Fundamentals of Biomechanics: Equilibrium, Motion, and Deformation. Springer Science +Business Media, LLC, New York New York: 1999.

73. Danova NA, Colopy SA, Radtke CL, Kalscheur VL, Markel MD, Vanderby R, McCabe RP, Escarcega AJ, Muir P. Degradation of bone structural properties by accumulation and coalescence of microcracks. Bone 2003; 33:197–205.

74. Diab T, Vashishth D. Effects of damage morphology on cortical bone fragility. Bone 2005; 37: 96–102.

75. Cotton JR, Zioupos P, Winwood K, Taylor M. Analysis of creep strain during tensile fatigue of cortical bone. Journal of Biomechanics 2003; 36: 943–9.

76. Fleck C, Eifler D. Deformation behavior and damage accumulation of cortical bone specimens from the equine tibia under cyclic loading. Journal of Biomechanics 2003; 36: 179–89.

77. Gibson VA, Stover SM, Martin RB, Gibeling JC, Willits NH, Gustafson MB, Griffin LV. Fatigue behavior of the equine third metacarpus: mechanical property analysis. Journal of Orthopaedic Research 1995; 13: 861–8.

78. Monreno LD, Waldman SK, Grynpas MD. Sex differences in long bone fatigue using a rat model. Journal of Orthopaedic Research 2006; 24: 1924–32.

79. Pattin CA, Caler WE, Carter DR. Cyclic mechanical property degradation during fatigue loading of cortical bone. Journal of Biomechanics 1996; 29: 69–79.

80. Schaffler MB, Radin EL, Burr DB. Mechanical and morphological effects of strain rate on fatigue of compact bone. Bone 1989; 10: 207–14.

81. Schaffler MB, Radin EL, Burr DB. Long-term fatigue behavior of compact bone at low strain magnitude and rate. Bone 1990; 11: 321–6.

82. Winwood K, Zioupos P, Currey JD, Cotton JR, Taylor M. Strain patterns during tensile, compressive and shear fatigue of human cortical bone and implications for bone ciomechanics. Journal of Biomedical materials Research 2006; 79A: 289–97.

83. Zioupos P, Wang XT, Currey JD. The accumulation of fatigue microdamage in human cortical bone of two different ages in vitro. Clinical Biomechanics 1996; 11: 365–75.

84. Akkus O, Knott DF, Jepsen KJ, Davy DT, Rimnac CM. Relationship between damage accumulation and mechanical property degradation in cortical bone: microcrack orientation is important. Journal of Biomedical Materials Research 2003; 65A.4: 482–8.

85. Jepsen KJ, Davy DT Comparison of damage accumulation measures in human cortical bone. Journal of Biomechanics 1997; 30: 891–4.

86. Pidaparti RM, Akyuz U, Naick PA, Burr DB. Fatigue data analysis of canine femurs under four-point bending. Biomedical Materials and Engineering 2000; 10: 43–50.

87. Landrigan, MD, Roeder RK. Systematic error in mechanical measures of damage during four-point bending fatigue of cortical bone. Journal of Biomechanics 2009; 42: 1212–17.

88. Lou Q, Leng H, Acuna R, Dong X, Rong Q, Wang X. Constitutive relationship of tissue behavior with damage accumulation of human cortical bone. Journal of biomechanics 2010; 43: 2356–61.

89. Roschger P, Rinnerthaler S, Yates J, Rodan GA, Fratzl P, Klaushofer K. Alendronate increases degree and uniformity of mineralization in cancellous bone and decreases the porosity in cortical bone of osteoporotic women. Bone 2001; 29: 185–91.

90. Burr DB, Diab T, Koivunemi A, Koivunemi M, Allen MR. Effects of one to three years treatment with alendronate on mechanical properties of the femoral shaft in a canine model: implications for subtrochanteric femoral fracture risk. Journal of Orthopeadic Research 2009; 27: 1288–92.